

Predicting Static Data Using Dynamic Data and Quantitative Sample  
Characterization

by  
Abdullah Bilal

A dissertation submitted to the Department of Petroleum Engineering,  
Cullen college of Engineering  
in partial fulfillment of the requirements for the degree of

Doctor of Philosophy

in Petroleum Engineering

Chair of Committee: Assistant Professor, Dr. Lori Hathon

Committee Member: Associate Professor, Dr. Michael Myers

Committee Member: Associate Professor, Dr. Guan Qin

Committee Member: Associate Professor, Dr. Konstantinos Kostarelos

Committee Member: Dr. Nishank Saxena

University of Houston

December 2019

Copyright 2019, Abdullah Bilal

*To my parents, who instilled in me the virtues of perseverance and encouraged me to  
strive for excellence.*

*To my sisters, for their endless love.*

*And,*

*to my lovely wife, Amina, for being understanding and supportive. Thank you for  
always being there.*

# Acknowledgment

I would like to express my deepest gratitude to my advisers Dr. Lori Hathon and Dr. Michael Myers, whose consistent encouragement, guidance, and support from the very beginning enabled me to work on my research and finish my dissertation.

I would like to thank the rest of my thesis committee, Dr. Guan Qin, Dr. Konstantinos Kostarelos, from the department of Petroleum engineering at Cullen college of engineering and Dr. Nishank Saxena from Shell E&P, for their suggestions and insightful comments.

I am very thankful to my friends and lab-mates, Mohab Dessouki, Clara Palencia, Jim Funk, Sabya Prakash, Aryab Mazumdar, and other students in the lab.

I am also grateful to my uncles, Javed Akhtar, Tahir Mehmood, and Muhammad Ahmad, for their guidance and professional insights.

## Abstract

We have analyzed static and dynamic data along a triaxial stress path with the goal of better understanding the mechanisms controlling each response and their relationship to the correlation between large strain and small strain measurements. “Static data” large strain ( $10^{-4}$ ) measurements were performed on both unloading and reloading along a multistage triaxial stress path. Simultaneous “dynamic data” ( $10^{-6}$ ) strain were acquired using standard pitch and catch acoustic velocity measurement techniques. The samples were measured “dry” i.e. equilibrated to ambient conditions. Young’s modulus was calculated from the acoustic data and compared to the measured static Young’s modulus. A quadratic fit has been applied to the static unloading and reloading data. This allows us to characterize the elastic data in terms of linear and nonlinear elastic terms, with coefficients  $M_1$ , and  $M_2$  respectively. The quadratic fit for the elastic data is subtracted from the total strain response during each reload cycle to obtain the “induced plastic strains”. The value of  $M_1$  is found to be equal to the measured dynamic modulus within experimental error. It was therefore interpreted to be dominated by the physics of the grain contacts.  $M_2$ , the nonlinear elastic term, is interpreted to be due to the opening and closing of induced micro-cracks. This is based on the correlation observed between  $M_2$  and the measured irrecoverable strains. A network model is developed to fit the observed plastic strain data as a function of mean and deviatoric stress. Application of this model allows prediction of the sample stiffness (the slope of a triaxial test along the initial loading curve), at any confining stress. This is a key component of wellbore stability models, and allows for more robust model developments for wellbore stability, sand control etc. Future work will include the extension of the model to include nonlinearities for the prediction of failure. Thin section analysis to predict the plastic and nonlinear elastic parameters in combination with velocity data is also planned.

# Table of Contents

|  |             |
|--|-------------|
| <b>Dedication</b>  | <b>iii</b>  |
| <b>Acknowledgment</b>  | <b>iv</b>   |
| <b>Abstract</b>  | <b>v</b>    |
| <b>Table of Contents</b>   | <b>viii</b> |
| <b>List of Tables</b>  | <b>x</b>    |
| <b>List of Figures</b>   | <b>xxii</b> |
| <b>Chapter 1: Introduction</b>   | <b>1</b>    |
| 1.1 Significance of Thesis . . . . .   | 1           |
| 1.2 Introduction . . . . .   | 1           |
| 1.2.1 Static (large strain) Data Review . . . . .  | 1           |
| 1.2.2 Dynamic (small strain) Data Review . . . . .   | 3           |
| 1.2.3 Static Versus Dynamic Data . . . . .   | 6           |
| 1.2.4 Difficulties in Characterization and Modeling of Static and Dy-<br>namic Data (It's not trivial) . . . . . | 8           |
| 1.3 Terminology and Definition . . . . .   | 10          |
| 1.3.1 The Stress-strain Curve . . . . .  | 10          |
| 1.3.2 Deviatoric Stress . . . . .  | 11          |
| 1.3.3 Strain and its Relation to the Point of Positive Dilatancy . . . . .                                       | 12          |
| 1.3.4 Modulus . . . . .  | 13          |
| 1.4 Mohr-Coulomb failure criteria . . . . .  | 14          |
| 1.5 Triaxial Test . . . . .  | 15          |
| 1.6 Multistage Triaxial Test (MST) Methodology . . . . .   | 15          |

|  |  |           |
|--|--|-----------|
| 1.6.1  | Irrecoverable Strain . . . . .                           | 18        |
| <b>Chapter 2: Experimental analysis</b>      |  | <b>19</b> |
| 2.1  | Experimental Setup and Stress Protocol . . . . .         | 19        |
| 2.2  | Multistage Triaxial Test . . . . .                       | 21        |
| 2.2.1  | Austin Chalk . . . . .                                   | 22        |
| 2.2.2  | Berea Sandstone . . . . .                                | 24        |
| 2.2.3  | Castlegate Sandstone . . . . .                           | 26        |
| 2.2.4  | Boise Sandstone . . . . .                                | 27        |
| 2.2.5  | Fontainebleau Sandstone . . . . .                        | 31        |
| 2.2.6  | Miocene sandstone . . . . .                              | 37        |
| 2.3  | Experimental Data Modeling and Analysis . . . . .        | 40        |
| 2.3.1  | Quadratic Fit for the Stress vs Strain Curve . . . . .   | 40        |
| 2.3.2  | Interpretation of $M_1$ Velocity . . . . .               | 42        |
| 2.3.3  | Interpretation of $M_2$ – Irrecoverable Strain . . . . . | 43        |
| 2.3.4  | $M_1$ and $M_2$ on an Unloading Stress Path . . . . .    | 44        |
| 2.3.5  | Compaction Model . . . . .                               | 45        |
| 2.3.6  | Mathematical Representation . . . . .                    | 45        |
| 2.3.7  | Model Calibration . . . . .                              | 50        |
| 2.3.8  | Experimental Fit for Plastic Strains . . . . .           | 52        |
| 2.4  | Modeling Summary . . . . .                               | 55        |
| <b>Chapter 3: Predicting a triaxial test</b> |  | <b>56</b> |
| 3.1  | Miocene sandstone Prediction . . . . .                   | 56        |
| 3.2  | Castlegate Sandstone Prediction . . . . .                | 58        |
| 3.3  | Berea Sandstone Prediction . . . . .                     | 58        |
| 3.4  | Austin Chalk Prediction . . . . .                        | 59        |
| 3.5  | Fontainebleau Sandstone Prediction . . . . .             | 60        |

|   |   |            |
|---|---|------------|
| 3.6   | Austin Chalk-2 Prediction . . . . .                   | 62         |
| 3.7   | Miocene-2 sandstone Prediction . . . . .              | 63         |
| 3.8   | Generalized Stress Path for Plastic Strains . . . . . | 65         |
| 3.8.1   | Matlab GUI . . . . .                                  | 66         |
| <b>Chapter 4: Sample Characterization</b>     |   | <b>68</b>  |
| 4.1   | Fontainebleau-1 Sandstone Characterization . . . . .  | 68         |
| 4.2   | Fontainebleau-3 Sandstone Characterization . . . . .  | 77         |
| 4.3   | Boise Sandstone Sample Characterization . . . . .     | 83         |
| 4.4   | Miocene sandstone . . . . .                           | 89         |
| 4.5   | Characterization Discussion . . . . .                 | 95         |
| <b>Chapter 5: Conclusions and Future work</b> |   | <b>103</b> |
| 5.1   | Conclusions . . . . .                                 | 103        |
| 5.2   | Future Work . . . . .                                 | 103        |
| <b>References</b>                             |   | <b>105</b> |
| <b>Appendix I</b>                             |   | <b>111</b> |
| <b>Appendix II</b>                            |   | <b>115</b> |

## List of Tables

|    |  |    |
|----|--|----|
| 1  | Austin Chalk sample dimensions and weight. . . . .                 | 24 |
| 2  | Berea sandstone sample dimensions and weight. . . . .              | 24 |
| 3  | Castlegate Sandstone sample dimensions and weight. . . . .         | 26 |
| 4  | Boise 1 Sandstone sample dimensions and weight. . . . .            | 28 |
| 5  | Boise-2 Sandstone sample dimensions and weight. . . . .            | 29 |
| 6  | Fontainebleau-1.9 Sandstone sample dimensions and weight. . . . .  | 31 |
| 7  | Fontainebleau-1.10 Sandstone sample dimensions and weight. . . . . | 33 |
| 8  | Fontainebleau-3.5 Sandstone sample dimensions and weight. . . . .  | 35 |
| 9  | Fontainebleau-3.4 Sandstone sample dimensions and weight. . . . .  | 37 |
| 10 | Miocene-1 sandstone sample dimensions and weight. . . . .          | 37 |
| 11 | Miocene-3 sandstone sample dimensions and weight. . . . .          | 39 |
| 12 | Miocene-1 Sandstone Model Parameters. . . . .                      | 57 |
| 13 | Castlegate Sandstone Model parameters. . . . .                     | 58 |
| 14 | Berea Model Parameters. . . . .                                    | 59 |
| 15 | Austin Chalk Model Parameters. . . . .                             | 60 |
| 16 | Fontainebleau Sandstone Model Parameters. . . . .                  | 61 |
| 17 | Austin Chalk-2 Model Parameters. . . . .                           | 62 |
| 18 | Miocene-2 sandstone Model Parameters. . . . .                      | 64 |
| 19 | Fontainebleau-1 Sandstone sample characterization summary. . . . . | 74 |
| 20 | Fontainebleau-1 Sandstone sample cracks summary. . . . .           | 77 |
| 21 | Fontainebleau-3 Sandstone sample characterization summary. . . . . | 82 |
| 22 | Fontainebleau-3 Sandstone sample cracks summary. . . . .           | 82 |
| 23 | Boise Sandstone sample characterization summary. . . . .           | 88 |
| 24 | Boise Sandstone framework grain characterization summary. . . . .  | 88 |
| 25 | Boise Sandstone sample cracks summary. . . . .                     | 88 |

|    |  |     |
|----|--|-----|
| 26 | Miocene sandstone sample characterization summary. . . . . | 94  |
| 27 | Miocene sandstone grains characterization summary. . . . . | 94  |
| 28 | Miocene sandstone sample cracks summary. . . . .           | 95  |
| 29 | Modeling parameters for every sample. . . . .              | 102 |

# List of Figures

|   |  |    |
|---|--|----|
| 1 | The figure shows typical stress-strain behavior of rock under increasing axial stress. The three regions exhibited are defined by the magnitudes of the recoverable and irrecoverable strains. $S$ is the slope of the stress strain curve and referred to as the sample stiffness. If the region is assumed to be elastic, the stiffness is equal to Young's modulus ( $E$ ). . . . . | 11 |
| 2 | Data for a typical triaxial test. The deviatoric stress is plotted on the vertical axis. The axial strain is plotted on the horizontal axis. This is a conventional triaxial test where the confining stress is held constant throughout. . . . .  | 16 |
| 3 | A typical MST stress path. The red curve is at a lower confining stress than the blue. The point of positive dilatancy (Strain Ratio = 0.5) is indicated where the unload cycle begins . . . . .   | 17 |
| 4 | The point of positive dilatancy (PPD) used for multi-stage triaxial (MST) tests. Sample unloading begins once this point is reached . . .  | 17 |
| 5 | Confining stress versus axial strain for Austin Chalk. This plot is easily interpreted for the percent irrecoverable strain . . . . .  | 18 |
| 6 | A typical experimental setup for a tri-axial test. Internal measurements of axial strain, radial strain and load are performed. . . . .  | 20 |
| 7 | The cylindrical pressure vessel in which the sample assembly is placed. The maximum confining pressure is 12000 psi which is applied by displacement pumps under PID (proportional integral differential) control.   | 20 |
| 8 | Experimental setup including the computerized control panel. The entire apparatus is PID controlled and capable of 75000 lb. axial load and 12000 psi confining stress. . . . .  | 21 |

|    |  |    |
|----|--|----|
| 9  | The Fountain plot for Austin Chalk showing deviatoric stress vs. axial, radial, and volumetric strain. The inset shows that the PPD has been reached. This is the most ductile sample measured exhibiting 20 percent irrecoverable strain. . . . . | 23 |
| 10 | The p/q plot for Austin Chalk, the friction angle is 26 degrees and the measured cohesion is 1900 psi. Due to the ductile nature of this material the actual cohesion may be much lower (nonlinear yield criteria).                                | 23 |
| 11 | Fountain plot for a sample of the Berea Sandstone showing deviatoric stress vs axial, radial and volumetric strains. This is the least ductile sample measured, exhibiting only 5 percent irrecoverable strain. . . .                              | 25 |
| 12 | The p/q plot for Berea Sandstone, the friction angle is 36 degrees and the measured cohesion is 2200 psi. . . . .  | 25 |
| 13 | Fountain plot for Castlegate Sandstone showing deviatoric stress vs axial, radial and volumetric strain. The irrecoverable strain is 15 percent . . . . .  | 26 |
| 14 | The p/q plot for Castlegate Sandstone, the friction angle is 30.5 degrees and the measured cohesion is 1320 psi. . . . .   | 27 |
| 15 | Fountain plot for Boise Sandstone showing deviatoric stress vs axial, radial and volumetric strain. The sample exhibited 45 percent irrecoverable strain. . . . .  | 28 |
| 16 | The p/q plot for Boise-1 Sandstone, the friction angle is 25.7 degrees and the measured cohesion is 1300 psi. . . . .  | 29 |
| 17 | Fountain plot for the Boise Sandstone showing deviatoric stress vs axial, radial and volumetric strain. The sample exhibited 45 percent irrecoverable strain. . . . .  | 30 |
| 18 | The p/q plot for Boise-2 Sandstone, the friction angle is 23.0 degrees and the measured cohesion is 1326 psi. . . . .  | 30 |

|    |  |    |
|----|--|----|
| 19 | Fountain plot for Fontainebleau-1.9 Sandstone showing deviatoric stress vs. axial, radial and volumetric strain. The sample exhibited 5 percent irrecoverable strain. . . . .            | 32 |
| 20 | The p/q plot for Fontainebleau Sandstone, the friction angle is 63.2 degrees and the measured cohesion is 300 psi. . . . .   | 32 |
| 21 | Fountain plot for the Fontainebleau Sandstone sample 1.10 showing deviatoric stress vs axial, radial and volumetric strain. The sample exhibited 5 percent irrecoverable strain. . . . . | 33 |
| 22 | The p/q plot for Fontainebleau Sandstone, the friction angle is 56 degrees and the measured cohesion is 1500 psi. . . . .  | 34 |
| 23 | Fountain plot for Fontainebleau Sandstone showing deviatoric stress vs axial, radial and volumetric strain. The sample exhibited 5 percent irrecoverable strain. . . . .                 | 34 |
| 24 | The p/q plot for Fontainebleau Sandstone, the friction angle is 22.0 degrees and the measured cohesion is 4700 psi. . . . .  | 35 |
| 25 | Fountain plot for Fontainebleau Sandstone showing deviatoric stress vs. axial, radial, and volumetric strain. The sample exhibited 5 percent irrecoverable strain . . . . .              | 36 |
| 26 | The p/q plot for Fontainebleau Sandstone, the friction angle is 24.3 degrees, and the measured cohesion is 5200 psi. . . . .   | 36 |
| 27 | Fountain plot for a Miocene sandstone sample showing deviatoric stress vs. axial, radial, and volumetric strain. The sample exhibited 43 percent irrecoverable strain. . . . .           | 38 |
| 28 | The p/q plot for Miocene-1 sandstone sandstone, the friction angle is 39.2 degrees, and the measured cohesion is 920 psi. . . . .  | 38 |

|    |   |    |
|----|---|----|
| 29 | Fountain plot for the Miocene sandstone showing deviatoric stress vs. axial, radial, and volumetric strain. The sample exhibited a 6 percent irrecoverable strain because the stopping point for each stage was reduced to a strain ratio of 0.3. . . . . .   | 39 |
| 30 | The p/q plot for Miocene-3 sandstone, the friction angle is 30.6 degrees, and the measured cohesion is 160 psi. . . . . .   | 40 |
| 31 | An example of a deviatoric stress vs. strain curve showing the actual data and the quadratic fit to the data. Induced plastic strains are calculated by taking the difference between actual data and the quadratic fit. . . . . .  | 41 |
| 32 | Dynamic vs. static M1 on the loading stress path. The static and dynamic properties are equal within experimental error. There are multiple points for each sample implying a small stress dependence for each sample compared to the differences between samples. . . . . .  | 42 |
| 33 | $M_1$ vs. confining pressure. $M_1$ varies significantly with confining pressure for Fontainebleau samples and Berea. However, it remains relatively constant for Austin Chalk, Boise Sandstone, and Miocene sandstone samples. The result is currently under investigation. The dots are dynamic $M_1$ , where velocity data is available. . . . . . | 43 |
| 34 | Absolute $M_2$ vs irrecoverable strains. $M_2$ has a direct relationship with irrecoverable strain. For higher irrecoverable strain, the value of $M_2$ is higher. The higher $M_2$ value implies more non-linear strain effects. . . . . .   | 44 |
| 35 | The initial known network consists of nodes with multiple connections to one another. The statistics of the network are described by $n(N,j)$ the number of nodes with $j$ connections when there are $N$ total nodes in the network. . . . . .   | 47 |

|    |   |    |
|----|---|----|
| 36 | Solution to a model where it is assumed that the fractional change in the number of nodes is proportional to the fractional change in the total number of nodes . . . . .   | 47 |
| 37 | Depending on the form that the $k(n,j)$ term takes, the equation allows for models where the distribution translates, broadens, skews and shows nonlinear effects with increasing numbers of nodes. . . . .   | 48 |
| 38 | An example of a deviatoric stress vs. strain curve showing the actual data and the quadratic fit to the data. Induced plastic strains are calculated by taking the difference between actual data and the quadratic fit. . . . .  | 50 |
| 39 | Plastic strains as a function of deviatoric stress for Castlegate Sandstone. The solid black lines are model predictions. A simple exponential is used to fit the data. The model is fit using only three parameters: $(\eta_o)$ 1.06E-4, $(k_d)$ 513 psi and $(k_m)$ -633 psi. . . . .         | 52 |
| 40 | Plastic strains as a function of deviatoric stress for the Austin Chalk. The solid black lines are model predictions. A simple exponential is used to fit the data. The model is fit using only three parameters: $(\eta_o)$ 3.11E-3, $(k_d)$ 606 psi and $(k_m)$ -943 psi. . . . .             | 53 |
| 41 | Plastic strains as a function of deviatoric stress for Boise-1 Sandstone. The solid black lines are model predictions. A simple exponential is used to fit the data. The model is fit using only three parameters: $(\eta_o)$ 5.05E-4, $(k_d)$ 115 psi and $(k_m)$ -505 psi. . . . .            | 54 |
| 42 | Plastic strains as a function of deviatoric stress for the Boise-2 Sandstone sample. The solid black lines are model predictions. A simple exponential is used to fit the data. The model is fit using only three parameters: $(\eta_o)$ 2.15E-4, $(k_d)$ 114 psi and $(k_m)$ -200 psi. . . . . | 54 |

|    |   |    |
|----|---|----|
| 43 | Plastic strains as a function of deviatoric stress for the Miocene-1 sandstone sample. The solid black lines are model predictions. A simple exponential is used to fit the data. The model is fit using only three parameters: ( $\eta_o$ ) 4.69E-5, ( $k_d$ ) 240 psi and ( $k_m$ ) -195 psi. . . . .                 | 55 |
| 44 | (A) Miocene sandstone MST data on sample "MR" that is used to calibrate the model to predict a triaxial test. (B) Sample "MM" data used to validate the model prediction. The predicted data are shown as black lines, and the measured data is shown in blue. The model predicts the measured data quite well. . . . . | 57 |
| 45 | Castlegate Sandstone MST data for initial loading curve at 500 psi confining along with the model results at 500 psi, 1000 psi and 1500 psi confining pressures. The model predicts the initial loading curve quite well. . . . .   | 58 |
| 46 | Berea MST data for the initial loading curve at 1000 psi confining stress along with model results for 1000 psi, 2000 psi and 3000 psi confining pressure. The model predicts the initial loading curve quite well. . . .   | 59 |
| 47 | Austin Chalk MST data and model results for the initial loading curve at 500 psi confining along with the predicted data at 1000 psi, and 1500 psi confining pressures. The model predicts the initial loading curve quite well. . . . .  | 60 |
| 48 | Fontainebleau Sandstone MST data for the initial loading curve at 1000 psi confining stress shown together with the model results at 500 psi, 1000 psi and 1500 psi confining pressures. The model predicts the initial loading curve quite well. . . . .   | 61 |
| 49 | Austin Chalk-2 MST and SST tests plot. The test was performed by Al Salman et al. (2015). The MST test was used to calibrate the model. The results were then used to predict single stage triaxial tests.  | 62 |

|    |  |    |
|----|--|----|
| 50 | SST data prediction for four Austin Chalk samples at four different confining pressures. The red lines show the raw data, and the black lines show the model predictions. The model predicts the single stage test data within 1-2% of the original data. . . . .  | 63 |
| 51 | Miocene-2 sandstone MST and SST tests plot. The test was performed by Al Salman et al. (2015). The MST test was used to calibrate the model. The results were then used to predict single stage triaxial tests.  | 64 |
| 52 | SST data prediction for Miocene sandstone at four different confining pressures. The red line is the raw data, and the black line is the model prediction. The model predicts the data quite well. . . . .   | 65 |
| 53 | (A) Constant mean stress prediction. (B)Constant deviatoric stress prediction. The plastic strains increase due to increasing deviatoric stress (const. mean stress test), and decrease due to increasing mean stress (const. deviatoric stress test). . . . .   | 66 |
| 54 | Matlab interface for calculating plastic strains along different stress paths. The model is calibrated from a triaxial stress path to predict other stress paths. The first figure is a triaxial stress path. The second shows the predicted constant mean and constant deviatoric stress path results. The third and fourth are the 2D projections of figure 2. As expected, the plastic strains increase for increasing deviatoric stress and decrease for increasing mean stress. . . . . | 67 |
| 55 | Pre-test Fontainebleau-1 Sandstone thin-section. The black circles show the regions from which tiles were selected for quantitative analysis. The scale bar is 0.2 in. . . . .   | 69 |
| 56 | The analyzed image shows the sampled porosity, percentage cement, contacts between grains, and sampled grains. The scale bar is 200 microns. . . . .   | 70 |

|    |  |    |
|----|--|----|
| 57 | Workflow used to analyze the Fontainebleau Sandstone thin section. First, the porosity (13%) is quantified, then contacts (22%), then cements (18%), and finally, grains are quantified. The scale bar is 200 microns. . . . .   | 71 |
| 58 | Post-test Fontainebleau-1-10 Sandstone thin-section image showing regions of interest. The sample was tested to a confining pressure of 2500 psi. An incipient failure surface can be seen in the thin-section. The black circles are the regions from which tiles were selected for detailed analysis. The scale bar is 0.2 in. . . . . | 71 |
| 59 | The analyzed image shows the sampled porosity, percentage cement, contacts between grains and sampled grains. The scale bar is 200 microns.  | 72 |
| 60 | Post-test Fontainebleau-1-9 Sandstone thin-section. The sample was run to a confining pressure of 2000 psi. The black circled regions indicate where the tiles were selected for analysis. The scale bar is 0.2 inch. . . . .  | 73 |
| 61 | The analyzed image shows the sampled porosity (12%), percentage cement (17%), contacts (26%) between grains, and sampled grains. The scale bar is 200 microns. . . . .   | 73 |
| 62 | Mean cracks as a function of the number of image tiles analyzed for the Fontainebleau 1.9 Sandstone sample. The mean stabilizes after segment number 6. . . . .  | 75 |
| 63 | The post-test image for Fontainebleau 1.10 Sandstone shows the cracks generated during a MST test. The scale bar is 1000 microns. . . . .  | 76 |
| 64 | The analyzed image for Fontainebleau 1.10 Sandstone shows the cracks drawn on the tile with a red line. The cracks are counted along with their orientation. . . . .   | 76 |

|    |  |    |
|----|--|----|
| 65 | There is an exponential relationship between the total number of cracks as a function of increasing stress stage. . . . .  | 77 |
| 66 | Pre-test Fontainebleau-3 Sandstone thin-section. The black circles are the regions from which the tiles were selected to be analyzed. The scale bar is 0.2 inch. . . . .   | 78 |
| 67 | The analyzed image for the Fontainebleau-3 Sandstone pre-test shows the sampled porosity (12%), percentage cement (15%), contacts between grains (27%), and sampled grains. The scale bar is 200 microns. . . . .                    | 78 |
| 68 | Post-test Fontainebleau-3.5 Sandstone thin-section. The black circles are the regions from which the tiles were selected to be analyzed. The scale bar is 0.2 inch. . . . .  | 79 |
| 69 | An analyzed image for the Fontainebleau-3.5 Sandstone sample post-test shows the segmented porosity(10%), cement volume (14%), contacts (29%) between grains, and identified framework grains. The scale bar is 200 microns. . . . . | 79 |
| 70 | Post-test Fontainebleau-3.4 Sandstone thin-section. The black circles are the regions from which the tiles were selected for analysis. The scale bar is 0.2 inch. . . . .  | 80 |
| 71 | A sample analyzed image for the Fontainebleau-3.4 Sandstone sample post-test shows the segmented porosity (9%), volume of cement (15%), contacts between grains (40%), and identified framework grains. . . . .                      | 81 |
| 72 | There is an exponential relationship between total number of cracks and the end stage stress. . . . .  | 83 |
| 73 | Pre-test Boise Sandstone thin-section. The black circles are the regions from which the tiles were selected for analysis. The scale bar is 400 microns. . . . .  | 84 |

|    |   |    |
|----|---|----|
| 74 | The analyzed image for the Boise Sandstone pre-test shows the sampled porosity, percentage cement, contacts between grains, and sampled grains. The scale bar is 400 microns. . . . .     | 84 |
| 75 | Post-test Boise Sandstone thin-section. The black circles are the regions from which tiles were selected for analysis. The scale bar is 0.2 inch. . . . .                                 | 85 |
| 76 | An analyzed image for the Boise-1.1 Sandstone sample post-test shows the segmented porosity, volume of cement, contacts among grains , and framework mineralogy. . . . .                  | 85 |
| 77 | Scan of post-test Boise Sandstone thin-section. The black circles are the regions where tiles were selected for analysis. . . . .   | 87 |
| 78 | An analyzed image tile for the Boise-1.2 Sandstone sample post-test illustrating the segmented porosity, volume of cement, contacts among grains, and framework grain mineralogy. . . . . | 87 |
| 79 | There is an exponential relationship between the total number of cracks and stress at each stage. . . . .   | 89 |
| 80 | Pre-test Miocene sandstone thin-section. The black circles are the regions from which tiles were selected for analysis. . . . .   | 90 |
| 81 | The analyzed image for Miocene sandstone pre-test shows the segmented porosity, volume of cement, contacts among grains, and framework grain mineralogy. . . . .                          | 90 |
| 82 | Post-test Miocene sandstone thin-section. The black circles are the regions from which tiles were selected for analysis. . . . .  | 91 |
| 83 | The analyzed image for Miocene sandstone post-test shows the segmented porosity, volume of cement, contacts among grains, and the framework grain mineralogy. . . . .                     | 92 |

|    |  |    |
|----|--|----|
| 84 | Post-test Miocene-3 sandstone thin-section. The black circle is the region from where the tiles were selected to be analyzed. . . . .  | 93 |
| 85 | An analyzed image tile for the Miocene-3 sandstone sample post-test shows the segmented porosity, volume of cement, contacts among grains, and the framework mineralogy. . . . .   | 93 |
| 86 | $M_1$ (dynamic data) vs contact ratio for different rock types. There is a linear relationship between $M_1$ and contact ratio. . . . .  | 96 |
| 87 | Maximum compressive strength (static data) vs. percentage cement for different rock types. There is a linear relationship between strength and cement volume. . . . .  | 96 |
| 88 | Total no. of cracks generated vs irrecoverable strains. There is no correlation between the number of cracks generated and the percent irrecoverable strain. . . . .   | 97 |
| 89 | Total number. of cracks generated, normalized to maximum shear stress vs. irrecoverable strains. There is an improved correlation between the number of cracks generated and percent irrecoverable strains. The higher the number of normalized cracks generated the larger the irrecoverable strains. . . . . | 98 |
| 90 | Total no. of cracks generated, normalized to maximum deviatoric stress and porosity vs. irrecoverable strains. There is an excellent correlation between the normalized number of cracks generated and percent irrecoverable strains. . . . .  | 98 |
| 91 | Total number of cracks generated, normalized to maximum deviatoric stress and porosity vs $M_2$ . A higher number of cracks generated corresponds to higher irrecoverable strains. . . . .   | 99 |

|    |  |     |
|----|--|-----|
| 92 | $M_2$ increases with increasing porosity and increases with decreasing cement volume. This is expected as higher porosity should be related to higher irrecoverable strains, and a higher $M_2$ . Higher cement results in lower irrecoverable strains and lower $M_2$ . . . . . | 100 |
| 93 | Comparison of original and predicted $M_2$ as a function of cements and porosity. The blue points are the raw data and red points are predicted data. Equation 33 fits the data very well. . . . .   | 101 |
| 94 | Comparison of original and predicted $M_2$ as a function of cements and porosity on 2D plots. The red points are the raw data and blue points are predicted data. . . . .  | 101 |

# Chapter 1: Introduction

## 1.1 Significance of Thesis

Extensive work has been done to understand the relationship between static and dynamic data. We have cited several of these studies in this chapter. The main areas in which this work provides new insights are:

- Quantifying the effects of sample characterization on static and dynamic properties. This has been achieved by doing a detailed image analysis of thin-section data.
- A systematic modeling methodology is presented in which the parameters are easier to obtain and use in predicting sample properties.
- Model is successfully applied to published data in the literature.
- Physical mechanisms have been identified that control modeling parameter.
- Several crack models have been published in the literature. These models are mainly based on correlations and empirical fits. In this study, we have looked at the generated cracks pre-test and post-test and have provided their physical interpretation in terms of modeling parameters.

## 1.2 Introduction

### 1.2.1 Static (large strain) Data Review

Static to dynamic correlations are locally dependent on mineralogy, texture, stress, and thermal history, porosity, and clay content (Al-Tahini and Tani, 2006; Edimann and Somerville, 1998). Al-Tahini and Tani (2006) measured the mechanical properties of sandstones using triaxial tests and related them with the presence of

cements. The cement volume was characterized using thin sections. They concluded that not only the presence of cement is significant but also to know where they occur in the rock matrix.

Quartz overgrowth plays a major role in increasing strength, while clay coatings play a minor role (Al-Tahini and Tani, 2006). Small amounts of cement can significantly impact both static and dynamic data, depending on its volume and distribution. Edimann and Somerville (1998) demonstrated that an increase in porosity results in a decrease in rock strength, and an increase in Poisson's ratio (ratio of radial strain to axial strain).

Commonly used material models also have limitations. The Modified Cam Clay (MCC) material model is one of the widely used models to predict static data (Roscoe and Burland, 1968). The model assumes that a rock behaves as a linear elastic material inside the yield surface. Generally, there are additional mechanisms present inside the yield surface such as non-linear elasticity and plastic strains (Bilal et al., 2015).

Walsh (1965) provided the conceptual basis of much of the work that has been published in the literature on crack propagation and modeling in rocks. The model discusses grains crushing and sliding as controlling mechanisms for grain deformation. Kachanov (1982) utilized the sliding approach and modeled penny shaped cracks. Fjaer et al. (2014) and David et al. (2007) have also applied the sliding mechanism to model the propagation of cracks along a uniaxial stress path. These models do not include a methodology to predict model parameters. There is also no incorporation of data from sample characterization.

A Staged Differential Effective Medium (SDEM) model was developed by Myers and Hathon (2014) to predict the compressibility of unconsolidated sands along a zero-lateral strain stress path. This work utilized the length scales defined by sample characterization to predict model parameters. In this work, we have extended this

model to the triaxial stress path. The model will be discussed in detail later. The next step is to calibrate the model parameters to the thin section and/or micro-CT data.

On a well scale, acoustic logs often provide the input data for the prediction of static properties. This upscaling allows the prediction of wellbore failure and sand control. Core data are required to build local correlations between static and dynamic properties. The usual upscaling issues are present when core data are used to derive the static to dynamic correlations. This emphasizes the need for models that are calibrated in terms of detailed sample characterization including: porosity, framework mineralogy, the presence and volume of cements, grain contact percent and orientation and post-test characterization of sample response.

The next level of upscaling is to map these properties on a field scale. This makes possible the calibration of geomechanical and 4D seismic models. If models are successfully derived based on mineralogy, texture, and stress history, this level of upscaling is much more likely to be successful, because they can be related to depositional models and sequence stratigraphy etc.

### **1.2.2 Dynamic (small strain) Data Review**

For sandstones, load bearing or structural clays will increase irrecoverable strain and slow the acoustic velocity (Hathon and Myers, 2012). Non-load bearing clays at small volumes, however, increase the modulus derived from dynamic data but do not affect the static stress strain response. In mudrocks, according to Hathon and Myers (2012), peak strength is directly related to the acoustic velocity. Polar anisotropy in GOM mudrocks ranges from 9-20% due to the interaction of depositional and compaction processes. This contrasts with the shale gas samples in which the anisotropy is around 40%. Anisotropy is an important input fracture modeling parameter. Hathon et al., (2016) modeled the acoustic anisotropy in unconsolidated sands using thin

sections and micro-CT data. They concluded that in thrust belt settings, where the principal stress is non vertical, average anisotropy was 15%.

In dry rock, a linear relationship is observed between reciprocal acoustic wave velocity (travel time) and porosity (Mavko, 2009). Myers and Hathon (2009) developed SDEM models for acoustic velocity. The model allows continuous interpolation between iso-strain (parallel) and iso-stress (series) averages of the moduli. The model provides an intuitive interpretation of the modelling parameter in terms of the porosity dependence of the Biot parameter. Contact length is also related to the modeling parameter.

Gassman (1951) equation provide a simple model to estimate fluid saturation effect on dynamic data. Change in bulk modulus can be calculated as a function of fluid saturation, provided the rock fluid, dry and saturated frame moduli are known. The relationship is given by

$$\frac{K_{sat}}{K_{solid} - K_{sat}} = \frac{K_{dry}}{K_{solid} - K_{dry}} + \frac{K_{fluid}}{\phi(K_{solid} - K_{fluid})}. \quad (1)$$

The assumptions are that the material is isotropic and elastic, the pore space is well connected and the medium is a closed system with no pore fluid movement across boundaries.

Domenico (1977) modified Gassman (1951) equation and concluded that the rate of porosity change is proportional to the differential pressure raised to a power n. The value of exponent n is approximately 1/4 for the compressional wave velocity of the gas saturated specimen and the shear wave velocity of both gas and brine saturated specimens. For the compressional wave velocity of brine saturated specimens, the value of n is around 1/18. The compressional wave velocity increases by a factor of 2.2 at 400 psi if gas is replaced by brine. The factor reduces to 1.3 as differential pressure is increased to 5000 psi. Gas saturated shear wave velocities are a little higher than brine saturated shear wave velocities due to the difference in bulk density. The shear

modulus, derived from shear wave velocity, increases non-linearly with increasing differential pressure. The value of Poisson's ratio for brine saturated rocks ranges from 0.4 to 0.5. On the other hand, the value for gas saturated rocks is in the range of 0.1 to 0.15.

Domenico (1977) also concluded that although the compressional wave velocity is primarily a function of differential (deviatoric) stress rather than confining or pore fluid pressure, a variation of pore fluid pressure does modify velocity slightly. Compressional wave velocity of gas saturated samples and shear wave velocity of both gas and brine saturated samples depend solely on differential pressure.

Effective fluid compressibility derived from the compressional wave velocity was found generally to be between theoretical values given by the direct weighting and inverse weighting of the gas and brine. Direct weighting means, weighting by volume average of the compressibility and inverse weighting means the average of incompressibility.

Experimental results have shown that dispersion (variation of velocity as a function of frequency) is negligible in rocks between logging tool khz and lab tool MHz frequency (Mavko et al., 2009). Biot (1956) theory does not predict these experimental observations. Biot (1956) assumed that the attenuation in the propagation of waves arose due to the viscosity of pore fluid. Plona (1980) offered a different mechanism caused by the relative movement between the fluid and grain boundaries known as squirt flow.

Composite models have been used quite often in predicting static and dynamic properties. They use a combination of acoustic velocity data and a distribution of aspect ratios of the ellipsoidal cracks to predict rock properties. Coyner and Cheng (1984) predicted the change in porosity with pressure within 0.1% of the measured change in porosity for sandstones. They observed the P and S wave velocity for dry and saturated Berea sandstones. Shear wave velocity for the Benzene saturated rock

was very close to the dry rock. At low stress, the saturated shear wave velocity was higher than the dry velocity. The saturated P wave velocities were higher than the dry velocities at all stresses.

Coyner and Cheng (1984) developed the composite model by extending the velocity model of Toksoz and Kuster (1974) and Toksoz and Chen (1979). They used a spectrum of aspect ratio ellipsoidal cracks. However, it's not easy to predict the model parameters, and they only apply to a low porosity rock.

### 1.2.3 Static Versus Dynamic Data

Static and dynamic moduli are typically different from one another (Simons, Brace, 1965) with dynamic modulus almost always being greater than static modulus. One of the reasons could be the contribution of pore fluid (Biot, 1956). This difference is usually small in lithified rocks. Montmayeur and Graves (1985) concluded that elastic rock properties are a strong function of maximum historical stress. Grazielle (2017) found an order of magnitude difference between the static and dynamic compressibility of Middle East carbonates.

Gassman (1951) was the first to propose a relationship between constituent properties (grain, frame and fluid modulus) and acoustic velocity. For reservoir rocks, Graves (1982) had some success in correlating dynamic and static rock properties using modified Gassman relations. Geertsma (1961) showed that Gasmann (1951) relationships are low frequency limit of Biot's relationships. He also concluded that the time average approximation that is used to predict porosity using acoustic velocity is not accurate.

Even in gas saturated rocks, there is a significant difference between static and dynamic data (King 1970). The dynamic moduli are higher than the corresponding static moduli. The ratio of these moduli decreases as the mean stress increases.

The difference between static and dynamic moduli is greater perpendicular to the

bedding plane than parallel to it. There is often a correlation between the static and dynamic ratio and the non-linear elastic behavior of rocks (Yale et al. 1995). Grain contact adhesion and stick-slip sliding mechanisms have been proposed to explain this relationship. These results imply that grain contact models should be useful in understanding and quantifying static and dynamic differences (Walsh, 1965; Tutuncu et al., 1995; Fjaer et al., 2014). Yale et al. (1995) also concluded that grain contact and cementation control static and dynamic differences. They further illustrated that cement type also plays a role in the static and dynamic differences with weaker chlorite cemented samples showing larger static and dynamic differences than fully quartz cemented samples.

Jizba (1990) found that both lithology and stress dictated the relation between static and dynamic moduli in tight gas sandstones. He characterized the lithology into sandstone, load bearing clays and dispersed clays. Static and dynamic moduli can also help distinguish between sandstone and shales. Jizba (1990) concluded two types of behavior: In shales (clay greater than 20 percent), he found that the ratio of dynamic to static moduli is rather insensitive to confining stress due to inelastic behavior. The ratio ranges between 1.1 to 1.6. In contrast, in sandstones and framework clay bearing sandstones (clay less than 20 percent) he observed a strong dependence of the ratio of dynamic to static moduli on confining stress. This behavior may be attributed to the differing sensitivity of static and dynamic moduli to the presence of cracks.

The difference between static and dynamic data has also been attributed to the difference in strain amplitude (Martin and Haupt, 1994). Martin concluded that for granite rock strains greater than 5 micro strains, the stiffness of the cracks decreases, and Young's Modulus decreases. This effect is explained due to slip on contacts between the surfaces. Surface forces at crack tips are essential for small strain excursions contributing to the higher dynamic moduli.

Olsen (2008) performed experiments on North Sea chalk and showed that the

dynamic and static modulus depends on the magnitude of strains associated each modulus. Similar results are also observed in this work.

Static and dynamic moduli are only equal at the beginning of the loading and unloading stress path where the strains are small (Fjaer, 2009). This observation was also made by (Walsh, 1965). The model by Walsh (1965) qualitatively explains the difference between static and dynamic Young's modulus. The velocity data corresponds to the superposition of small alternating stress on the existing applied stress. The static value is usually the slope of stress and strain curve at some arbitrarily selected value of applied stress. On the other hand, the modulus calculated from the sonic velocity corresponds to some average slope of the loop representing the sound wave. Thus, the dynamic value would be somewhat higher than the static value.

Rock elastic properties are a function of the maximum stress applied to the rock. Static compressibility is higher at higher stresses than dynamic compressibility (Montmayeur and Graves 1985). Rocks mineralogy and distribution of minerals is also one reason that only local correlations between static and dynamic properties have been developed. Knowing just the mineralogy is not enough. Both static and dynamic moduli are anisotropic (Hamza et al. 2018). Hamza (2018) also showed that for both static and dynamic Young's moduli, the horizontal modulus was greater than vertical.

#### **1.2.4 Difficulties in Characterization and Modeling of Static and Dynamic Data (It's not trivial)**

The static and dynamic data depend on many different rock properties including porosity, clay content, cement, contact modulus, and stress history, etc. Porosity affects both static and dynamic data. Porosity is usually inversely related to peak strength and acoustic wave velocity. Load bearing clays increase irrecoverable strains, and non-load bearing clays impact velocity. Peak strength is sensitive to small volumes of cement. Cement type also plays a role in the static and dynamic differences

with weaker chlorite cemented samples showing more significant static and dynamic differences than fully quartz cemented samples. The contact modulus significantly impacts the dynamic data. With production of irrecoverable strains inherent in static data, rock is different at every stress.

The dynamic Young's modulus is typically greater than or equal to the static Young's modulus and is believed to depend on stress path. The difference between the two moduli typically increases as the strains become larger due to the production of micro cracks with increasing stress. There are additional mechanisms contributing to this difference include grain rotation and ductile deformation. There can be an order of magnitude or more difference between static and dynamic moduli at large strains. The presence of pore fluid also increases the difference between static and dynamic data. For this reason, gas saturated samples are typically measured.

Commonly used material models also have limitations. The MCC model is one of the most widely used models to predict static data. The model assumes that a rock behaves as a linear elastic material inside the yield surface. Generally, there are additional mechanisms present inside the yield surface such as non-linear elasticity (opening and closing of micro-cracks) and plastic strains (ductile deformation, grain rotation).

Several crack models have been published in the literature to predict static data. These models are extensions of the work published by Walsh (1965). These extended models include grains crushing and sliding as controlling mechanisms for sample deformation. Kachanov (1982) utilized the sliding approach and modeled deforming penny shaped cracks. Fjaer et.al (2014) and David (2007) has also applied the sliding mechanism to model the propagation of cracks along a uniaxial stress path. These models do not include a methodology to predict model parameters. There is also no incorporation of data from sample characterization. Composite models have been used in predicting static and dynamic properties. They use a combination of acoustic

velocity data and a distribution of aspect ratios of the ellipsoidal cracks. It is difficult to predict the model parameters, and they apply only to low porosity samples.

### 1.3 Terminology and Definition

We now introduce the concepts of stress and strain and Hooke's law. We define the point of positive dilatancy (PPD) and its connection with multistage triaxial tests. Also, in this section, we provide an elementary discussion of plasticity parameters: recoverable and irrecoverable strains, friction, and dilatancy. These concepts are used in the data analysis section.

#### 1.3.1 The Stress-strain Curve

An example of a typical stress: strain curve is shown in Figure 4. A sample under confining stress that is exposed to an axial load often initially exhibits linear elastic behavior. Linear elasticity is the most basic of all material models. Only two material parameters need to be experimentally determined: the Young's modulus and the Poisson's ratio. This region may be as small as  $10^{-6}$  strain for a ductile rock to approximately one percent, or  $10^{-1}$  strain for more lithified samples. By definition elastic strain is recoverable, meaning that the sample rebounds completely when unloaded (i.e. there is no permanent change in shape or volume). Elastic strains include compression of grain contacts, the elastic deformation of grains, and the opening and closing of compliant pores. In this region, if the sample is unloaded the measured stress-strain path retraces the initial loading curve. With continued loading and increased axial strain, the stress-strain paths for loading and unloading diverge, and some of the strain is not recovered. The missing strain is called irrecoverable, which is the measure of permanent sample deformation. The mechanisms include, among others, grain sliding (Fjaer et al., 2015), grain rotation, grain cracking, displacement or translation, and permanent ductile grain deformation. With increments of loading,

the sample often reaches the failure point, also known as the maximum compressive strength (MCS). At this point, the sample unloads with further applied axial strain . Depending on a sample's previous stress and thermal history, mineralogy, and texture, this point may never be reached, or require very high axial strains  $\geq 10\%$ . The details of the post failure stress-strain curve depend on the mode of failure and the details of the sample makeup. A typical axial stress versus axial strain plot is shown in Figure 1.

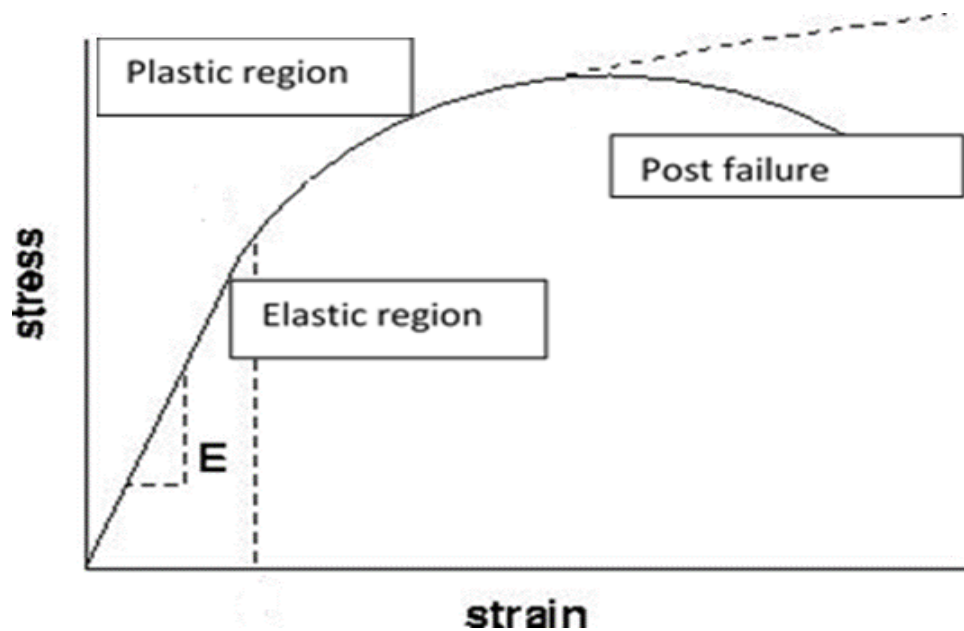


Figure 1: The figure shows typical stress-strain behavior of rock under increasing axial stress. The three regions exhibited are defined by the magnitudes of the recoverable and irrecoverable strains.  $S$  is the slope of the stress strain curve and referred to as the sample stiffness. If the region is assumed to be elastic, the stiffness is equal to Young's modulus ( $E$ ).

### 1.3.2 Deviatoric Stress

Deviatoric stress is defined as the difference between the axial stress and radial stress. This stress is commonly associated with failure in rocks in models such as Mohr-Coulomb (Mohr, 1882), Drucker-Prager (Drucker, 1952), etc.

### 1.3.3 Strain and its Relation to the Point of Positive Dilatancy

A constant axial strain rate is the axial loading parameter used in all the measurements in this thesis. This allows to calculate Young's Modulus or stiffness over a constant strain range. constant stress is another typically used method, however it is harder to stop the sample before failure when using it. The ratio of the radial strain to the axial strain is called Poisson's ratio. The strain in rock samples is often expressed in millistrain. If  $L_o$  and  $r_o$  represent the original length and radius, then the axial engineering strain is calculated by normalizing the total axial displacement to the sample's original length (Beer et al. 2009). This is given by

$$\epsilon_a = \frac{\delta L}{L_o}. \quad (2)$$

The engineering radial strain is given by

$$\epsilon_r = \frac{\delta r}{r_o}. \quad (3)$$

Engineering volumetric strain is defined as the change in volume divided by original volume,

$$\epsilon_v = \frac{\delta v}{v_o}. \quad (4)$$

The relation between volume strain, radial and axial strain for infinitesimal strains is shown by application of Hooke's law,

$$\epsilon_v = 2\epsilon_r + \epsilon_a. \quad (5)$$

A smaller sample results from a positive strain by convention, while conversely, a negative strain means that the sample is getting larger. Figure 4 shows deviatoric stress plotted against volumetric strain for a typical triaxial measurement. Initially,

the volumetric strain is positive (smaller sample). At larger axial strains, the volume strain goes negative. The point at which the volumetric strain changes sign is the point of positive dilatancy. We have used this point as the criteria to end the axial strain loading ramps in a multistage triaxial test.

### 1.3.4 Modulus

We need relationships between the various measures of sample stiffness, and they are defined below (Birch, 1961).

- **Bulk modulus,  $K$** , is the ratio of isostatic stress to volumetric strain under an isostatic stress path.
- **Shear modulus,  $\mu$** , is the ratio of shear stress to shear strain.
- **P wave modulus,  $M = \rho V_p^2$** , is the ratio of axial stress to axial strain for a plane wave or uniaxial-strain path.
- **Young's modulus,  $E$** , is the ratio of axial stress to axial strain for a constant radial stress boundary condition. Young's modulus is calculated using Hooke's law from the compressional and shear velocity and is given by

$$E = \frac{3 * (V_p/V_s)^2 - 4}{(V_p/V_s)^2 - 1} * V_s^2 * \rho. \quad (6)$$

Where  $V_p$  and  $V_s$  are the compressional and shear wave velocity, and  $\rho$  is the bulk density.

- **Poisson's ratio** is defined as the negative ratio of radial to axial strain, for a constant radial stress boundary condition,

$$\nu = -\frac{\epsilon_r}{\epsilon_a}. \quad (7)$$

## 1.4 Mohr-Coulomb failure criteria

(Mohr,1882)

The Mohr-Coulomb failure criterion is one of the commonly used methods to predict failure. It states that there is a linear relation between the normal stress ( $\sigma_n$ ) and the shear stress ( $\tau$ ) is given by

$$\tau = \mu\sigma_n + C_o. \quad (8)$$

Recalling from the basic physics related to friction force, the factor ( $\mu$ ) is the friction coefficient related to the applied normal stress, and ( $C_o$ ) is called the inherent shear stress that represents the cohesion of the sample along the sliding plane. Equation 8 can be written in terms of axial stress ( $\sigma_y$ ) and confining stress ( $\sigma_x$ ) as

$$\frac{(\sigma_y - \sigma_x)}{2} = \mu \frac{(\sigma_y + \sigma_x)}{2} + C_o. \quad (9)$$

This is also called p-q plot where

$$p = \frac{(\sigma_y - \sigma_x)}{2}, \text{ and} \quad (10)$$

$$q = \frac{(\sigma_y + \sigma_x)}{2}. \quad (11)$$

Using this plot, we can graph the direct measured quantities and find the slope ( $\mu$ ) and the intersection ( $C_o$ ). The slope is usually represented in terms of an angle as

$$\theta = \sin^{-1}\mu. \quad (12)$$

## 1.5 Triaxial Test

By definition, a standard triaxial test is performed at a constant confining pressure. The loading parameter is usually a constant axial strain rate. Brittle samples at failure have dramatic results if the equipment is controlling on axial load. As the axial strain increases, the deviatoric stress increases until the sample reaches its maximum compressive strength (MCS). Figure 2 shows typical triaxial stress-strain data. The purple line shows a constant confining pressure of 1000 psi. There are also unload and reload cycles of the deviatoric stress to measure irrecoverable strains and the unloading and reloading Young’s modulus and Poisson’s ratio.

## 1.6 Multistage Triaxial Test (MST) Methodology

In this work, we deviate from the standard triaxial test measurement protocol by using “multistage” triaxial testing protocol. A multistage test is like a standard triaxial test except that it has multiple loading stages at different confining pressures. Instead of increasing the axial load of the sample to the maximum compressive strength (MCS), i.e., failing the sample, the loading is stopped at the point of positive dilatancy (PPD). The sample is then unloaded, and the confining pressure is increased. The same cycle is repeated at the increased confining pressure. This means that the yield surface is encountered at multiple points during a single MST measurement. This eliminates the sample “twinning” problem, i.e., the lack of repeatability inherent in single stage triaxial tests.

Figure 3 shows the stress path for our implementation of an MST. The red curve is at a lower confining stress than the blue. The PPD is the point at which the radial strain to axial strain ratio reaches one-half, or equivalently the volume strain is independent of an axial load, as shown in figure 4.

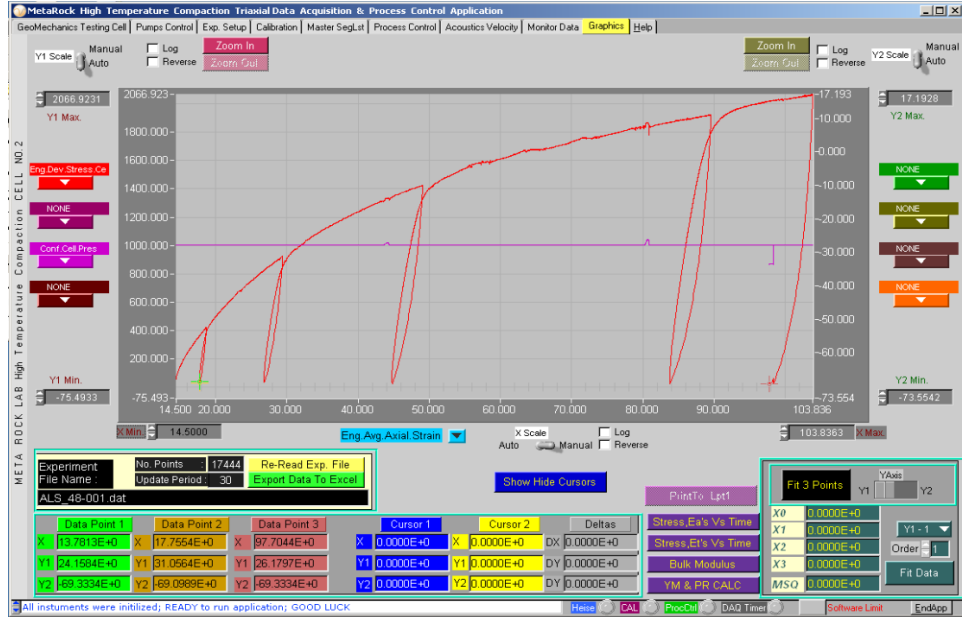


Figure 2: Data for a typical triaxial test. The deviatoric stress is plotted on the vertical axis. The axial strain is plotted on the horizontal axis. This is a conventional triaxial test where the confining stress is held constant throughout.

The PPD was chosen because it is a well-defined point that is easily picked during the experiment and found to be easily corrected to the maximum compressive strength. Al-Salman and Myers (2015) found that the maximum compressive strength is equal to 1.2 times the axial stress where the PPD occurs for a broad range of samples (recoverable strains ranging from ten percent to ninety percent).

Earlier techniques used different unloading points to perform an MST. The unloading point used in the ISRM standard is at the maximum compressive strength, i.e., where the slope of the axial stress-strain curve is zero (Kovari, Tisa 1975). This occurs at higher stress than the PPD. When this point is used, it is problematic to stop the axial ramp before sample failure, and significantly more sample damage is induced at each confining step. It is not clear how this damage affects the measure MCS. Taheri and Tani (2008) used a lower unloading point using the maximum value for Young's modulus ( $E(\text{secant}) = \max$ ). This point is at a lower stress than the point of positive dilatancy. There would be a larger correction factor to estimate the max-

imum compressive strength than using the PPD. To our knowledge, this correction factor has not yet been developed.

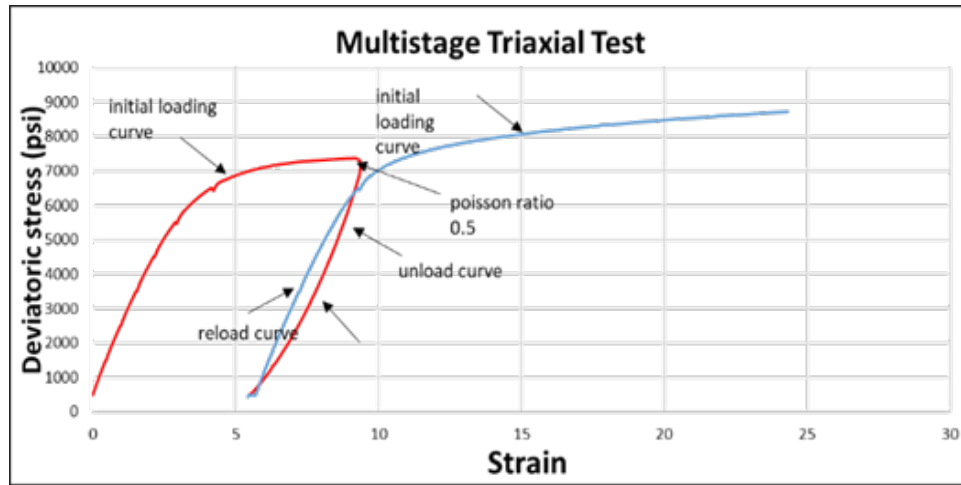


Figure 3: A typical MST stress path. The red curve is at a lower confining stress than the blue. The point of positive dilatancy (Strain Ratio = 0.5) is indicated where the unload cycle begins

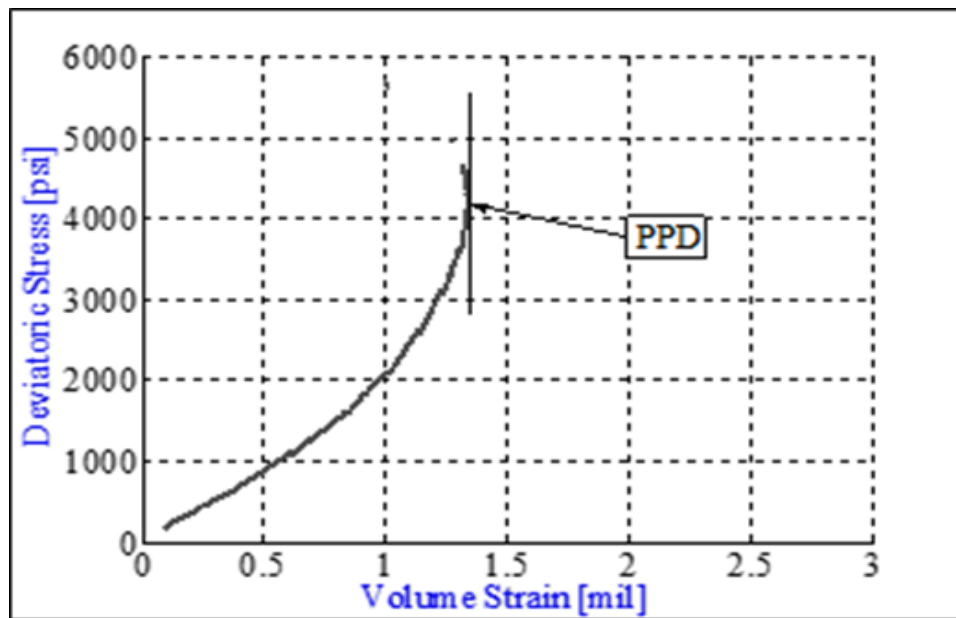


Figure 4: The point of positive dilatancy (PPD) used for multi-stage triaxial (MST) tests. Sample unloading begins once this point is reached

The PPD has been chosen for the MST instead of the two other unloading points. It represents a compromise between them. Using PPD, the sample damage appears

to be minimal, and the data are easily corrected (Al-Salman, Myers, Sharf-Aldin, 2015). This point also has the advantage that different operators can choose it or even automate it with good repeatability.

### 1.6.1 Irrecoverable Strain

Figure 5 shows the plot of confining stress versus axial strain for a multistage triaxial test. Similar plots may be made for the radial strain. In Figure 5, the recoverable and irrecoverable strain is delineated. The percent irrecoverable strain is defined as the ratio of the irrecoverable strain to the total strain during each stress cycle. The percent irrecoverable strain is a total accumulated strain because the sample is unloaded to a common low deviatoric stress at each confining stress. We did not observe any significant variation as a function of confining stress for any of the samples. Therefore an average percent irrecoverable strain value is used.

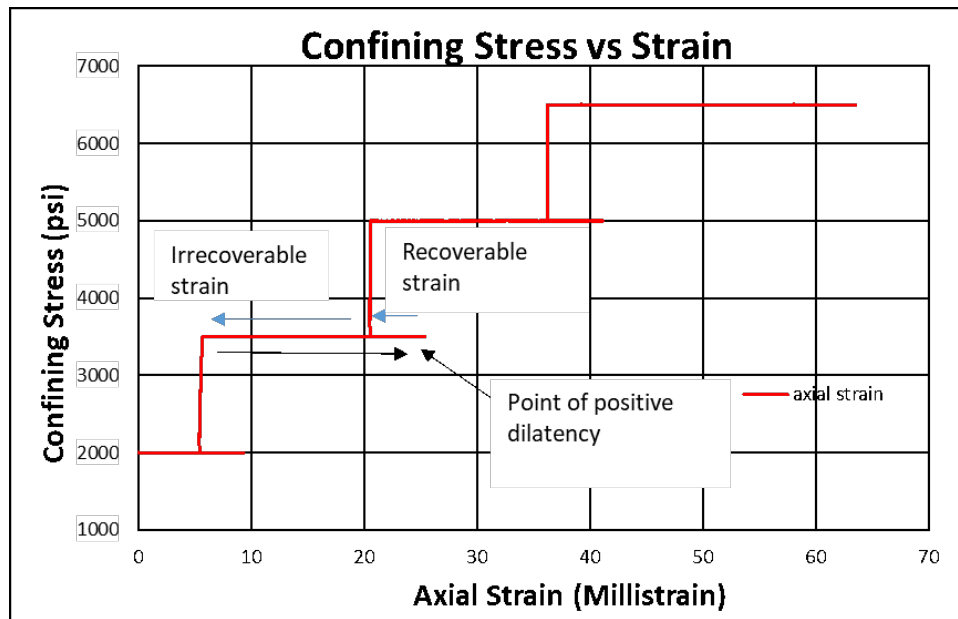


Figure 5: Confining stress versus axial strain for Austin Chalk. This plot is easily interpreted for the percent irrecoverable strain

## Chapter 2: Experimental Analysis

The data was measured using a multistage triaxial test (MST). The testing methodology for MST was discussed in section 1.6. This chapter discusses the experimental data, and data analysis.

### 2.1 Experimental Setup and Stress Protocol

This section discusses the experimental equipment and the standard testing protocols for a triaxial test. Young's modulus ( $Y_m$ ) is the derivative of the axial strain to axial stress along an elastic response curve when the radial stress is held constant. This stress path is commonly referred to as a "triaxial test." A typical experimental setup for a triaxial test is shown in Figure 6. The sample used was a right cylinder, two inches in length and one inch in diameter, oriented perpendicular to the bedding or vertical plug. ASTM (2014) guidelines were followed to setup triaxial testing protocols. All the samples used for this study were measured equilibrated to ambient humidity and temperature. The velocities were measured using standard "pitch and catch" techniques with torsional shear and compressional piezoelectric plates. The loading parameter is a constant axial strain rate of five milistrains per second. The deviatoric stress was measured using an internal, vented load cell. A two point axial strain measurement was made using internal, vented LVDTs. A two point radial strain measurement was made using a cantilever bridge, comprising four arms with the strain gauges mounted in a Wheatstone bridge configuration.

The experimental error in the static data is approximately five percent for the axial data and ten percent for the radial data based on calibration to aluminum. The error in the dynamic data is approximately one percent for compressional velocities and approximately three percent for shear velocities, based on aluminum and Lucite standards. The equipment was corrected for axial strain compliance and confining

stress effects using a tungsten carbide billet.

The assembly shown in figure 6 is placed inside the cylindrical pressure vessel shown in figure 7. The pressure vessel is filled with confining fluid (mineral oil) to apply the radial stress.

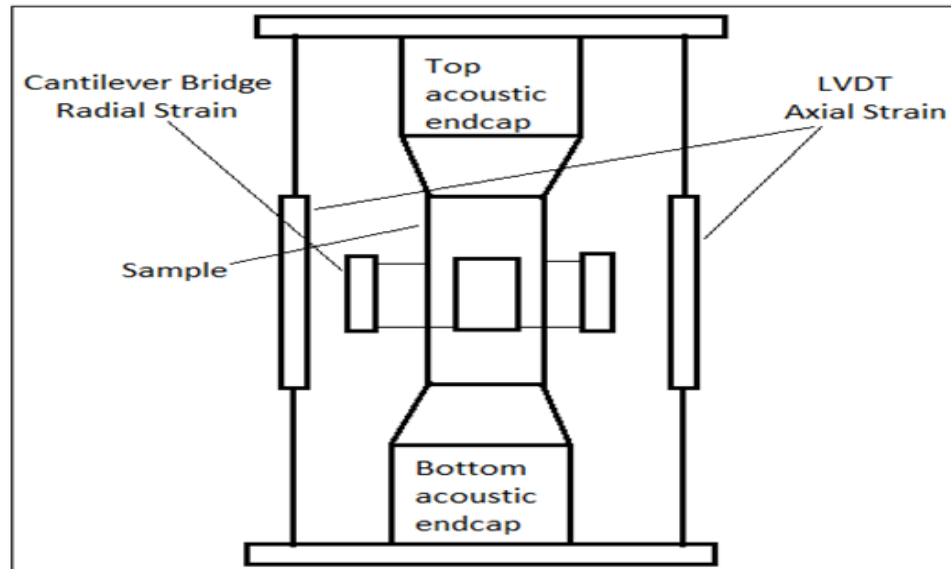


Figure 6: A typical experimental setup for a tri-axial test. Internal measurements of axial strain, radial strain and load are performed.



Figure 7: The cylindrical pressure vessel in which the sample assembly is placed. The maximum confining pressure is 12000 psi which is applied by displacement pumps under PID (proportional integral differential) control.

The internal load cell is located on the bottom of the vessel and is used to measure the axial load. This load is applied through a 1 1/2 inch diameter piston using a ball screw press. Figure 8 is a picture of the experimental setup.



Figure 8: Experimental setup including the computerized control panel. The entire apparatus is PID controlled and capable of 75000 lb. axial load and 12000 psi confining stress.

## 2.2 Multistage Triaxial Test

In this section, we discuss the experimental results. Multistage triaxial tests have been performed on a suite of different rock types. The samples are initially equilibrated at 500 psi radial (confining) stress and 600 psi axial stress (100 psi deviatoric stress). The tests were all performed using a constant strain rate loading parameter. The static data was measured at equal time intervals, which implies that the strain between two consecutive points is a constant value.

The velocities were measured at deviatoric stress intervals of 1000 psi. A three-point derivative of the stress-strain curve, which straddles the velocity measurements, was used to calculate the static Young's modulus. In this way, we obtain both static and dynamic Young's modulus at the same average stress (or strain) point on the

stress-strain curve.

Figures 9 to 13 show the “fountain plots” for Austin chalk, Berea and Castlegate Sandstone. The author originally measured these three samples, and the data are published in the master’s thesis (Bilal, 2016). A fountain plot consists of the axial, radial, and volumetric strains displayed on the same plot. Positive radial strains indicate that the sample is getting smaller whereas, the negative radial strains indicate that the sample diameter is becoming larger. Plots for the Austin Chalk and Berea Sandstone illustrate the range in sample properties measured (stiffness, MCC,  $Y_m$ , irrecoverable strain). The Berea and Austin Chalk show very different stress effects on the initial slope of stress-strain curve (stiffness), with the Berea showing more sensitivity to confining stress than the Austin Chalk. This effect is currently under investigation.

### **2.2.1 Austin Chalk**

Figure 9 shows a fountain plot for a test conducted on the Austin Chalk. The Austin Chalk is an Upper cretaceous geologic formation in the Gulf Coast region of the United States. It is named for outcrops near the type locality in Austin, Texas. The Austin Chalk consists of recrystallized, fossiliferous, interbedded chinks, and marls (Weishampel, 1990). Outcrops of the Austin Chalk can be seen throughout Dallas extending into Austin and San Antonio. The water depth during deposition of the Austin Chalk is estimated to be on the order of 820 ft. (Weishampel, 1990). The MST was run at confining pressures of 500, 2000, 3500, 5000, and 6500 psi. There is a significant effect of confining stress on sample stiffens. The nonlinearity near the PPD is quite high. This is consistent with the highly ductile nature of the material.

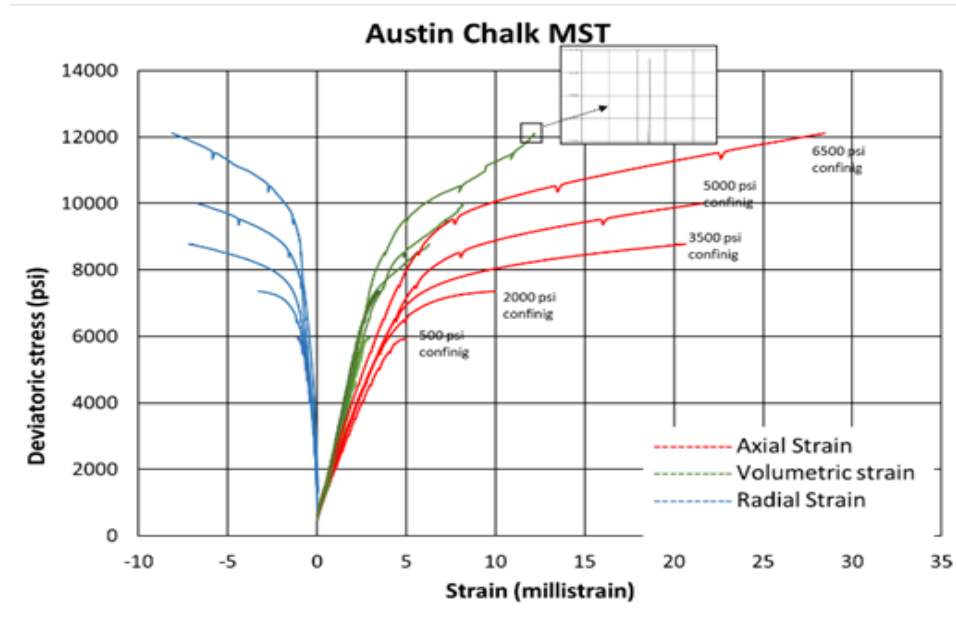


Figure 9: The Fountain plot for Austin Chalk showing deviatoric stress vs. axial, radial, and volumetric strain. The inset shows that the PPD has been reached. This is the most ductile sample measured exhibiting 20 percent irrecoverable strain.

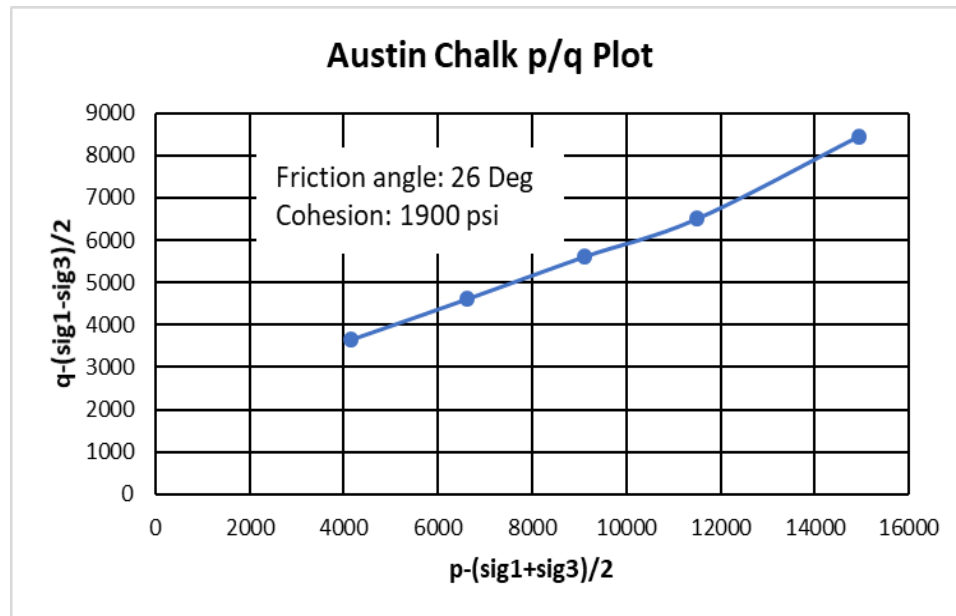


Figure 10: The p/q plot for Austin Chalk, the friction angle is 26 degrees and the measured cohesion is 1900 psi. Due to the ductile nature of this material the actual cohesion may be much lower (nonlinear yield criteria).

The p/q plot for Austin chalk is shown in figure 10. The friction angle is 26 degrees, and the measured cohesion is 1900 psi. Due to the ductile nature of this

material, the actual cohesion may be much lower (nonlinear yield criteria).

Table 1: Austin Chalk sample dimensions and weight.

| <b>Parameter</b> | <b>Value</b> |
|------------------|--------------|
| Length           | 1.962 in     |
| Diameter         | 0.986 in     |
| Weight           | 51.55 g      |

### 2.2.2 Berea Sandstone

Berea Sandstone is named after the town of Berea, in Cuyahoga County, Ohio where it is quarried to use as a grindstone. It is a very fine grained sandstone with grains being angular rather than rounded . The grains are predominantly composed of quartz held together by silica cement. (Andrews 1870). Figure 11 shows the fountain plot for Berea sandstone. Table 2 contains the sample dimensions and weight.

Table 2: Berea sandstone sample dimensions and weight.

| <b>Parameter</b> | <b>Value</b> |
|------------------|--------------|
| Length           | 2.042 in     |
| Diameter         | 1.014 in     |
| Weight           | 59.65 g      |

For Berea, the multistage triaxial test was performed at confining pressures of 1000, 2000, 3000, and 4000 psi. Figure 11 is the “fountain plot” for this MST test. A fountain plot contains axial, radial, and volumetric strain plotted simultaneously. As shown, the radial strains are negative because the sample diameter is increasing. There is a significant effect of confining pressure on the slope of axial stress versus strain data. The stiffness increases with increasing confining pressure. This is interpreted as due to the closing of compliant pores.

Figure 12 is the p/q plot for Berea sandstone. The friction angle is 36 degrees, and the cohesion is 2200 psi. As expected, both friction angle and cohesion are higher than Austin chalk.

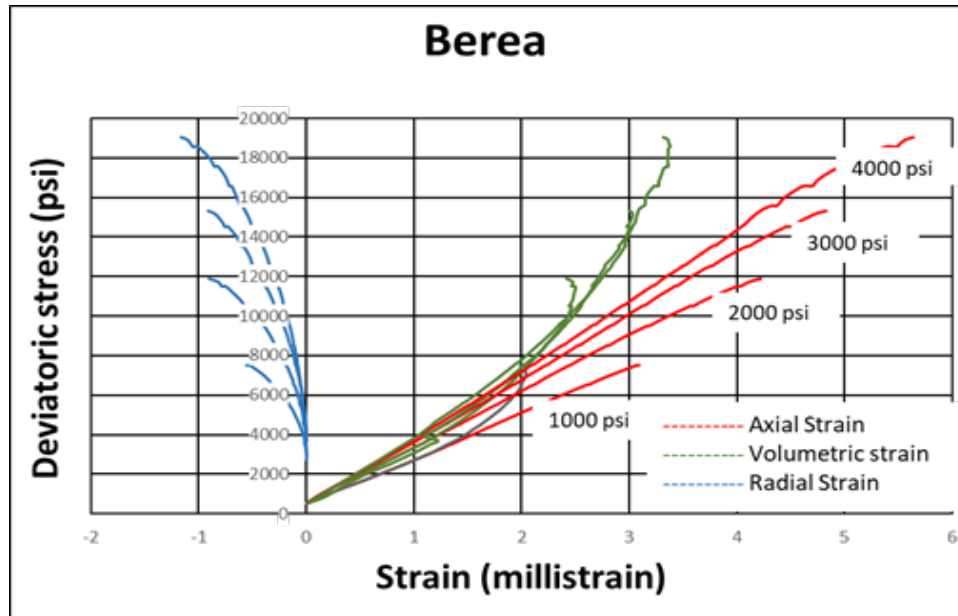


Figure 11: Fountain plot for a sample of the Berea Sandstone showing deviatoric stress vs axial, radial and volumetric strains. This is the least ductile sample measured, exhibiting only 5 percent irrecoverable strain.

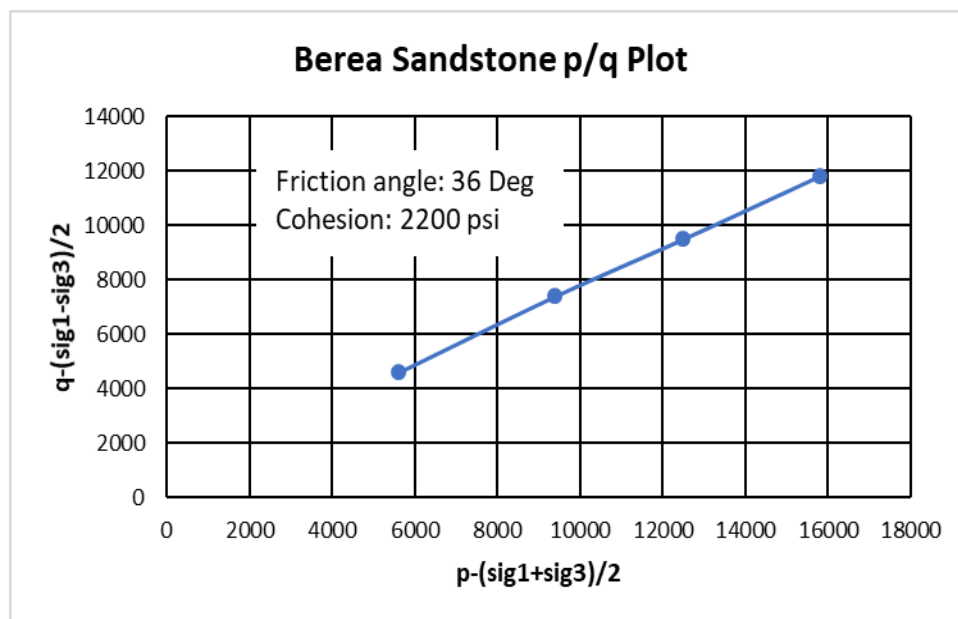


Figure 12: The p/q plot for Berea Sandstone, the friction angle is 36 degrees and the measured cohesion is 2,200 psi.

### 2.2.3 Castlegate Sandstone

Figure 13 is fountain plot for a test conducted on the Castlegate Sandstone. Castlegate Sandstone is a Mesozoic aged geologic formation that outcrops in Utah, USA. For Castlegate Sandstone, the multistage test was performed at eight different confining pressures ranging from 1000 psi to 6500 psi. Table 3 contains the sample measurements.

Table 3: Castlegate Sandstone sample dimensions and weight.

| Parameter | Value    |
|-----------|----------|
| Length    | 1.946 in |
| Diameter  | 1.023 in |
| Weight    | 49.38 g  |

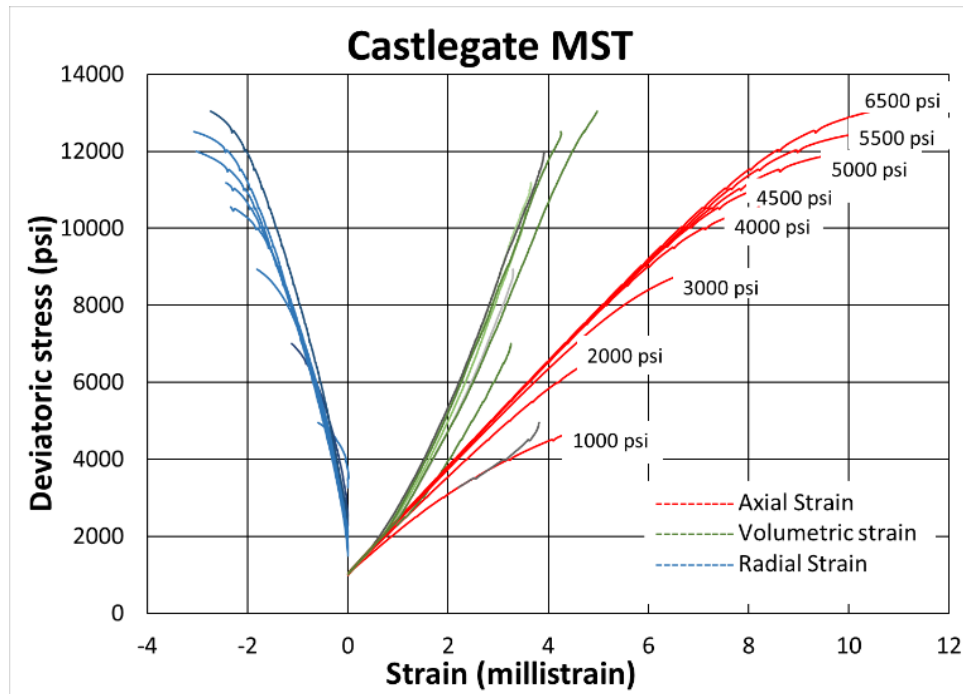


Figure 13: Fountain plot for Castlegate Sandstone showing deviatoric stress vs axial, radial and volumetric strain. The irrecoverable strain is 15 percent

The p/q plot for Castlegate Sandstone is shown in Figure 14. The maximum compressive strength was obtained by multiplying the deviatoric stress at the point

of positive dilatancy by 1.2 (Al-Salman and Myers, 2014). The friction angle is 30.4 degrees; the cohesion is 1192 psi. These numbers are both less than the values obtained for the Berea Sandstone. This sample had a more ductile failure than the Berea. This is evident by the increased nonlinearity near the PPD.

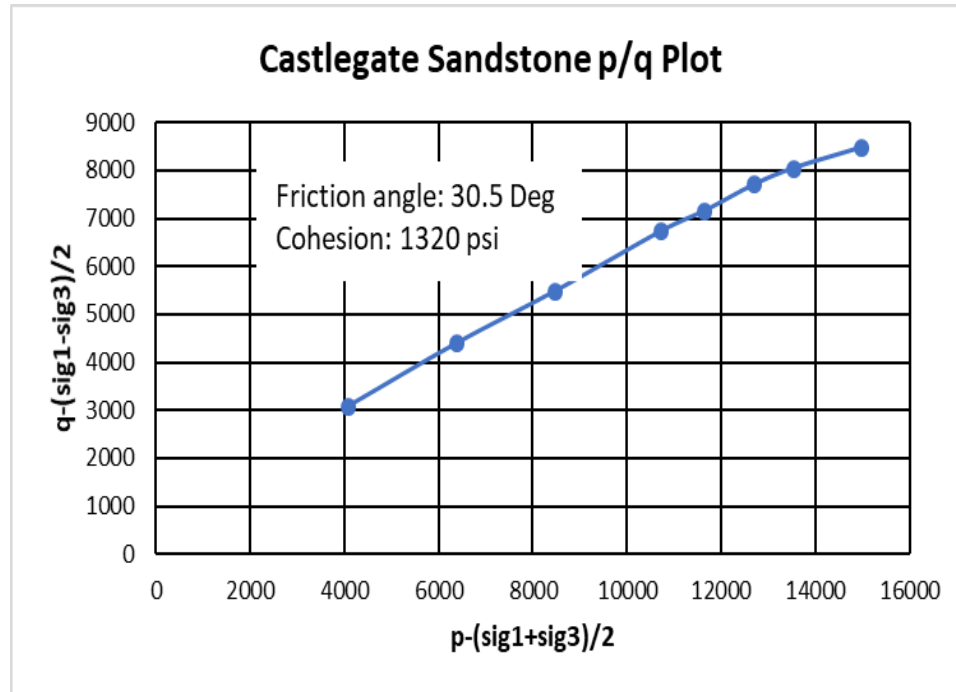


Figure 14: The p/q plot for Castlegate Sandstone, the friction angle is 30.5 degrees and the measured cohesion is 1320 psi.

#### 2.2.4 Boise Sandstone

Figure 15 shows the results for sample Boise 1.1 of the Boise Sandstone MST run at confining pressures up to 3000 psi. Figure 17 shows results for sample Boise 1.2 of the Boise Sandstone MST, which run up to an intermediate confining pressure of 2000 psi. These samples are considered twins for testing purposes. These samples provided us with the opportunity to analyze the induced damage in two similar samples, which were run to two different ultimate confining pressures. Micro-CT and thin section data have been used to analyze the damage in post-test samples. These results are discussed later in the sample characterization chapter of the thesis. Table 4 contains

the sample measurements for Boise-1 Sandstone.

For the Boise-1.1 Sandstone sample shown in figure 15, the test was run at confining pressures of 500, 1000, 1500, 2000, 2500, and 3000 psi. The sample stiffness is fairly constant with increasing confining pressure. The nonlinearity near the PPD is quite high, similar to Austin chalk. This is consistent with the highly ductile nature of the Boise Sandstone.

Table 4: Boise 1 Sandstone sample dimensions and weight.

| Parameter | Value    |
|-----------|----------|
| Length    | 2.014 in |
| Diameter  | 1.025 in |
| Weight    | 51.38 g  |

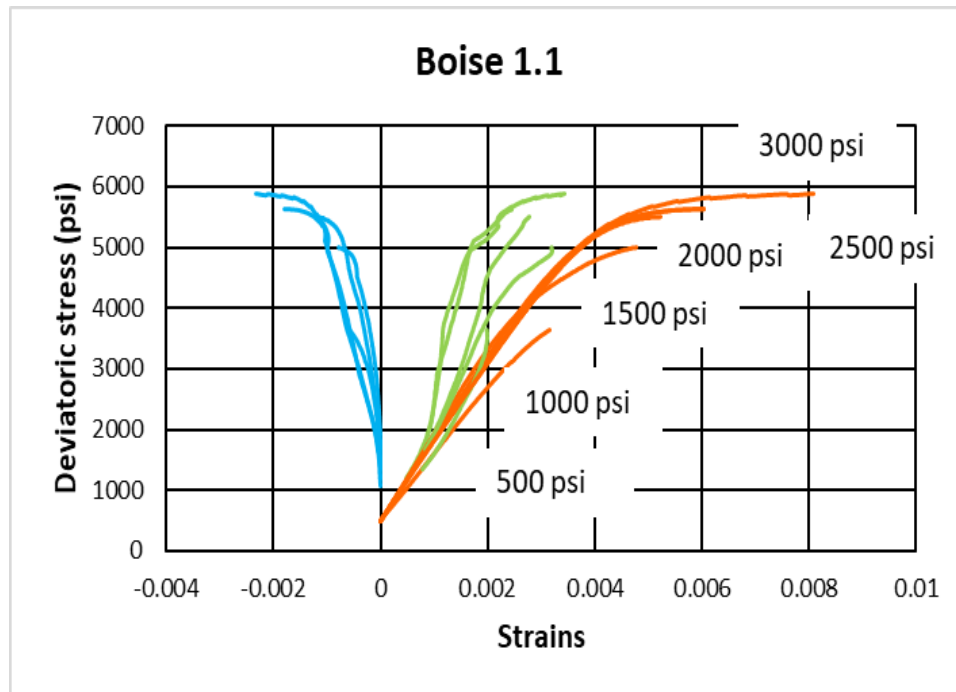


Figure 15: Fountain plot for Boise Sandstone showing deviatoric stress vs axial, radial and volumetric strain. The sample exhibited 45 percent irrecoverable strain.

The  $p/q$  plot for the Boise-1 Sandstone sample is shown in Figure 16. The maximum compressive strength was obtained by multiplying the deviatoric stress at the PPD by a factor of 1.2. The friction angle is 25.7 degrees, and the measured

cohesion is 1300 psi. The cohesion is similar to that observed for the Castlegate Sandstone, whereas the friction angle is similar to that observed for the Austin Chalk.

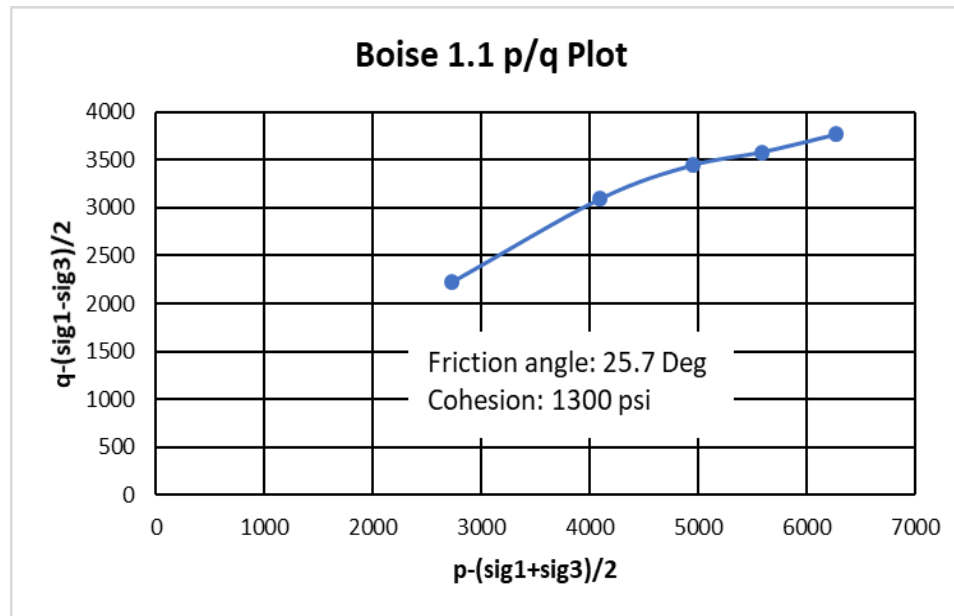


Figure 16: The p/q plot for Boise-1 Sandstone, the friction angle is 25.7 degrees and the measured cohesion is 1300 psi.

Figure 17 shows the fountain plot for the Boise-2 Sandstone sample. The test was run at confining pressures of 500, 1000, 1500, and 2000 psi. Similar to the Boise-1 Sandstone sample, the stiffness is fairly constant as a function of confining pressure. The sample also exhibits nonlinear behavior near the point of positive dilatancy, indicating a ductile response.

Table 5: Boise-2 Sandstone sample dimensions and weight.

| Parameter | Value    |
|-----------|----------|
| Length    | 2.007 in |
| Diameter  | 1.025 in |
| Weight    | 51.5 g   |

The p/q plot for the Boise-2 Sandstone sample is shown in Figure 18. The maximum compressive strength was obtained by multiplying the deviatoric stress at PPD by a factor of 1.2. The friction angle is 23 degrees, and the measured cohesion

is 1326 psi. Both cohesion and friction angle are similar to the Boise-1 Sandstone sample.

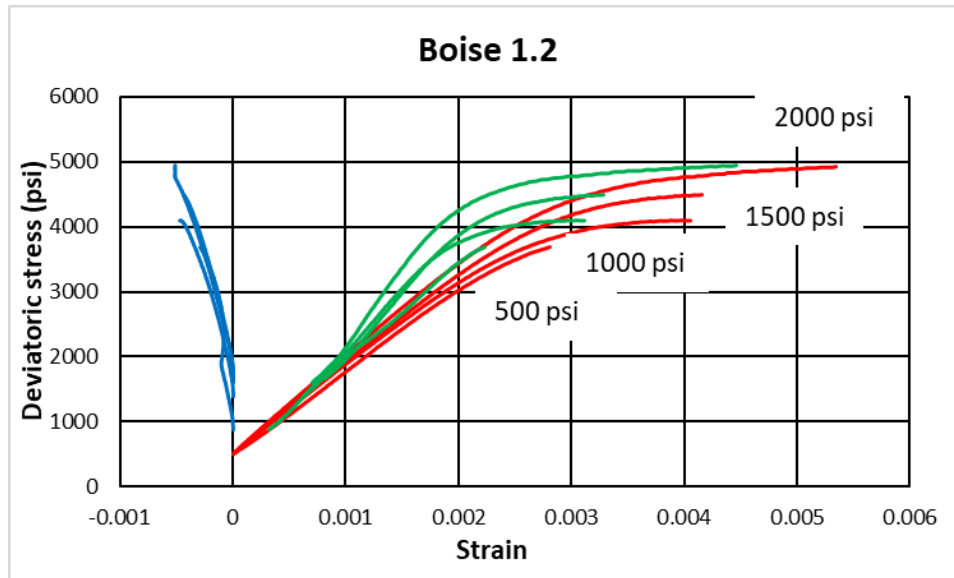


Figure 17: Fountain plot for the Boise Sandstone showing deviatoric stress vs axial, radial and volumetric strain. The sample exhibited 45 percent irrecoverable strain.

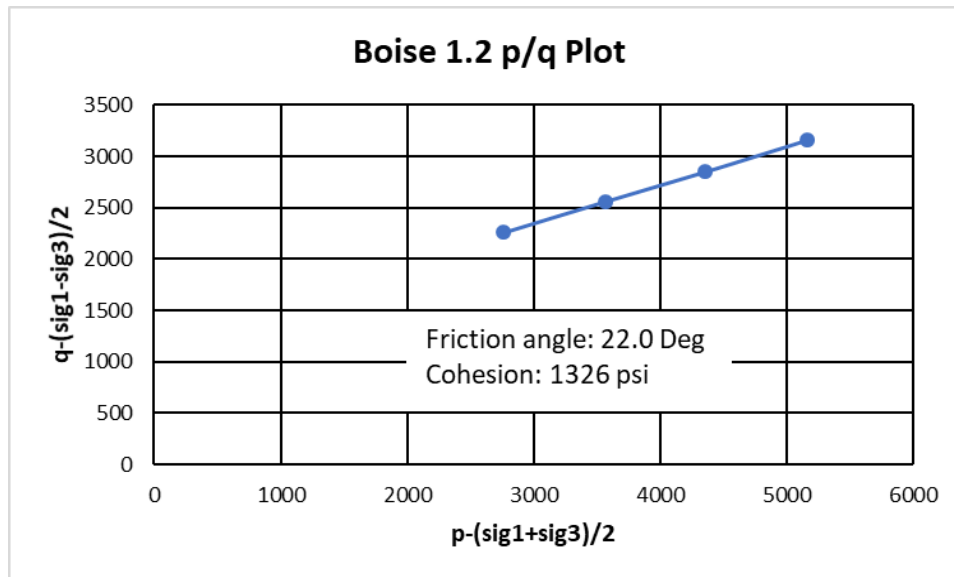


Figure 18: The p/q plot for Boise-2 Sandstone, the friction angle is 23.0 degrees and the measured cohesion is 1326 psi.

### 2.2.5 Fontainebleau Sandstone

Figure 19 and 21 are fountain plots for twin samples of the Fontainebleau Sandstone. The Fontainebleau Sandstone is a quartz cemented quartz arenite. Clay minerals are not present. The samples were obtained from a quarry in France. Similar to the Boise Sandstone tests, Fontainebleau Sandstone tests were also run to understand the effect of increasing confining pressure on induced damage to the sample. The sample in figure 19 was run to confining pressure of 2000 psi, and the sample in figure 21 was run to confining pressure of 2500 psi. These samples have a permeability of 500 mD. Figure 23 and figure 25 show another set of twin samples of the Fontainebleau Sandstone but with a different lithology. The permeability of these samples is 1 mD. The two sets of twin samples differ each other on the basis of permeability. These samples were also run to confining pressure of 2000 psi and 2500 psi, respectively. The purpose of running twin samples at two different confining pressures is to quantify the induced damage. These results are discussed later in the sample characterization chapter.

Figure 19 is the fountain plot for the Fontainebleau-1.9 Sandstone sample (lithology 1,  $k=500\text{mD}$ ). The sample exhibits linear behavior, resulting in elastic strains almost to the PPD. This is also evident from the observed irrecoverable strains, which are less than 5%. In a later section we will illustrate that the Fontainebleau Sandstone MST can be modeled with just linear and nonlinear elastic strains. Table 6 contains the sample dimensions and its weight.

Table 6: Fontainebleau-1.9 Sandstone sample dimensions and weight.

| Parameter | Value    |
|-----------|----------|
| Length    | 2.107 in |
| Diameter  | 1.007 in |
| Weight    | 64.31 g  |

Figure 20 shows the  $p/q$  plot for Fontainebleau-1.9 Sandstone sample. The friction

angle is 63.2 degrees, which is quite high. The cohesion is 300 psi. The maximum comprehensive strength was obtained by multiplying the deviatoric stress at PPD by a factor of 1.2.

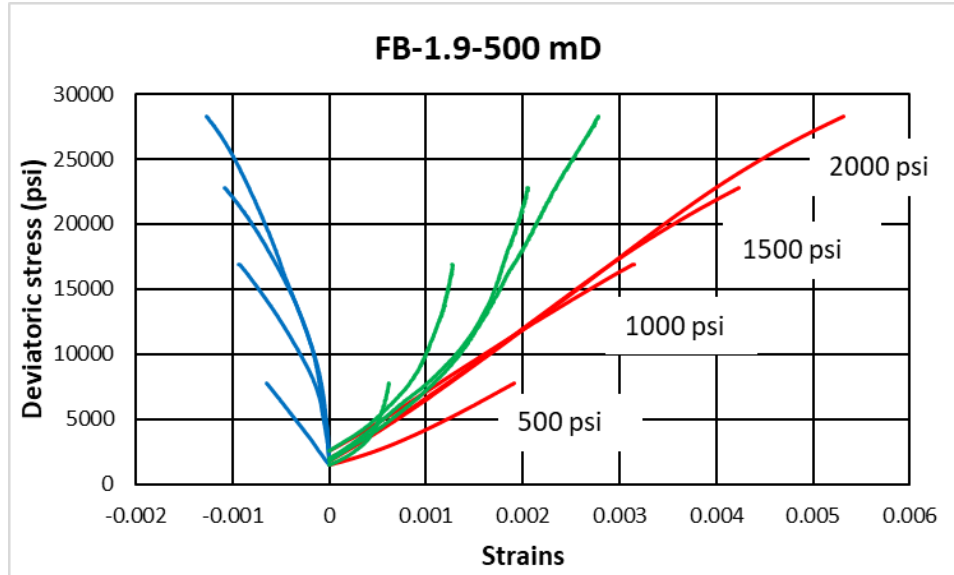


Figure 19: Fountain plot for Fontainebleau-1.9 Sandstone showing deviatoric stress vs. axial, radial and volumetric strain. The sample exhibited 5 percent irrecoverable strain.

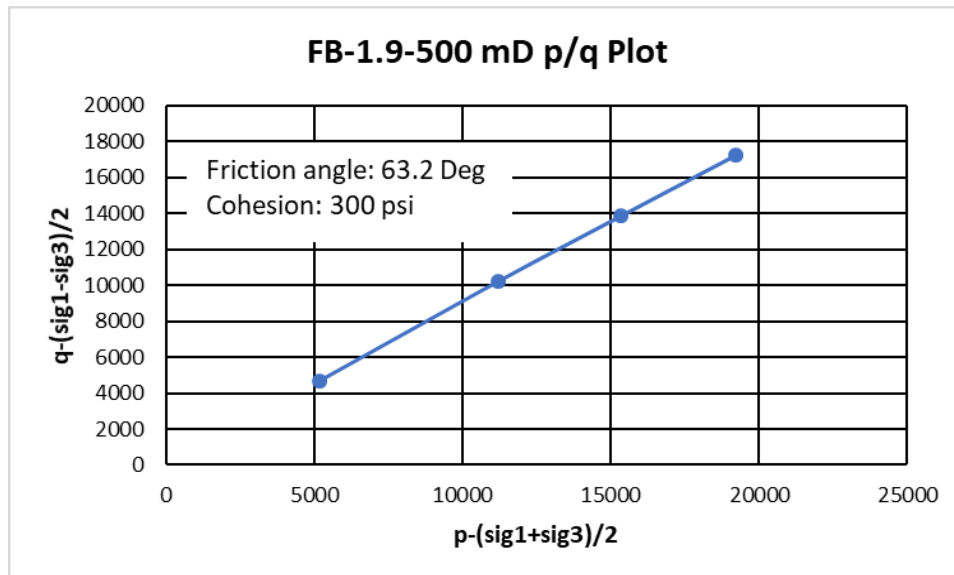


Figure 20: The p/q plot for Fontainebleau Sandstone, the friction angle is 63.2 degrees and the measured cohesion is 300 psi.

Figure 21 is the fountain plot for Fontainebleau-1.10 Sandstone sample. Similar to

Fontainebleau-1.9 Sandstone, the sample exhibits fairly linear behavior stress-strain behavior. This results in elastic strains almost to the PPD. Table 7 contains the sample dimensions and its weight.

Table 7: Fontainebleau-1.10 Sandstone sample dimensions and weight.

| Parameter | Value    |
|-----------|----------|
| Length    | 2.076 in |
| Diameter  | 1.011 in |
| Weight    | 62.45 g  |

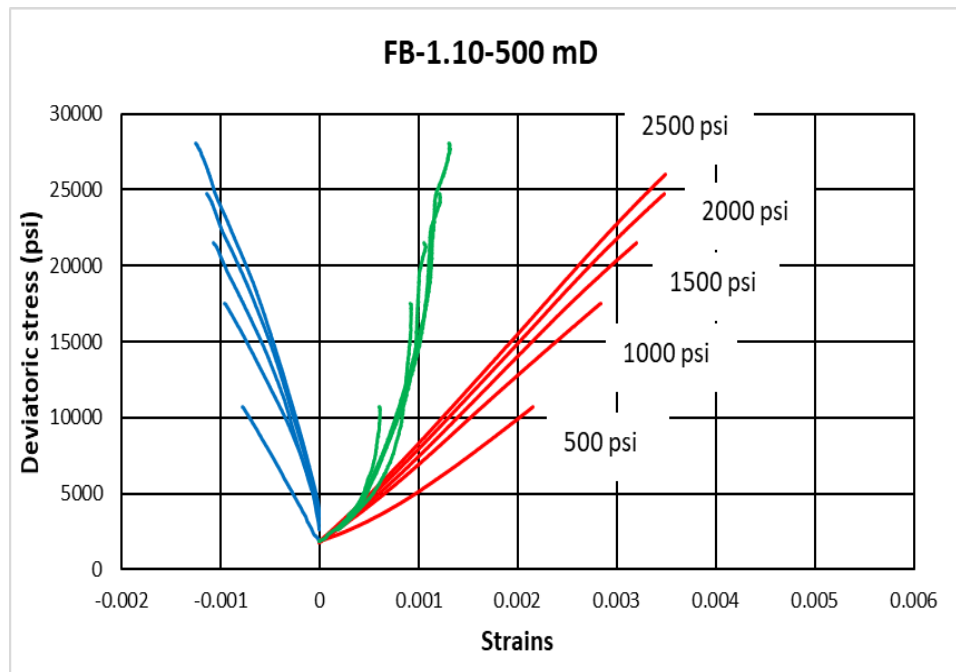


Figure 21: Fountain plot for the Fontainebleau Sandstone sample 1.10 showing deviatoric stress vs axial, radial and volumetric strain. The sample exhibited 5 percent irrecoverable strain.

Figure 22 is the p/q plot for the Fontainebleau-1.10 Sandstone sample. Similar to Fontaine-bleau 1.9, the friction angle (56 degrees) is quite high. However, the cohesion of 1500 psi is a bit higher than that of the twin sample.

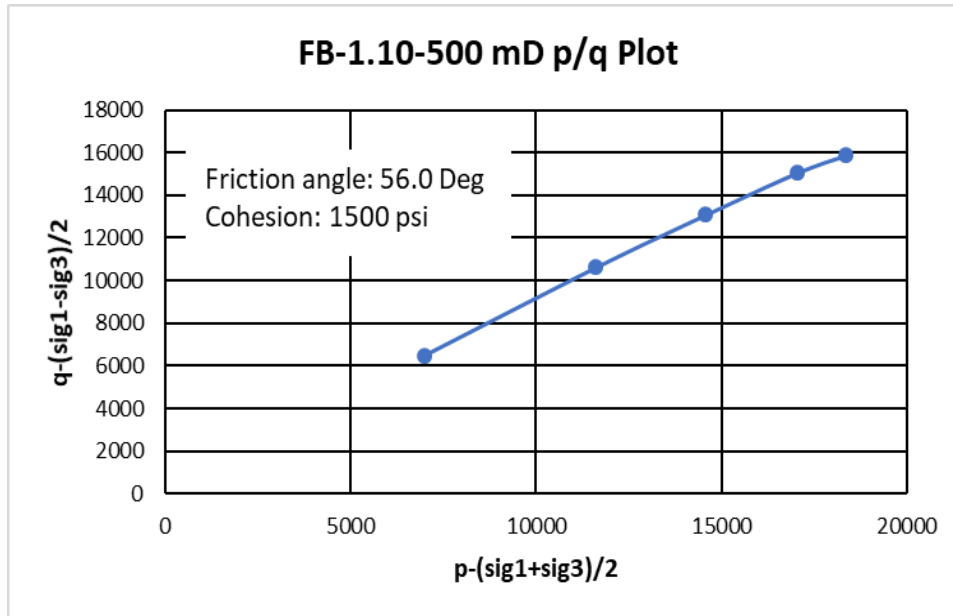


Figure 22: The p/q plot for Fontainebleau Sandstone, the friction angle is 56 degrees and the measured cohesion is 1500 psi.

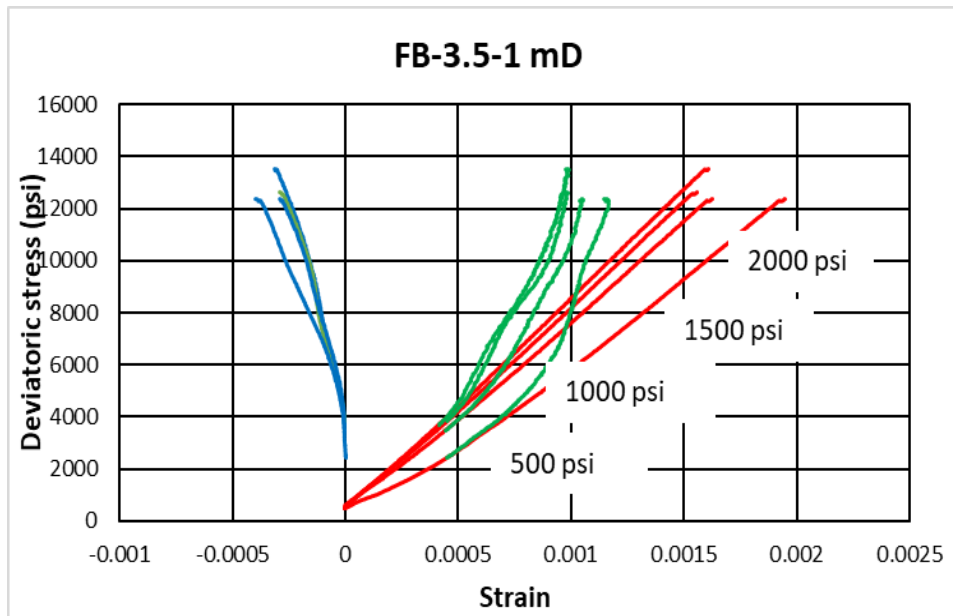


Figure 23: Fountain plot for Fontainebleau Sandstone showing deviatoric stress vs axial, radial and volumetric strain. The sample exhibited 5 percent irrecoverable strain.

Figure 23 is the fountain plot for the Fontainebleau-3.5 Sandstone sample. The permeability of this sample is 1 md. This is substantially lower than the permeability of the Fontainebleau Sandstone samples discussed previously. Similar to the higher

permeability Fontainebleau Sandstone samples, the behavior of the MST is quite linear. Table 8 contains the sample dimensions and weight.

Table 8: Fontainebleau-3.5 Sandstone sample dimensions and weight.

| Parameter | Value    |
|-----------|----------|
| Length    | 1.822 in |
| Diameter  | 0.986 in |
| Weight    | 52.4 g   |

Figure 24 is the p/q plot for Fontainebleau-3.5 Sandstone. The permeability is 1 mD. The friction angle (22 degrees) is quite low, but the cohesion of 4700 psi is quite high. The friction angle is the lowest of all the samples measured in this thesis, whereas cohesion is the highest.

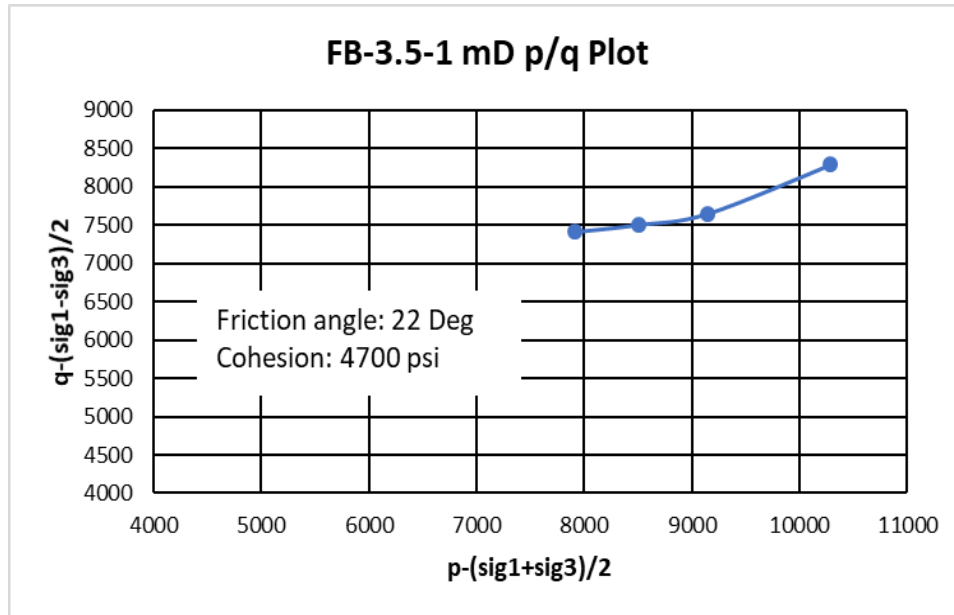


Figure 24: The p/q plot for Fontainebleau Sandstone, the friction angle is 22.0 degrees and the measured cohesion is 4700 psi.

Figure 25 shows the fountain plot for the Fontainebleau-3.4 Sandstone sample. The test was run at confining pressures of 500, 1000, 1500, 2000 and 2500 psi. This sample also exhibited linear behavior. Table 9 contains the sample dimensions and weight.

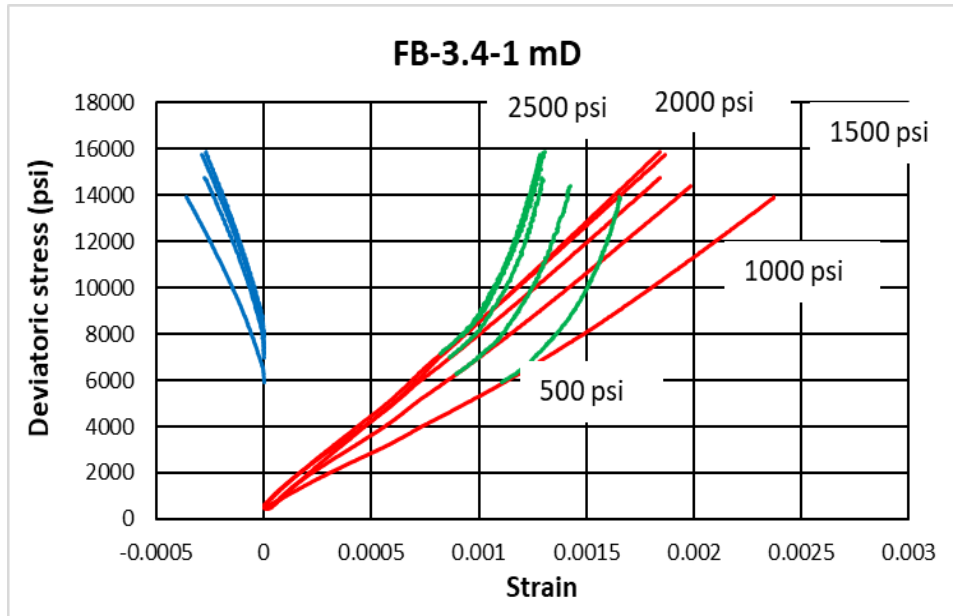


Figure 25: Fountain plot for Fontainebleau Sandstone showing deviatoric stress vs. axial, radial, and volumetric strain. The sample exhibited 5 percent irrecoverable strain

Figure 26 shows the p/q plot of Fontainebleau-3.4 Sandstone. The friction angle is 24.3, and the cohesion is 5200 psi. Both friction angle and cohesion are similar to the twin sample, Fontainebleau-3.5 Sandstone.

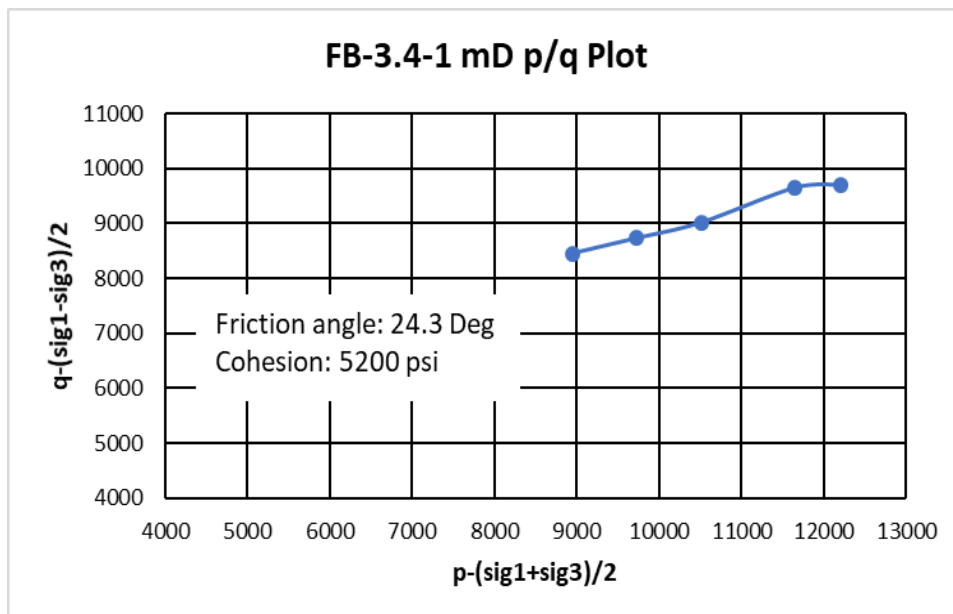


Figure 26: The p/q plot for Fontainebleau Sandstone, the friction angle is 24.3 degrees, and the measured cohesion is 5200 psi.

Table 9: Fontainebleau-3.4 Sandstone sample dimensions and weight.

| <b>Parameter</b> | <b>Value</b> |
|------------------|--------------|
| Length           | 1.795 in     |
| Diameter         | 0.990 in     |
| Weight           | 52.50 g      |

### 2.2.6 Miocene sandstone

For the Miocene-1 sandstone sample, the sample failed after only three confining pressures cycles, as shown in Figure 27. This result illustrates that unloading at a strain ratio of 0.5 is not a suitable point for a weakly cemented, under-compacted sandstone. The Miocene-3 sandstone sample was run with an unloading parameter at a strain ratio of 0.3 for each confining cycle, as shown in Figure 32. The measured irrecoverable strain is approximately 7%. For the Miocene-1 sandstone sample, the measured irrecoverable strain is approximately 43%. The difference results from the Miocene-3 sandstone being loaded to lower deviatoric stress, as the strain ratio to unload was just 0.3. Lower deviatoric stress resulted in less induced damage and hence, lower irrecoverable strains.

The Miocene-1 sandstone exhibits nonlinearity near the point of positive dilatancy. This is consistent with the ductile nature of the sample. This has also resulted in higher irrecoverable strains of 43%. Table 10 contains the sample measurements.

Table 10: Miocene-1 sandstone sample dimensions and weight.

| <b>Parameter</b> | <b>Value</b> |
|------------------|--------------|
| Length           | 1.948 in     |
| Diameter         | 0.972 in     |
| Weight           | 43.21 g      |

Figure 28 is the p/q plot for the Miocene-1 sandstone sample. The friction angle of 39.2 degrees is quite high, but the cohesion of 920 psi is on the lower end of the observations in this study.

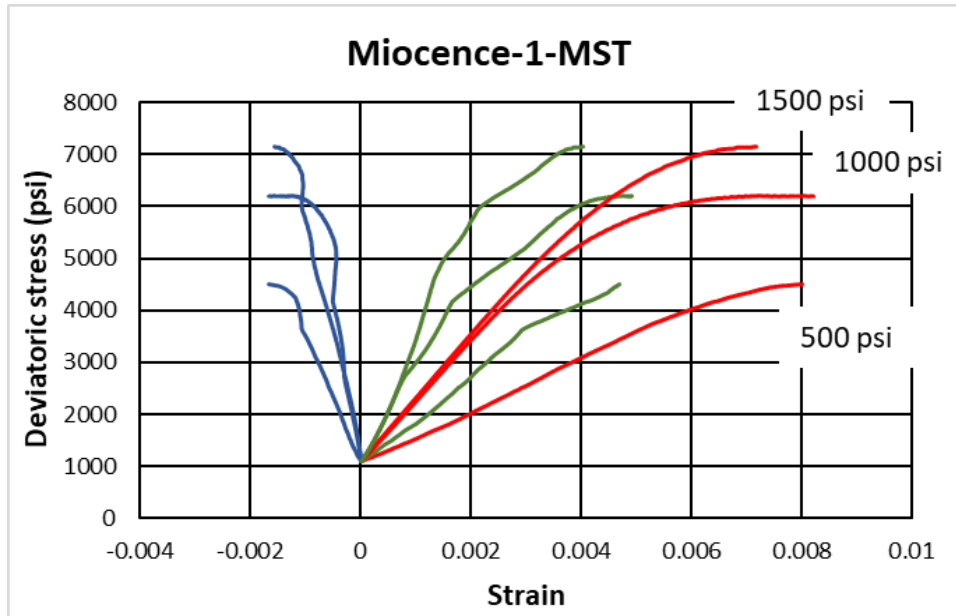


Figure 27: Fountain plot for a Miocene sandstone sample showing deviatoric stress vs. axial, radial, and volumetric strain. The sample exhibited 43 percent irrecoverable strain.

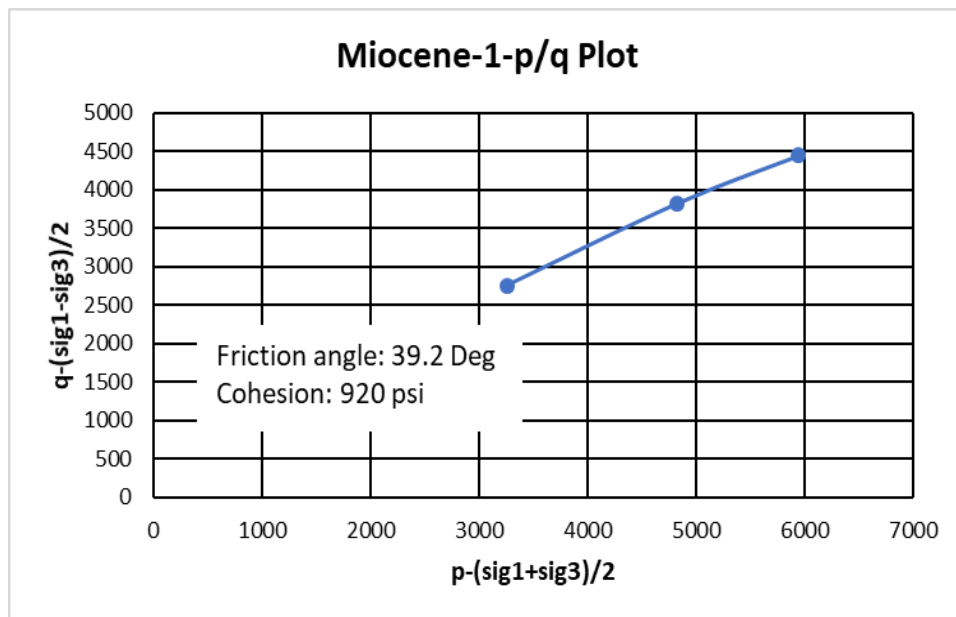


Figure 28: The p/q plot for Miocene-1 sandstone sandstone, the friction angle is 39.2 degrees, and the measured cohesion is 920 psi.

The Miocene-3 sandstone sample was not unloaded at the point of positive dilatancy (strain ratio: 0.5). Instead, the sample was unloaded at a strain ratio of 0.3.

This change in the testing protocol resulted from the observation that the Miocene-1 sandstone sample failed after only two cycles when it was unloaded at the strain ratio of 0.5. Because the Miocene-3 sandstone sample was loaded to a lower strain ratio, less damage was induced during each stage. Figure 29 shows the fountain plot for the Miocene-3 sandstone sample. The sample exhibits linear behavior. This indicates less sample damage and more elastic strains. Table 11 contains the sample dimensions and weight.

Table 11: Miocene-3 sandstone sample dimensions and weight.

| Parameter | Value    |
|-----------|----------|
| Length    | 2.004 in |
| Diameter  | 0.971 in |
| Weight    | 43.79 g  |

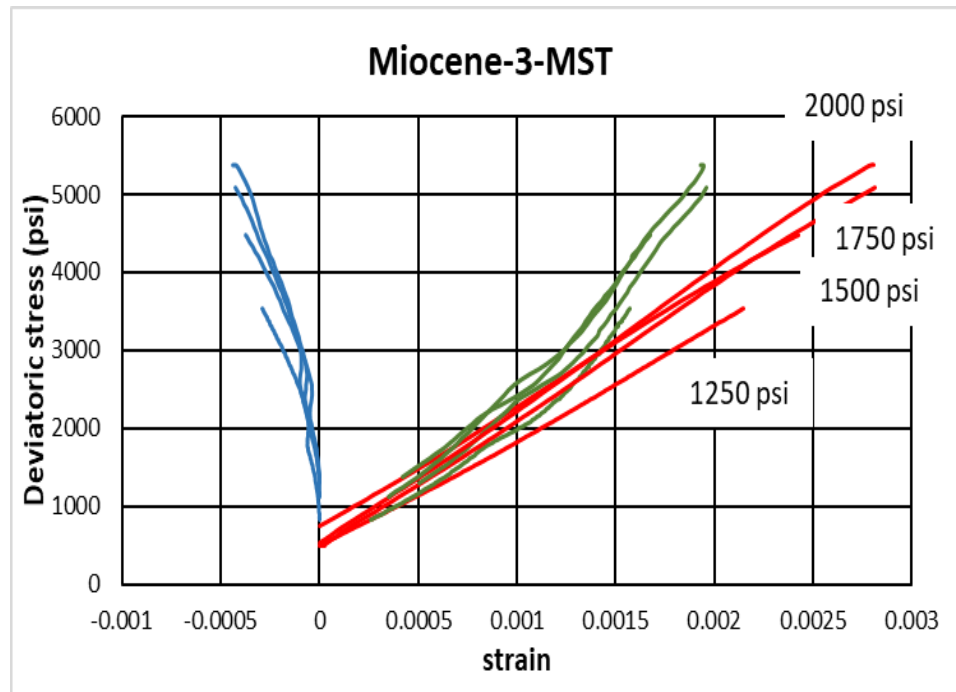


Figure 29: Fountain plot for the Miocene sandstone showing deviatoric stress vs. axial, radial, and volumetric strain. The sample exhibited a 6 percent irrecoverable strain because the stopping point for each stage was reduced to a strain ratio of 0.3.

Figure 28 shows the p/q plot for the Miocene-3 sandstone sample. The friction

angle of 30.6 degrees is a little high, but the cohesion of 160 psi is quite low.

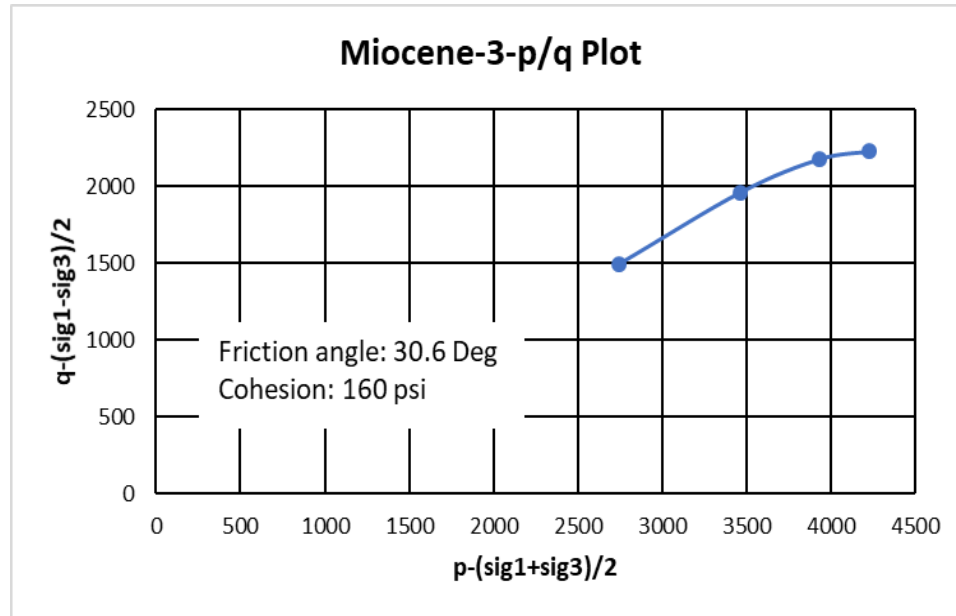


Figure 30: The p/q plot for Miocene-3 sandstone, the friction angle is 30.6 degrees, and the measured cohesion is 160 psi.

## 2.3 Experimental Data Modeling and Analysis

In the previous section, we have discussed how the experimental data was taken. In this and subsequent sections, we will discuss how to analyze the data and fit a model to it. We separate the sample response into linear elastic strains, nonlinear elastic strains, and irrecoverable strains. We will now discuss in detail how to model each of these strains separately and how to understand the physical mechanisms that control each part of the data. Please note that only axial strains have been modeled. The radial strains will be part of future work.

### 2.3.1 Quadratic Fit for the Stress vs Strain Curve

In order to develop a model for the stress strain behavior, we expand the axial stress in terms of the axial strain for the unload and reload curves in a Taylor series. We have only fit the data up to a second order term. The rest of the data is analyzed

separately as induced plastic strains. The axial stress can be expanded in term of strains as

$$\sigma = M_2\epsilon^2 + M_1\epsilon + \sigma_0. \quad (13)$$

Where  $\sigma_0$  is the initial stress of either the unloading or reloading curve.  $M_1$  and  $M_2$  are the regression coefficients for the fit.

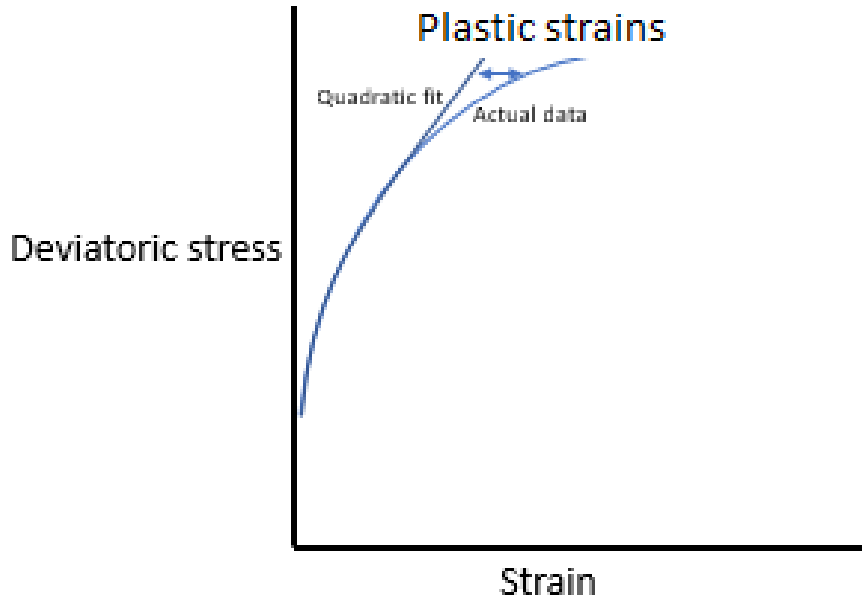


Figure 31: An example of a deviatoric stress vs. strain curve showing the actual data and the quadratic fit to the data. Induced plastic strains are calculated by taking the difference between actual data and the quadratic fit.

In order to fit the data, we are not using the initial two percent of the reloading cycles. This portion of the curve is dominated by equipment hysteresis, and possible effects due to sample creep on the unload cycle. On the reloading curve, the data is limited to avoid the initial loading curve. In other words we use only that portion of the curve for which additional sample damage is induced. The curve is fit to the maximum point of curvature. The maximum curvature point is calculated by fitting a circle through three points along the curve and calculating its radius. The point of the curve with the smallest radius is the maximum point of curvature.

### 2.3.2 Interpretation of $M_1$ Velocity

In the limit of small strains, the quadratic term ( $M_2\epsilon^2$ ) may be ignored, and the equation reduces to a Hooke's law relationship. The fit to the stress-strain data, therefore, should give  $M_1$  equal to the modulus derived from the velocity data, as shown in Figure 32.

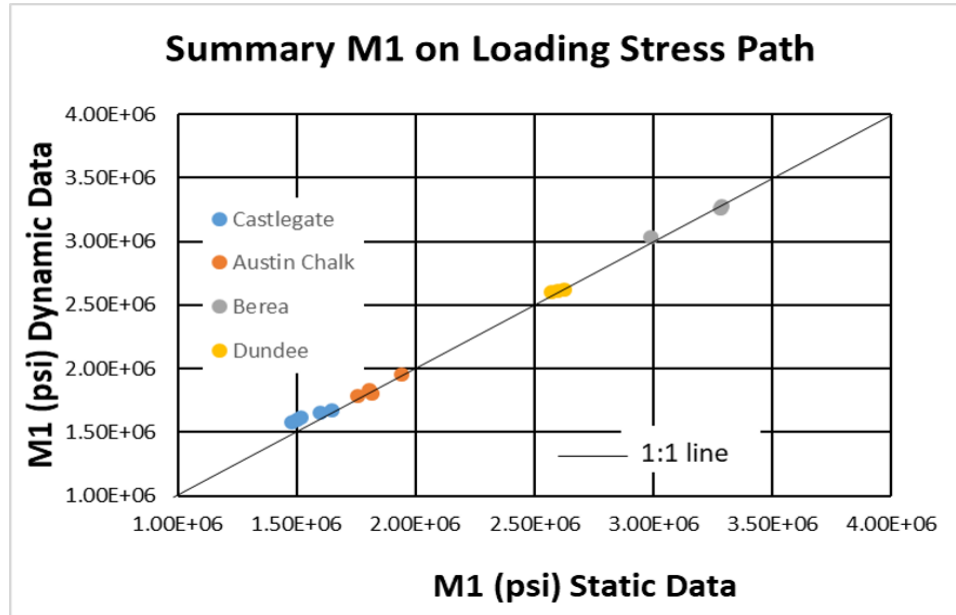


Figure 32: Dynamic vs. static  $M_1$  on the loading stress path. The static and dynamic properties are equal within experimental error. There are multiple points for each sample implying a small stress dependence for each sample compared to the differences between samples.

For the static and dynamic data, the measured small strain moduli are equal to within the uncertainty of the measured values, i.e.,  $M_1$  can be directly predicted for static data if we have acoustic data available from some other source. This is consistent with earlier published results (Fjaer et-al, 2015). If, however, the bulk and shear moduli are calculated from the static data to compare to the dynamic data, they are not equal at small strains. We conclude that we cannot convert between stress paths for static data using a linear elastic model. We also found that  $M_1$  either varies or remains constant as a function of confining pressure, depending upon

the sample, as shown in fig 33. This difference is currently under investigation.

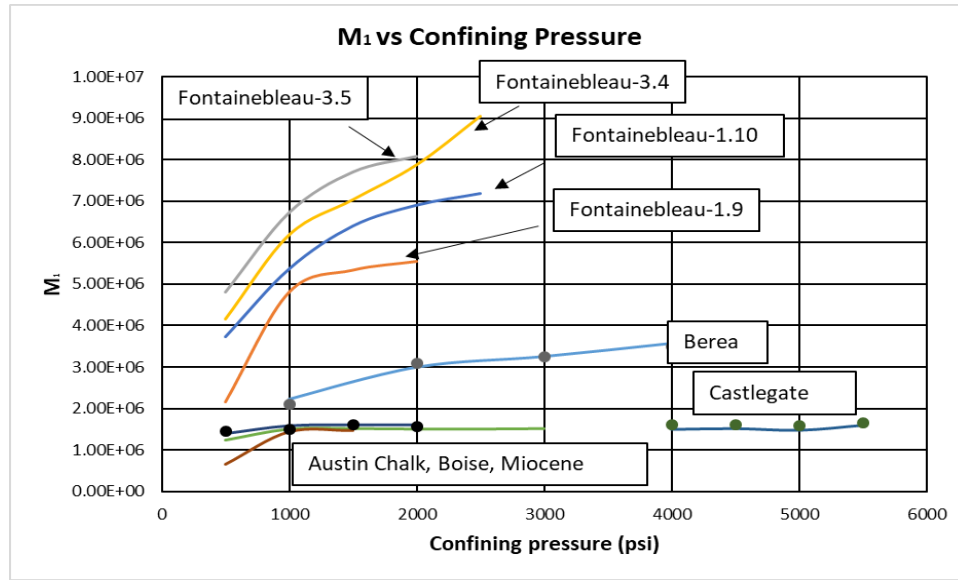


Figure 33:  $M_1$  vs. confining pressure.  $M_1$  varies significantly with confining pressure for Fontainebleau samples and Berea. However, it remains relatively constant for Austin Chalk, Boise Sandstone, and Miocene sandstone samples. The result is currently under investigation. The dots are dynamic  $M_1$ , where velocity data is available.

### 2.3.3 Interpretation of $M_2$ – Irrecoverable Strain

$M_2$  is termed the “Hypermodulus,” the coefficient of the second order term in Eq 13. This term is related to nonlinear irrecoverable strain effects. There was no significant variation observed among  $M_2$  for different reloads as a function of confining pressure. Therefore, an average value of  $M_2$  was used for each sample. In section 1.6.1, we discussed that irrecoverable strains remained constant for different reloads. This is consistent with  $M_2$  also remaining constant for each reload. Figure 34 shows a plot of the hypermodulus as a function of irrecoverable strains for each of the different samples. The hypermodulus has a direct relationship with irrecoverable strain. The relationship can be fit with either a linear or a quadratic relationship. We need more data, at higher irrecoverable strains, to establish which of these relationships best fits a range of sample types. For higher irrecoverable strains, the absolute value of  $M_2$  is

higher. The higher  $M_2$  value implies more nonlinear strain effects.

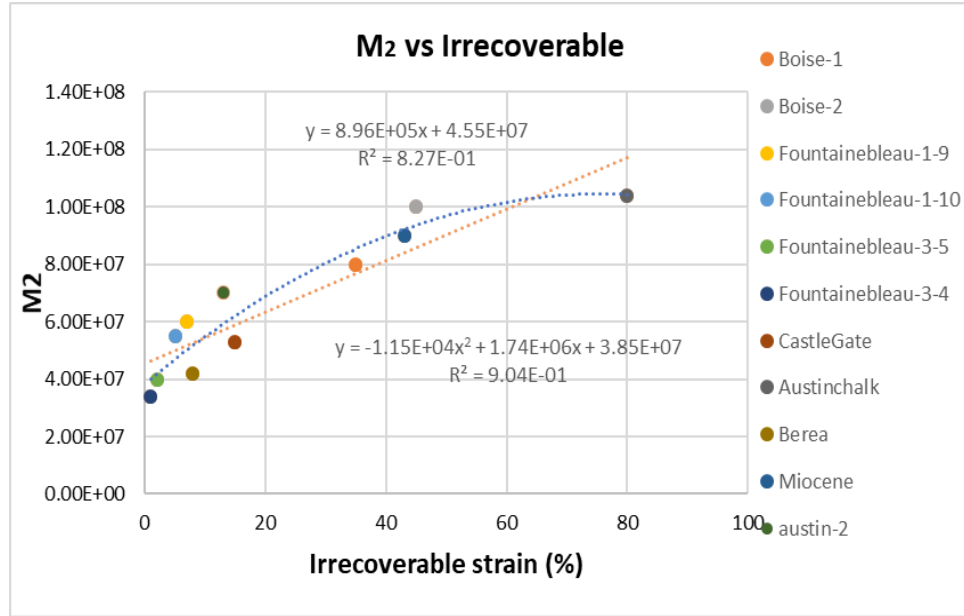


Figure 34: Absolute  $M_2$  vs irrecoverable strains.  $M_2$  has a direct relationship with irrecoverable strain. For higher irrecoverable strain, the value of  $M_2$  is higher. The higher  $M_2$  value implies more non-linear strain effects.

### 2.3.4 $M_1$ and $M_2$ on an Unloading Stress Path

$M_1$  and  $M_2$  were also calculated for unloading cycles. The results were compared with the parameters from the loading cycle. On average both  $M_1$  and  $M_2$  were higher on unloading cycle. The reason is primarily due to hysteresis effects that occur during sample loading and unloading. The differences in  $M_1$  ranged from 10% in higher irrecoverable strain samples (Castlegate Sandstone, Austin Chalk, Boise Sandstone, and Miocene sandstone) to almost 20% in lower irrecoverable strains samples (Fontainebleau Sandstone, Berea Sandstone). The differences in  $M_2$  for the latter group of samples, ranged from 10% to nearly an order of magnitude.

Total hysteresis in higher irrecoverable strain samples is larger than that observed in samples exhibiting lower irrecoverable strains. However, the difference in parameters among the high hysteresis samples is lower. This is counter intuitive. In higher irrecoverable strain samples, the hysteresis effects are dominated by plastic strains.

There are fewer effects on elastic parameters ( $M_1$  and  $M_2$ ). For lower irrecoverable strain samples, there are negligible plastic strains. Almost all the hysteresis effects the linear ( $M_1$ ) and non-linear ( $M_2$ ) elastic parameters. That is why we have observed larger differences in lower irrecoverable strain samples than in higher irrecoverable strain samples. Because our purpose is to predict the loading curve, subsequent analyses are performed on the loading stress path only.

### 2.3.5 Compaction Model

Myers and Hathon (2014) developed a model to predict uniaxial pore volume compressibility for unconsolidated to slightly consolidated sands in the deep water Gulf of Mexico. The model describes the evolution of a network as a function of modifying the number of nodes (compacting sites) and the number of bonds (grain contacts) between them. This network model is quite general and may be applied to a variety of physical phenomena such as permeability, and resistivity. The model has been extended here to include triaxial data.

### 2.3.6 Mathematical Representation

The goal of this section is to develop the network model equations that describe how the statistics of a network evolve with a characteristic change in the network properties. An initial distribution of the number of nodes to the number of bonds is known, as shown in figure 1. The network grows by adding nodes to it, which alter the network statistics. The objective is to develop a mathematical model for how the statistics of the entire network evolve.

We start with some definitions and notation. For the initial network,  $n = n(N, j)$  is the initial number of nodes,  $n$ , with  $j$  bonds when there are  $N$  total nodes. The total number of nodes is now increased, and the new network statistics are described by  $n' = n(N + \delta N, j)$  where  $n'$  is the new number of nodes with  $j$  bonds resulting

from the addition of  $\delta N$  total nodes. The changes in  $n$  and  $N$  are given by

$$\delta n(N, j) = n'(N, j) - n(N, j) \quad (14)$$

and

$$\delta N = N' - N = \sum n'(N, j) - \sum n(N, j). \quad (15)$$

As a base case we make the following “self-similar” assumption for the growth of the network,

$$\frac{\delta n(N, j)}{n(N, j)} = \frac{\delta N}{N}. \quad (16)$$

$n(N, j)$ : The initial number of nodes,  $n$ , with  $j$  bonds when there are  $N$  total nodes. The total number of nodes is now increased by  $\delta N$  and the new network statistics are described by where  $n(N + \delta N, j)$  is the new number of nodes with  $j$  bonds resulting from the addition of  $\delta N$  nodes,

$$n(N + \delta N, j) = n(N, j) + \frac{\delta N}{N} n(N, j). \quad (17)$$

The change in the number of nodes with  $j$  bonds is proportional to the fractional change in the total number of nodes that are added to the network, as shown in Figure 36. With this assumption, the statistics of the original network are preserved, and the network exhibits self- similar behavior. We show this by examining the limit as  $\delta N$  approaches zero,

$$\frac{n(N + \delta N, j)}{\delta N} = \frac{n(N, j)}{N}. \quad (18)$$

This gives in the limit of small  $\delta N$ ,

$$\frac{\partial n}{\partial N} = \frac{n}{N} \quad (19)$$

The distribution of the initial network provides the boundary condition. This will be the reference curve as

$$n(N_o, j) = D(j). \tag{20}$$

$N_o$  is the initial number of nodes. The solution is given by

$$n(N, j) = \eta D(j), \text{ Where : } \eta = \frac{N}{N_o}. \tag{21}$$

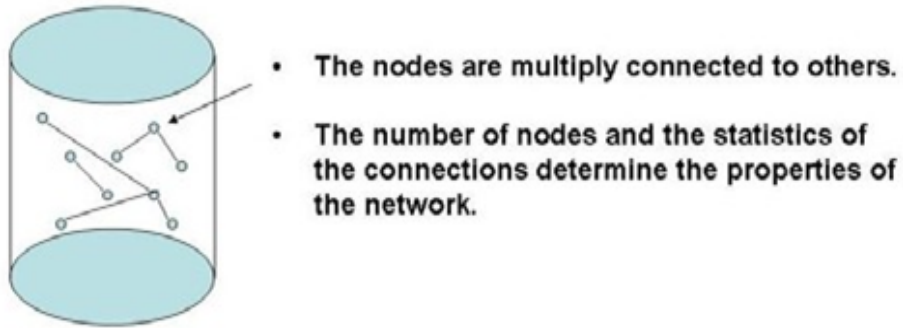


Figure 35: The initial known network consists of nodes with multiple connections to one another. The statistics of the network are described by  $n(N,j)$  the number of nodes with  $j$  connections when there are  $N$  total nodes in the network.

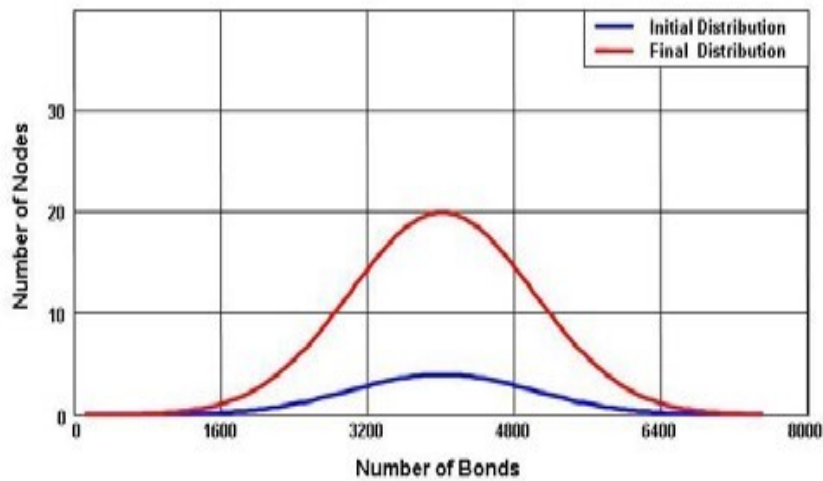


Figure 36: Solution to a model where it is assumed that the fractional change in the number of nodes is proportional to the fractional change in the total number of nodes

The next step is to extend the model that includes the possibility of more than the simple scaling by adding extra terms. These added terms account for the deviation from the base case and are a measure of deviation from self-similar behavior. A factor  $k(n,j)$  is used to define the fraction of nodes that add an additional bond above self-similar scaling. When  $k(n,j)$  is equal to zero, our base case is recovered. The model may be represented by

$$N * \frac{\partial n(N, j)}{\partial N} + k(n, j) * \frac{\partial n(N, j)}{\partial j} = n(N, j) * \left(1 - \frac{\partial k(n, j)}{\partial j}\right). \quad (22)$$

$k(n,j)$  is the fraction of nodes that will add an “excess” bond relative to self-similar scaling of the initial distribution. It may, in general, be a function of both the number of nodes,  $n$ , with a given number of bonds and/or the number of bonds,  $j$ , a node already has. The initial distribution translates, broadens, and skews. This results from the  $j$  dependence on the specific form of  $k(n,j)$ . The equation is nonlinear if  $k$  depends on  $n$ , and represents simple bookkeeping of nodes and bonds. The physics inherent in the evolving network is all contained in the term  $k(n,j)$ . It is based on the physics the network represents, as shown in figure 37.

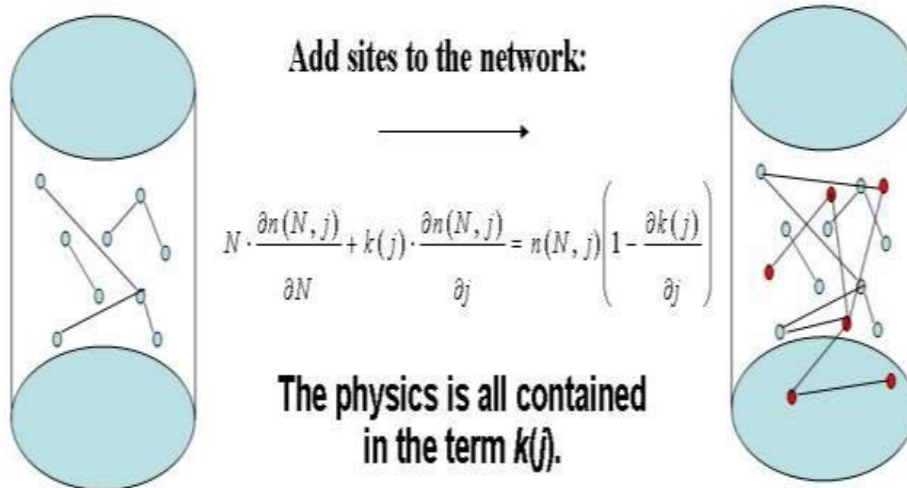


Figure 37: Depending on the form that the  $k(n,j)$  term takes, the equation allows for models where the distribution translates, broadens, skews and shows nonlinear effects with increasing numbers of nodes.

For  $k = k_o$ , we get

$$N * \frac{\partial n(N, j)}{\partial N} + k_o * \frac{\partial n(N, j)}{\partial j} = n(N, j). \quad (23)$$

The boundary condition is the assumption of a reference distribution  $n(N_o, j) = D(N_o, j)$ , where  $N_o$  is the initial number of nodes. The following solution is obtained. Using the method of characteristics, we arrive at

$$n(N, j) = \eta D(j - k_o * \ln(\eta)). \quad (24)$$

The scaling parameter for the network changes,  $\eta = \frac{N}{N_o}$  for nonzero  $k_o$  (for  $k_o = 0$  we retrieve the base case).

We now present the solution of the nonlinear assumptions for  $k$ ;  $k$  now depends on  $n$ , the number of nodes with a particular number of bonds. Substituting  $k(n, j) = k(n) = k_o + k_1.n$  we arrive at

$$N * \frac{\partial n(N, j)}{\partial N} + (k_o + k_1 n) * \frac{\partial n(N, j)}{\partial j} = n(N, j). \quad (25)$$

As before, we start with the boundary condition

$$n(N, j) = D(N_o, j), \quad (26)$$

when

$$N = N_o, \quad (27)$$

which gives the implicit solution ( $n$  appears on both sides of the equation),

$$n(N, j) = \eta D(j - (k_o + 2k_1 n) * \ln(\eta)). \quad (28)$$

We have calibrated the linear case of the model to the triaxial data. The future work will involve to calibrate the non-linear case.

### 2.3.7 Model Calibration

The model takes the form of a partial differential equation, which describes the evolution of a network as a function of a physical change, such as applying stress. The solution of this boundary value problem requires a measurement which establishes the boundary condition for the solution. The model is used to predict the plastic strains in terms of the invariants, the deviatoric, and mean stresses. The plastic strains were calculated by taking the difference between the original data and the quadratic fit to the elastic data, as shown in figure 38 below.

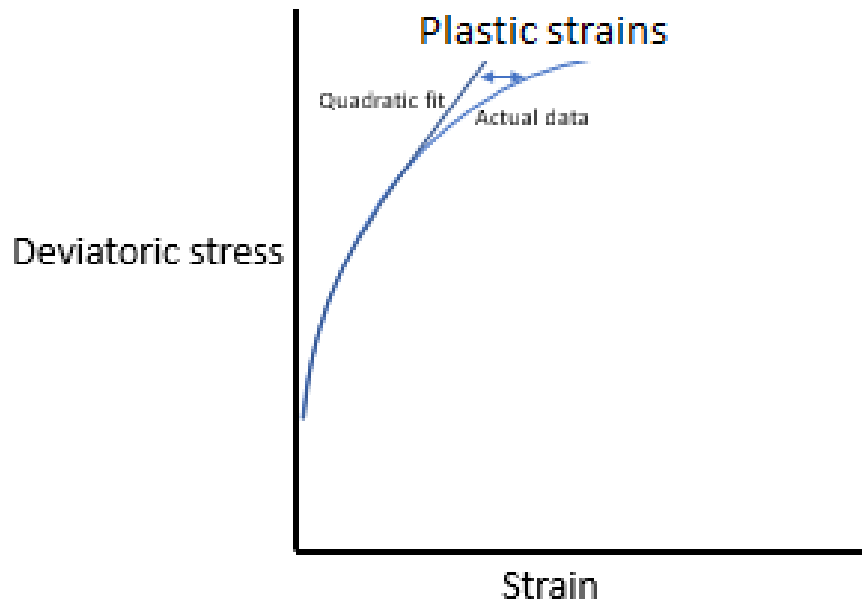


Figure 38: An example of a deviatoric stress vs. strain curve showing the actual data and the quadratic fit to the data. Induced plastic strains are calculated by taking the difference between actual data and the quadratic fit.

The first order term in the linear model is given by Eq. 29 where  $k = k_o$  is a constant,

$$\epsilon_m^p(N, \sigma) = \eta(\sigma - k_0 \ln \eta). \quad (29)$$

The linear solution of the network model is applied to the data. The future work will involve using the non-linear solution to fit the data. The boundary condition for the solution of the partial differential equation is assumed to be an exponential distribution ( $n(N_o, \sigma) = D(N_o, \sigma) = e^{\lambda\sigma}$ , consistent with AE observations (Prakash 2018). where  $n$  is number of nodes with specific number of bonds and  $N$  is total number of nodes. We have mapped  $n$  into plastic strains induced as a function of applied stress. From the exponential fit of the base case, we can get  $N_o$  and  $\lambda$ .  $N_o$  is the initial total strain.  $\lambda$  is the characteristic stress slope.  $K_o$  controls how the exponential distribution translates with mean and deviatoric stress.  $\eta = \frac{N}{N_o}$  is the measure of total strain and is a function of both mean and deviatoric stress.  $n(N, \sigma)$  is the calculated strain at a certain  $\sigma$  (stress). For an exponential distribution, equation 29 can be written as

$$\epsilon_m^p(\bar{\sigma}) = \eta_o e^{1/\bar{k}(\bar{\sigma} - \bar{\sigma}^o)}. \quad (30)$$

We can define  $\bar{\sigma}$  and  $\bar{k}_o$  in term of mean and deviatoric stress as

$$\sigma_d = \bar{\sigma} \sin \theta, \sigma_m = \bar{\sigma} \cos \theta, k_d = \bar{k} \sin \theta, k_m = \bar{k} \cos \theta. \quad (31)$$

$\theta$  describes the stress path. For example, for  $\theta = 0$  is constant mean stress.  $\theta = 1$  is constant deviatoric stress. Substituting above equation in equation 30 gives

$$\epsilon_m^p(\sigma) = \eta_o e^{1/k_d(\sigma_d - \sigma_d^o)} * e^{1/k_m(\sigma_m - \sigma_m^o)}. \quad (32)$$

Equation 32 allows for the possibility of calculating plastic strains as a function of the mean and deviatoric stresses. We need to know the base case ( $\eta_o$ ), ( $k_m$ ) and

( $k_d$ ). We are assuming that the effects of mean and deviatoric stress are separable.

### 2.3.8 Experimental Fit for Plastic Strains

In this section, we have plotted the modeled and raw data together to validate the model. Figure 39 is the plot of plastic strains as a function of deviatoric stress at different confining pressures for Castlegate Sandstone. The data shows an exponential function trend. The parameters fit to the model were ( $\eta_o$ ) 1.06E-4, ( $k_d$ ) 513 psi and ( $k_m$ ) -633 psi. The value of  $k_d$  is positive whereas  $k_m$  is negative. This is consistent with the intuitive effects of deviatoric and mean stresses. Deviatoric stress tends to weaken the sample and hence increases plastic strains. However, the mean stress tends to strengthen the sample resulting in decreasing plastic strains. This shows that the, the model captures the effects of changing mean and deviatoric stress correctly.

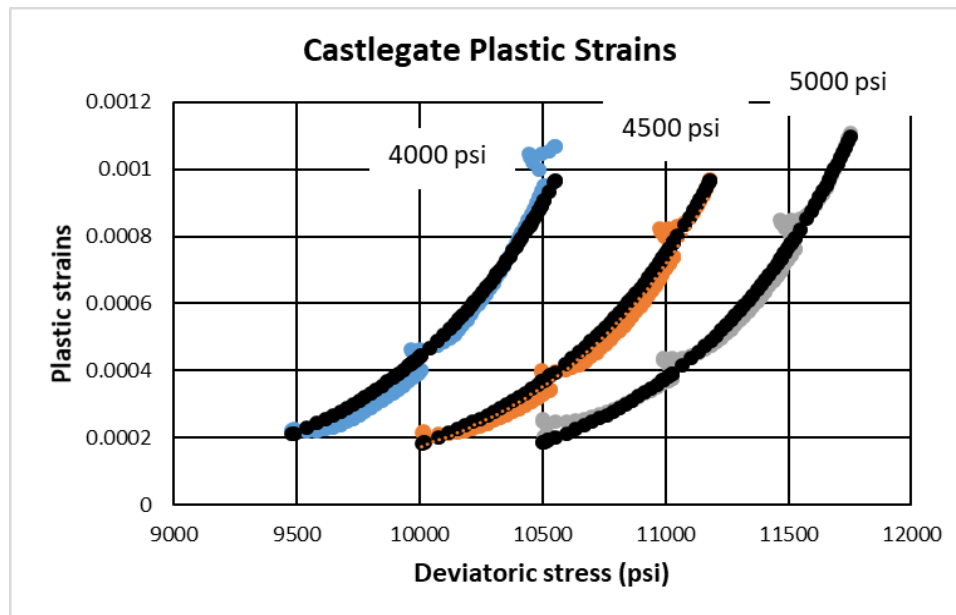


Figure 39: Plastic strains as a function of deviatoric stress for Castlegate Sandstone. The solid black lines are model predictions. A simple exponential is used to fit the data. The model is fit using only three parameters: ( $\eta_o$ ) 1.06E-4, ( $k_d$ ) 513 psi and ( $k_m$ ) -633 psi.

Figure 40 is a plot of original plastic strains vs modeled plastic strains for the Austin Chalk. The parameters used to fit the model are  $\eta_o$  3.11E-3,  $k_d$  606 psi and  $k_m$

-943 psi. Figure 41 is a similar plot for the Boise-1 Sandstone sample with modeling parameters  $\eta_o$  5.05E-4,  $k_d$  115 psi and  $k_m$  -505 psi. Figure 42 shows the plot for the Boise-2 Sandstone sample with modeling parameters  $\eta_o$  2.15E-4,  $k_d$  114 psi and  $k_m$  -200 psi. For the Fontainebleau and Berea Sandstones, there is no need to model plastic strains because the quadratic fit is enough to model all the data. Both of these formations have irrecoverable strains less than approximately 5%. Such low irrecoverable strains suggest elastic behavior. Figure 43 is the comparison of modeled plastic strains vs original data. The parameters used to model the data are ( $\eta_o$ ) 4.69E-5, ( $k_d$ ) 240 psi and ( $k_m$ ) -195 psi.

For Fontainebleau Sandstone and Berea Sandstone, the irrecoverable strain is less than 7%. Therefore the linear and non-linear elastic parameters ( $M_1$  and  $M_2$ ) are enough to model the data. We have plotted the model fit later in section 2.4. For this reason there is no need to model plastic strains for either the Fontainebleau Sandstone or the Berea Sandstone.

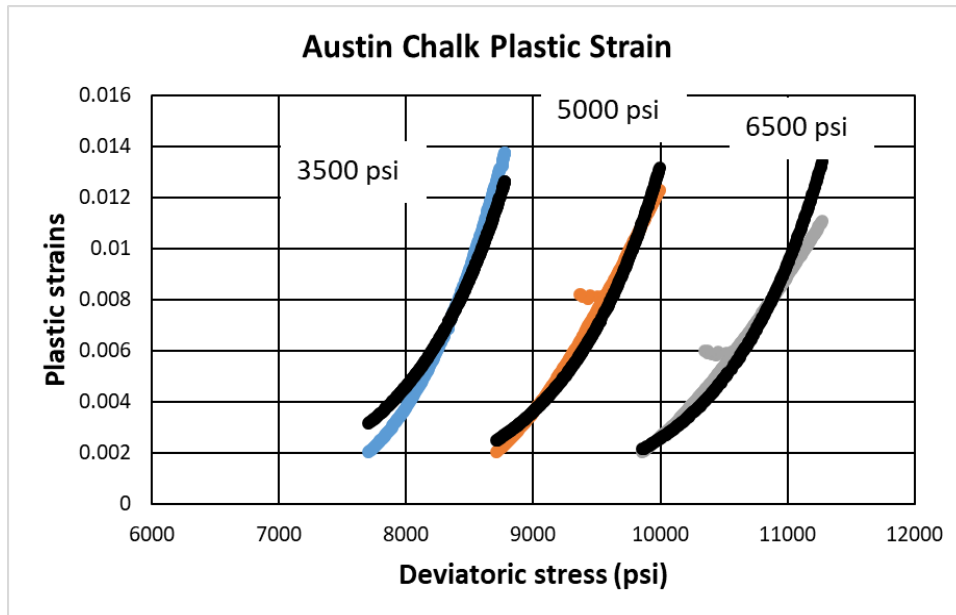


Figure 40: Plastic strains as a function of deviatoric stress for the Austin Chalk. The solid black lines are model predictions. A simple exponential is used to fit the data. The model is fit using only three parameters: ( $\eta_o$ ) 3.11E-3, ( $k_d$ ) 606 psi and ( $k_m$ ) -943 psi.

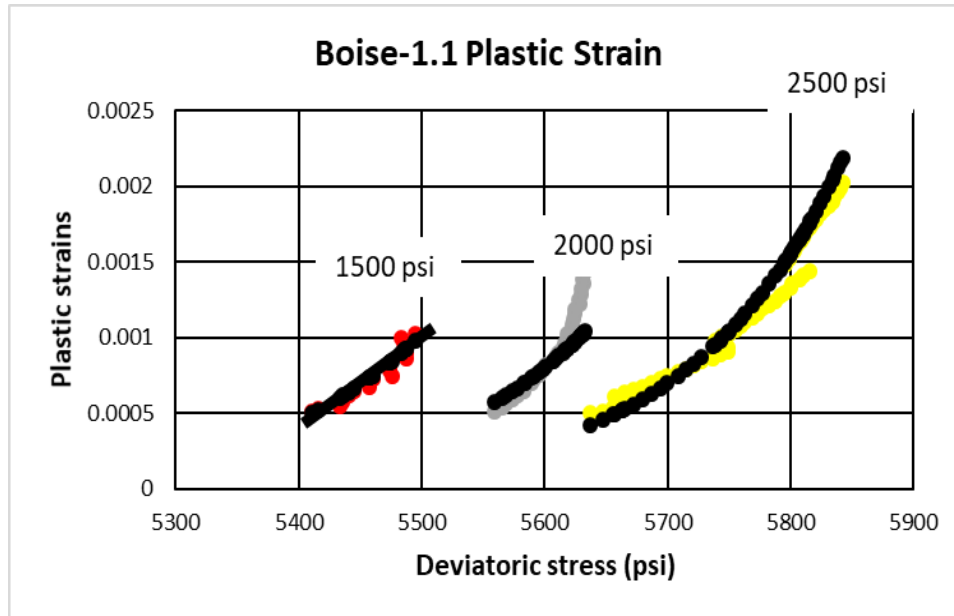


Figure 41: Plastic strains as a function of deviatoric stress for Boise-1 Sandstone. The solid black lines are model predictions. A simple exponential is used to fit the data. The model is fit using only three parameters: ( $\eta_o$ ) 5.05E-4, ( $k_d$ ) 115 psi and ( $k_m$ ) -505 psi.

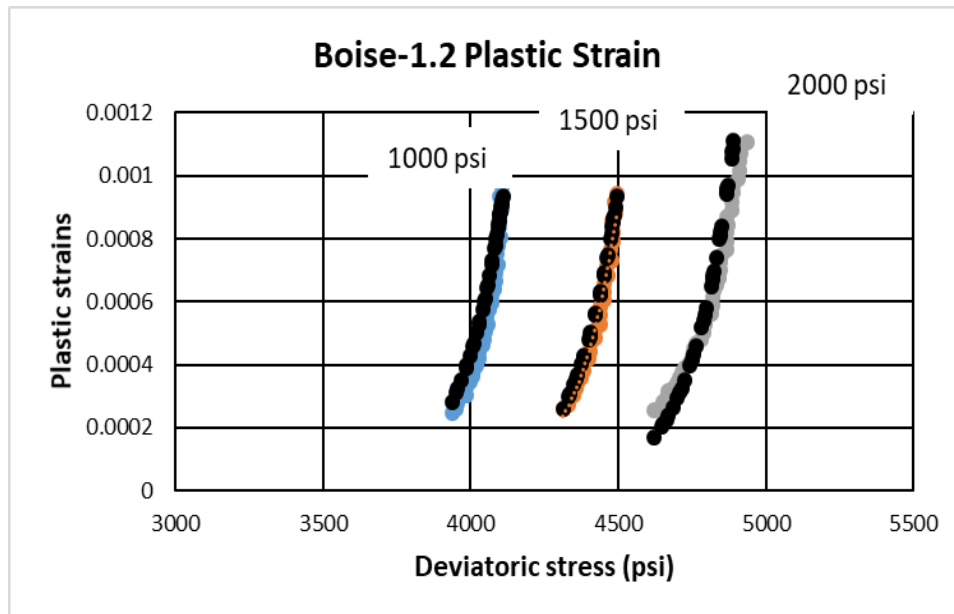


Figure 42: Plastic strains as a function of deviatoric stress for the Boise-2 Sandstone sample. The solid black lines are model predictions. A simple exponential is used to fit the data. The model is fit using only three parameters: ( $\eta_o$ ) 2.15E-4, ( $k_d$ ) 114 psi and ( $k_m$ ) -200 psi.

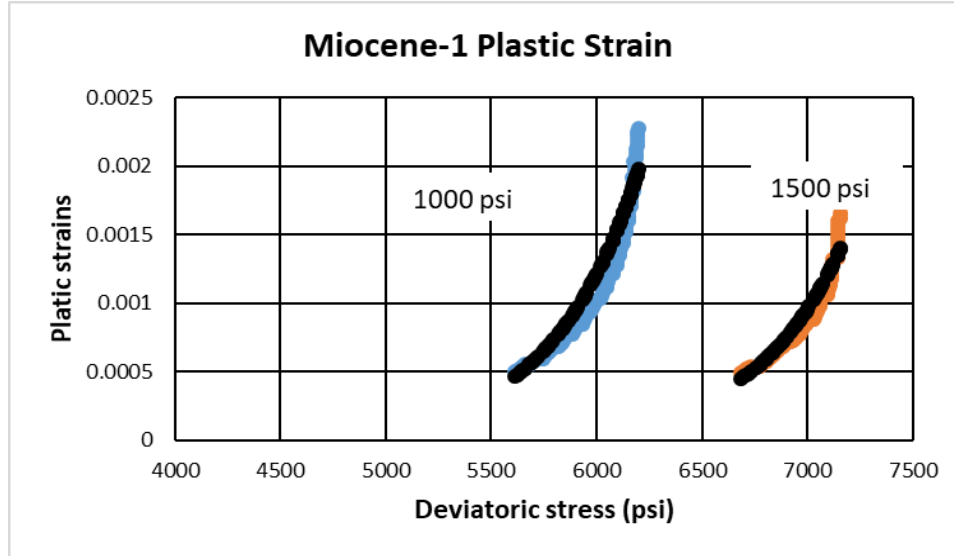


Figure 43: Plastic strains as a function of deviatoric stress for the Miocene-1 sandstone sample. The solid black lines are model predictions. A simple exponential is used to fit the data. The model is fit using only three parameters:  $(\eta_o)$  4.69E-5,  $(k_d)$  240 psi and  $(k_m)$  -195 psi.

## 2.4 Modeling Summary

The data are divided into linear elastic, nonlinear elastic, and irrecoverable strains:

- Linear elastic ( $M_1$ ): Directly predicted from the velocity data or a quadratic fit to the base case, as explained in section 2.3.2.
- Nonlinear elastic ( $M_2$ ): The nonlinear elastic term is correlated to the percent irrecoverable strain data and is directly predicted from the quadratic fit to the base case, as shown in section 2.3.3.
- Plastic strains( $\eta_o, k$ ): A network of nodes and bonds is used to predict irrecoverable strains, presented in detail in section 2.3.5. The modeling parameters are predicted by fitting the model to the base case.

In the next section, we have applied the modeling parameters to predict the triaxial test. The section shows the validity of the model. Two of the samples (Austin Chalk-2 and Miocene-2 are from the literature).

## Chapter 3: Predicting a Triaxial Test

### 3.1 Miocene sandstone Prediction

A multistage triaxial test is shown in figure 44a for the Miocene-1 sandstone sample. This test is named as sample "MR" (reference) as it is used as the reference test. The initial loading curve is at 500 psi confining stress, and the reloads curves are at 1000 psi and 1500 psi confining pressures, respectively. The sample "MR" data is then used to calibrate the modeling parameters.

A quadratic fit is applied to the reloads up to the point of maximum curvature, as discussed in section 2.3.1. The quadratic fit provides linear and non-linear elastic strain parameters  $M_1$  and  $M_2$ . Depending on the sample,  $M_1$  varies or remains constant with confining pressure, as shown in Figure 33. In contrast,  $M_2$  remains constant as a function of confining pressure for all of the samples, as discussed in section 2.3.3. In section 2.3.2, we have shown that  $M_1$  can also be directly predicted from an independent velocity measurement. This means that we can either use a velocity measurement or use the quadratic fit to data from a twin sample to get  $M_1$  at specified confining pressure.

The next step is to calculate the difference between the strains predicted by the quadratic fit and the actual strains measured for the reloads. These strains are labeled as plastic strains. The compaction model, discussed in section 2.3.5, is then applied on the plastic strains to estimate the parameters  $\eta_0$ ,  $k_d$  and  $k_m$ . All of the model parameters are summarized in Table 12.

The results of a single stage triaxial test may be predicted using these modeling parameters. To validate the predicted results, a separate single stage triaxial test was performed on a sample "MM" (measured) at a confining pressure of 500 psi. The sample "MM" is a twin for the sample "MR." Both the predicted result and the single

stage triaxial test data (sample "MM") are plotted in Figure 44b. The black line is the modeled data, and the blue line is the original experimental data. We observe that the model predicts the test data quite well.

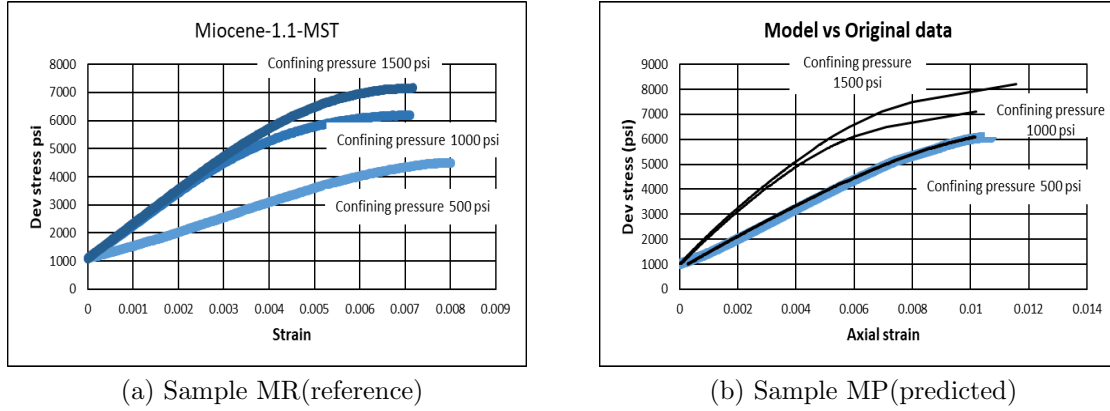


Figure 44: (A) Miocene sandstone MST data on sample "MR" that is used to calibrate the model to predict a triaxial test. (B) Sample "MM" data used to validate the model prediction. The predicted data are shown as black lines, and the measured data is shown in blue. The model predicts the measured data quite well.

Table 12: Miocene-1 Sandstone Model Parameters.

| Parameter                            | Value            |
|--------------------------------------|------------------|
| $M_1$ (psi)(500 psi conf. pressure)  | $6.6 * 10^5$     |
| $M_1$ (psi)(1000 psi conf. pressure) | $1.4 * 10^6$     |
| $M_1$ (psi)(1500 psi conf. pressure) | $1.5 * 10^6$     |
| $M_2$ (psi)                          | $-8 * 10^7$      |
| $\eta_o$                             | $4.69 * 10^{-5}$ |
| $k_m$ (psi)                          | -195             |
| $k_d$ (psi)                          | 245              |

Reloads for the triaxial test are predicted for higher confining pressures of 1000 psi and 1500 psi, as shown in Figure 44b using the above parameters.  $M_1$  is different for the reloads as it is dependent on confining pressure. The rest of the parameters are the same.

### 3.2 Castlegate Sandstone Prediction

Figure 45 shows the MST plot for the Castlegate Sandstone sample. The plot contains an initial loading curve and the model prediction. Model results are also shown for two higher confining pressures using the parameters shown in 13.

Table 13: Castlegate Sandstone Model parameters.

| Parameter                            | Value            |
|--------------------------------------|------------------|
| $M_1$ (psi) (500 psi conf. pressure) | $1.2 * 10^6$     |
| $M_1$ (psi)(1000 psi conf. pressure) | $1.38 * 10^6$    |
| $M_1$ (psi)(1500 psi conf. pressure) | $1.45 * 10^6$    |
| $M_2$ (psi)                          | $-5.3 * 10^7$    |
| $\eta_o$                             | $1.06 * 10^{-4}$ |
| $k_m$ (psi)                          | -633             |
| $k_d$ (psi)                          | 512              |

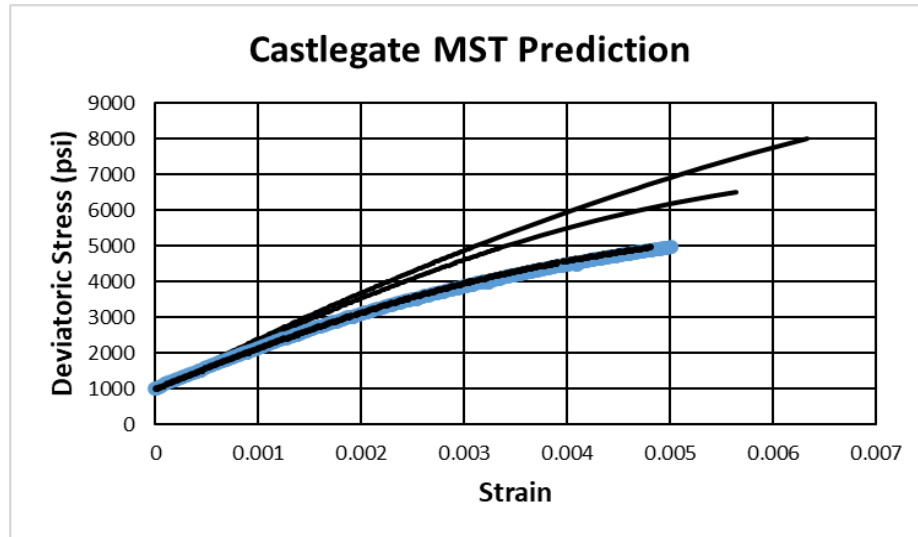


Figure 45: Castlegate Sandstone MST data for initial loading curve at 500 psi confining along with the model results at 500 psi, 1000 psi and 1500 psi confining pressures. The model predicts the initial loading curve quite well.

### 3.3 Berea Sandstone Prediction

Figure 46 shows the MST plot for the Berea Sandstone sample. The plot contains an initial loading curve and its prediction. Model results for two higher confining

pressures also shown. Because the recoverable strains are almost 93 percent, the data are adequately fit using  $M_1$  and  $M_2$ . There is no need to fit this model for plastic strains.

Table 14: Berea Model Parameters.

| Parameter                             | Value         |
|---------------------------------------|---------------|
| $M_1$ (psi) (1000 psi conf. pressure) | $2.2 * 10^6$  |
| $M_1$ (psi)(2000 psi conf. pressure)  | $3.0 * 10^6$  |
| $M_1$ (psi)(3000 psi conf. pressure)  | $3.36 * 10^6$ |
| $M_2$ (psi)                           | $-4.2 * 10^7$ |

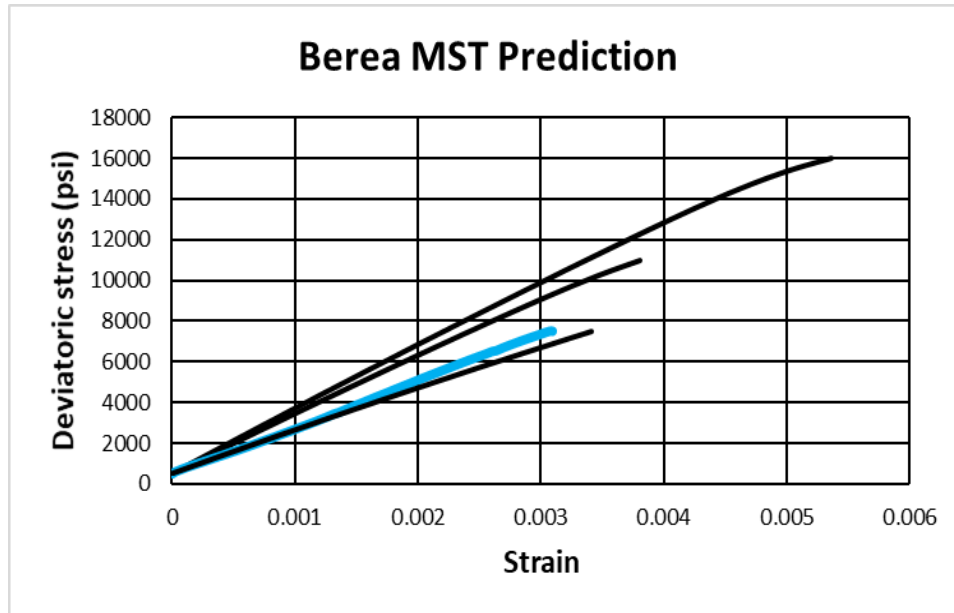


Figure 46: Berea MST data for the initial loading curve at 1000 psi confining stress along with model results for 1000 psi, 2000 psi and 3000 psi confining pressure. The model predicts the initial loading curve quite well.

### 3.4 Austin Chalk Prediction

Figure 47 shows the MST plot for the Austin Chalk sample. The plot contains an initial loading curve and the corresponding model prediction. Model results for two higher confining pressures are also shown using the parameters listed in table 15.

Table 15: Austin Chalk Model Parameters.

| Parameter                            | Value            |
|--------------------------------------|------------------|
| $M_1$ (psi) (500 psi conf. pressure) | $1.70 * 10^6$    |
| $M_1$ (psi)(1000 psi conf. pressure) | $1.75 * 10^6$    |
| $M_1$ (psi)(1500 psi conf. pressure) | $1.80 * 10^6$    |
| $M_2$ (psi)                          | $-1.0 * 10^8$    |
| $\eta_o$                             | $3.11 * 10^{-3}$ |
| $k_m$ (psi)                          | -943             |
| $k_d$ (psi)                          | 606              |

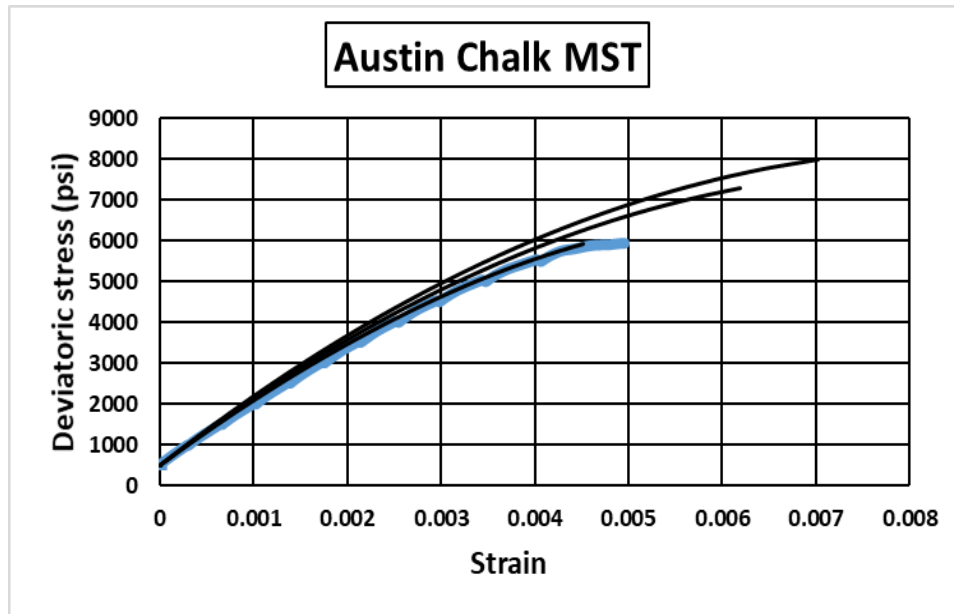


Figure 47: Austin Chalk MST data and model results for the initial loading curve at 500 psi confining along with the predicted data at 1000 psi, and 1500 psi confining pressures. The model predicts the initial loading curve quite well.

### 3.5 Fontainebleau Sandstone Prediction

Figure 48 shows the MST plot for the Fontainebleau Sandstone. The plot contains an initial loading curve and its modeled prediction. Stress-strain curves are also predicted for two higher confining pressures using the parameters shown in table 16. Because the recoverable strains are almost 98 percent, the data are adequately fit using  $M_1$  and  $M_2$ . There is no need to fit this model for plastic strains.

Table 16: Fontainebleau Sandstone Model Parameters.

| Parameter                            | Value         |
|--------------------------------------|---------------|
| $M_1$ (psi) (500 psi conf. pressure) | $1.70 * 10^6$ |
| $M_1$ (psi)(1000 psi conf. pressure) | $1.75 * 10^6$ |
| $M_1$ (psi)(1500 psi conf. pressure) | $1.80 * 10^6$ |
| $M_2$ (psi)                          | $-1.0 * 10^8$ |

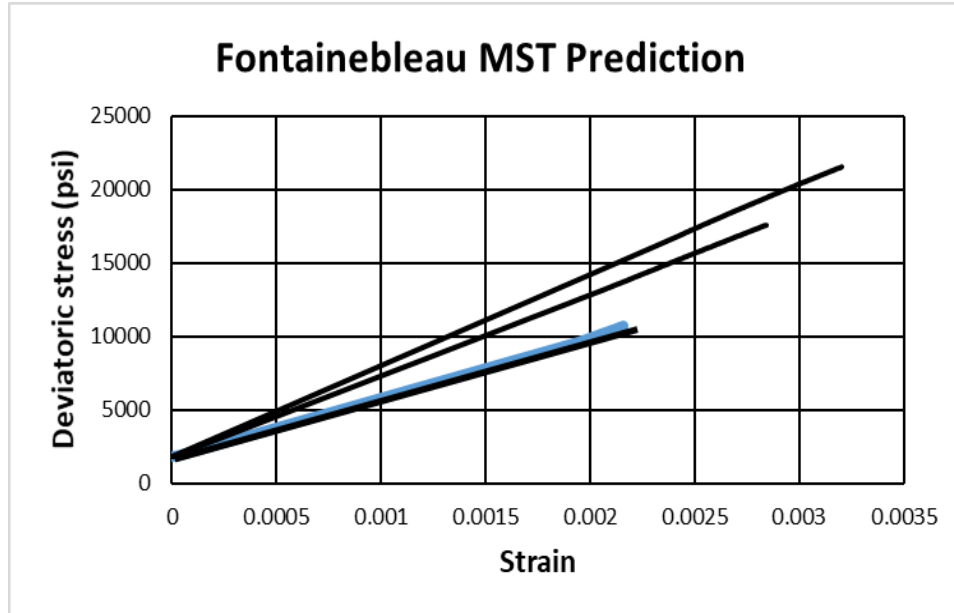


Figure 48: Fontainebleau Sandstone MST data for the initial loading curve at 1000 psi confining stress shown together with the model results at 500 psi, 1000 psi and 1500 psi confining pressures. The model predicts the initial loading curve quite well.

For the Miocene sandstone sample, a single stage triaxial test was run to validate the prediction from the multistage triaxial test. For the rest of the samples, the single stage data were not available. So, the initial loading curve from the multistage test was used to validate the modeling parameters, as shown above (Al-Salman et al. 2015) ran multistage tests along with single stage triaxial tests at different confining pressures. This set of data provided us with the opportunity to validate the modeling parameters by predicting the single stage triaxial test results at multiple confining pressures. Below are Austin Chalk and Miocene sandstone data for tests performed

by Al-Salman et al. (2015). The original MST and SST data are shown, and plotted together with the model prediction.

### 3.6 Austin Chalk-2 Prediction

Figure 49 shows the MST and SST axial stress versus strain plot for the Austin Chalk-2 sample. This test was performed by Al Salman et al. (2015). The MST test has been used to calibrate the model and to predict single stage triaxial test results on four different samples. The modeling parameters are shown in Table 17. Please note that  $M_1$  at different confining pressures is obtained from the velocity data. The rest of the parameters have been obtained from the MST test.

Table 17: Austin Chalk-2 Model Parameters.

| Parameter                            | Value            |
|--------------------------------------|------------------|
| $M_1$ (psi)(500 psi conf. pressure)  | $1.67 * 10^6$    |
| $M_1$ (psi)(1000 psi conf. pressure) | $1.77 * 10^6$    |
| $M_1$ (psi)(1500 psi conf. pressure) | $1.67 * 10^6$    |
| $M_1$ (psi)(2000 psi conf. pressure) | $1.61 * 10^6$    |
| $M_2$ (psi)                          | $-7 * 10^7$      |
| $\eta_o$                             | $4.22 * 10^{-4}$ |
| $k_m$ (psi)                          | -1100            |
| $k_d$ (psi)                          | 1000             |

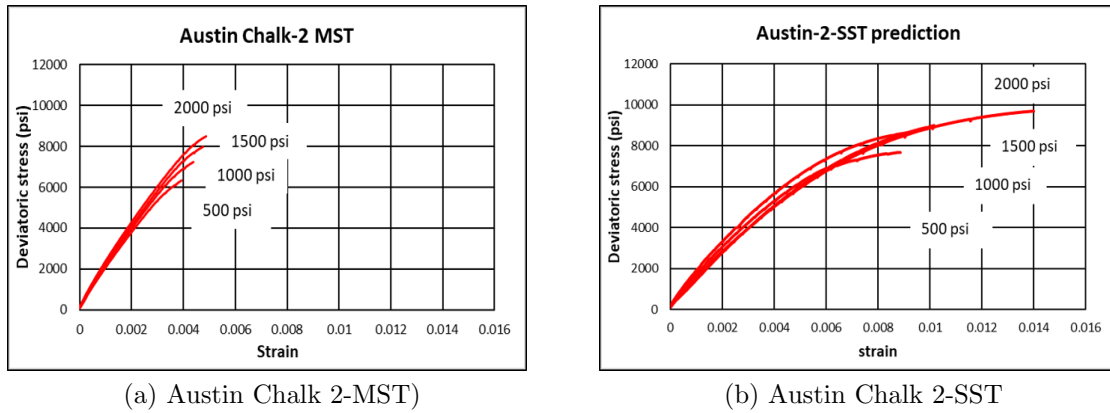


Figure 49: Austin Chalk-2 MST and SST tests plot. The test was performed by Al Salman et al. (2015). The MST test was used to calibrate the model. The results were then used to predict single stage triaxial tests.

Figure 50 shows the single stage tests run at 500, 1000, 1500 and 2000 psi confining pressures. These tests were performed on the twin samples of the Austin Chalk-2 by Al-Salman et al. (2015). The red curve is the original raw data. The black curve shows the model prediction made using the parameters shown in Table 17. The comparison shows that the model predicts the individual triaxial test data within 1-2% of the original data.

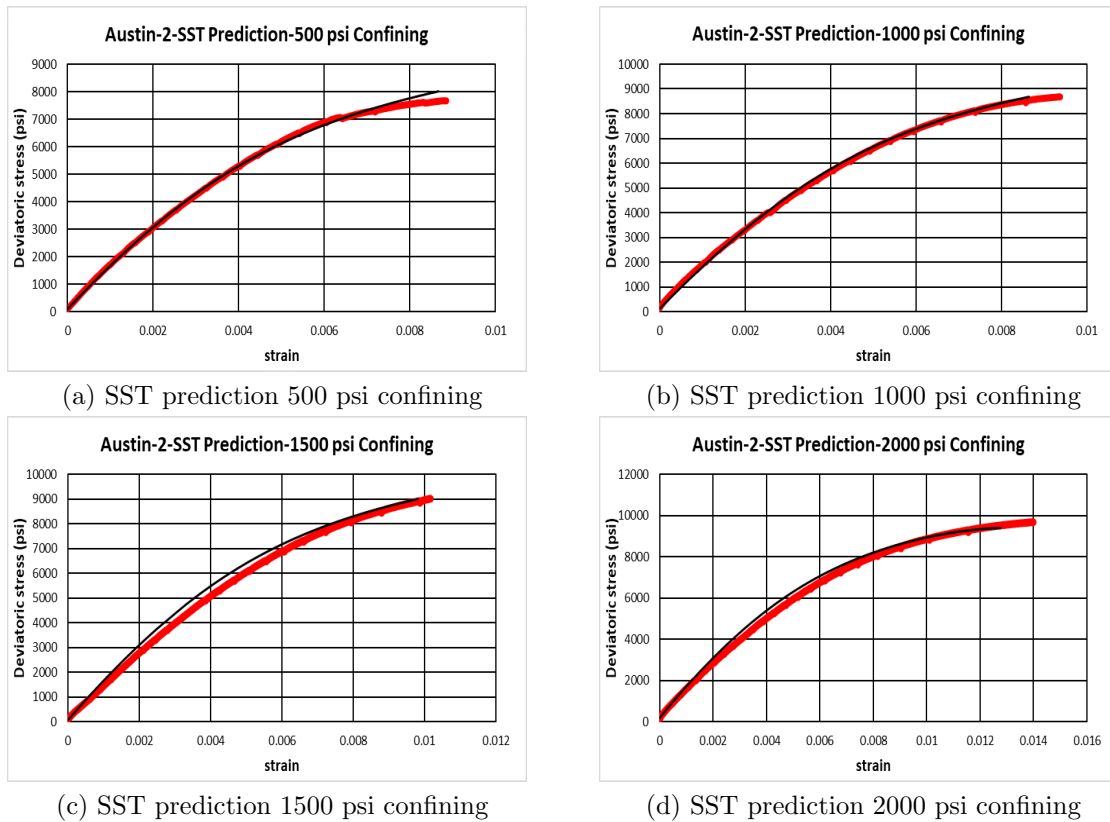


Figure 50: SST data prediction for four Austin Chalk samples at four different confining pressures. The red lines show the raw data, and the black lines show the model predictions. The model predicts the single stage test data within 1-2% of the original data.

### 3.7 Miocene-2 sandstone Prediction

Figure 51 shows the MST and SST axial stress vs strain plots for the Miocene-2 sandstone sample. The Miocene sandstone was also tested by Al Salmon et al. (2015). This MST has been used to calibrate the model and predict single stage triaxial tests

for four different core plugs. The model parameters are shown in Table 18. Please note that  $M_1$  at different confining pressures is obtained from the velocity data. The rest of the parameters have been obtained from the MST test results.

Table 18: Miocene-2 sandstone Model Parameters.

| Parameter                            | Value            |
|--------------------------------------|------------------|
| $M_1$ (psi)(500 psi conf. pressure)  | $1.40 * 10^6$    |
| $M_1$ (psi)(1000 psi conf. pressure) | $1.13 * 10^6$    |
| $M_1$ (psi)(1500 psi conf. pressure) | $1.78 * 10^6$    |
| $M_1$ (psi)(2000 psi conf. pressure) | $1.00 * 10^6$    |
| $M_2$ (psi)                          | $-2.2 * 10^7$    |
| $\eta_o$                             | $7.86 * 10^{-5}$ |
| $k_m$ (psi)                          | -210             |
| $k_d$ (psi)                          | 313              |

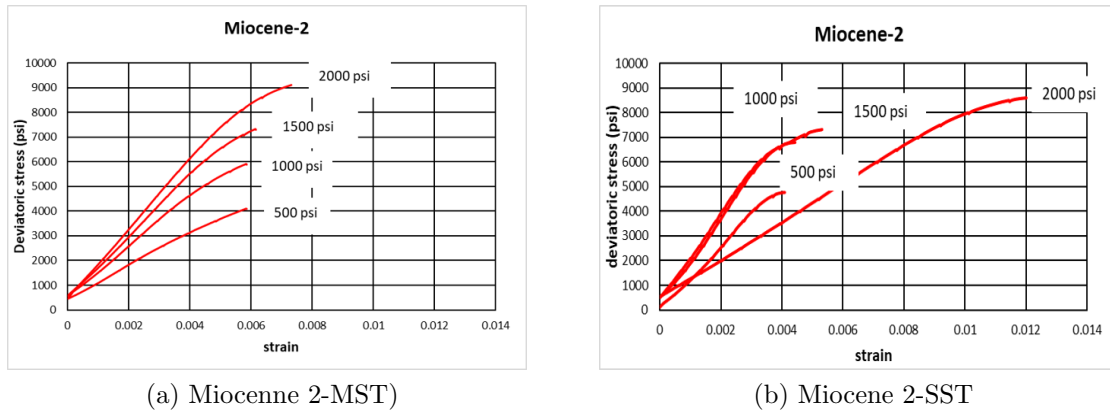


Figure 51: Miocene-2 sandstone MST and SST tests plot. The test was performed by Al Salman et al. (2015). The MST test was used to calibrate the model. The results were then used to predict single stage triaxial tests.

Figure 52 shows the single stage tests performed at 500, 1000, 1500 and 2000 psi confining pressures. These tests were performed on twin samples to this study’s Miocene-2 sandstone by Al Salman et al. (2015). The red curves show the original raw data. The black curves show the model predictions made using the parameters shown in Table 17. The comparison shows that the model predicts the individual triaxial test data quite well for 1500 and 2000 psi confining pressures (2-3% error).

For 500 psi and 1000 psi confining pressures, the model deviates somewhat at higher deviatoric stress (5-7% error). One potential interpretation of this observation is that the samples are not proper twins for one another.

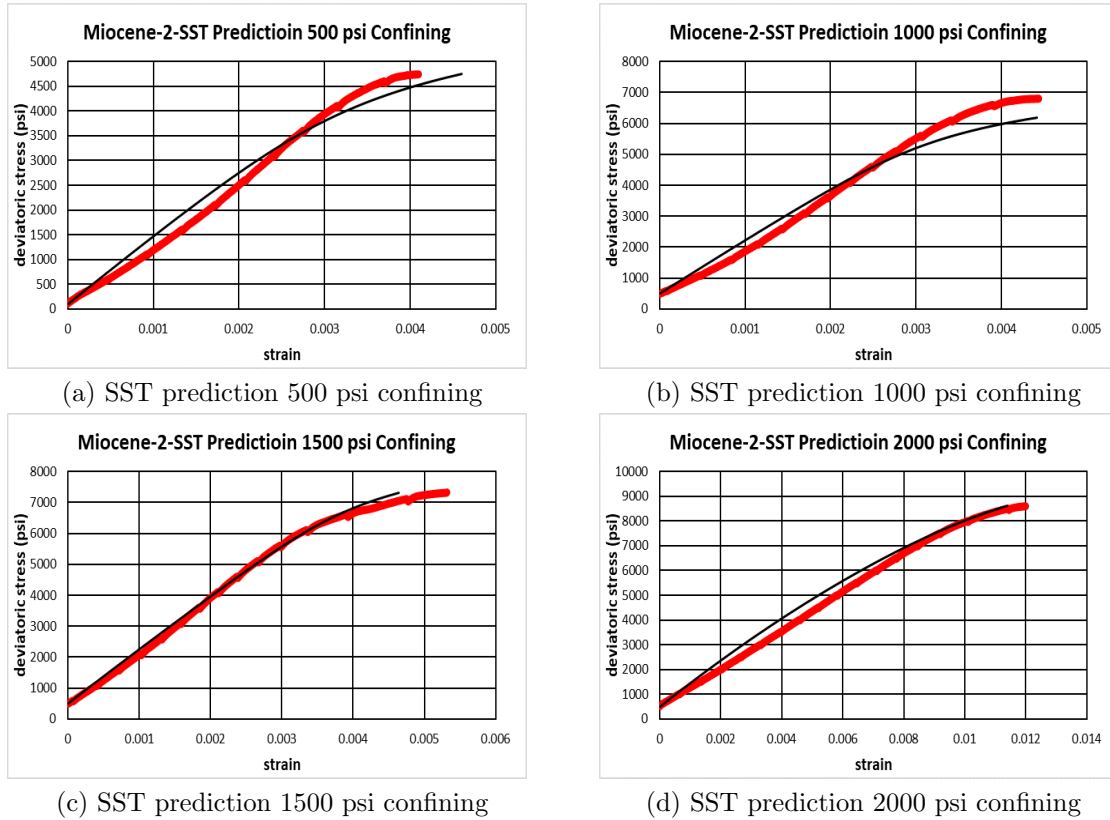


Figure 52: SST data prediction for Miocene sandstone at four different confining pressures. The red line is the raw data, and the black line is the model prediction. The model predicts the data quite well.

### 3.8 Generalized Stress Path for Plastic Strains

We have extended the compaction model to predict plastic strains along any stress path by calibrating the model parameters using triaxial stress path data (Equation 32). Figure 53 shows the plastic strains calculated for the Miocene-1 sandstone sample discussed in the previous section. The plastic strains are predicted for a constant mean stress path, shown in figure 53a and for constant deviatoric stress path, shown in figure 53b. As expected, the plastic strains increase due to increases in the deviatoric

stress (const. mean stress test), and decrease due to increases in the mean stress (const. deviatoric stress test). Future work will involve verifying these predictions by comparing to laboratory tests run under these conditions.

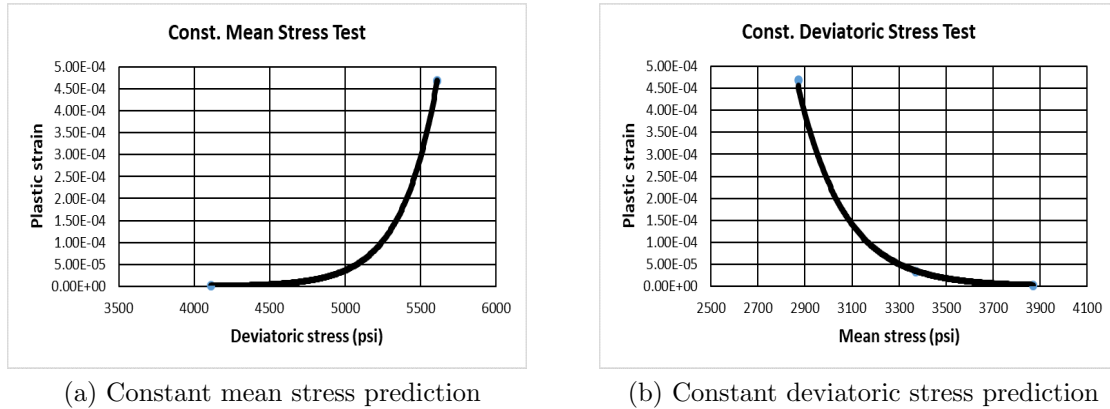


Figure 53: (A) Constant mean stress prediction. (B) Constant deviatoric stress prediction. The plastic strains increase due to increasing deviatoric stress (const. mean stress test), and decrease due to increasing mean stress (const. deviatoric stress test).

### 3.8.1 Matlab GUI

Figure 54 shows model predictions for plastic strains along varying stress paths. The figure was generated using a model program run in Matlab. The program takes  $(\eta_o, k_d, k_m)$  as inputs and calculates plastic strains as a function of stress path. The first figure shows plastic strains for a triaxial stress path. As both mean and deviatoric stresses are changing, the plastic strains are plotted on a surface. The second figure shows plastic strains for both constant mean and constant deviatoric stress. The third and fourth figures are 2D projections of model results for constant mean stress and constant deviatoric stress paths. As expected, for constant mean stress, plastic strains increase with increasing deviatoric stress. Similarly, for constant deviatoric stress, the plastic strains decrease with increasing mean stress. Qualitatively, the modeled plastic strains for the constant mean and constant deviatoric stress paths are correct. Future work will involve performing constant mean and constant deviatoric

stress path experiments and then validating the results by making predictions from a triaxial stress path. This is a pretty unique and exciting result. If this proves to be correct this is a giant leap forward in our ability to model the stress strain behavior of rocks.

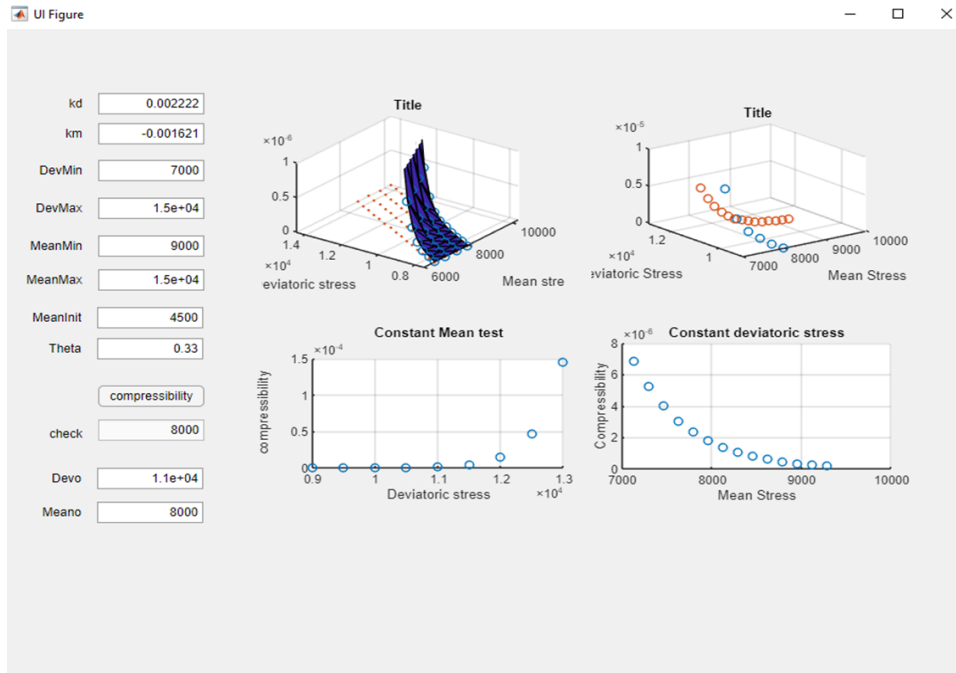


Figure 54: Matlab interface for calculating plastic strains along different stress paths. The model is calibrated from a triaxial stress path to predict other stress paths. The first figure is a triaxial stress path. The second shows the predicted constant mean and constant deviatoric stress path results. The third and fourth are the 2D projections of figure 2. As expected, the plastic strains increase for increasing deviatoric stress and decrease for increasing mean stress.

## Chapter 4: Sample Characterization

The purpose of this chapter is to provide quantitative visual insight into sample deformation. Thin sections were analyzed for samples of the Fontainebleau Sandstone, Boise Sandstone, and Miocene sandstone. Both pre-test and post-test thin sections were analyzed in order to quantify potential controlling sample characteristics and the induced strains. Thin sections were scanned using transmitted light, and cross polarized light, at 0 and 45 degree polarizer rotations from a Zeiss Axio Imager with an automated stage. The purpose of obtaining multiple images in transmitted light was to obtain framework grain compositional information not directly available in transmitted light alone. The following information was obtained using thin section analysis:

- Porosity % (total area of segmented pores/total area analyzed)
- Contact ratio (total length of grain contacts/total framework grain perimeter)
- Cement % (total area of mineral cements/total area analyzed)
- Number of Cracks, total length of induced cracks, and crack orientation
- Framework Grain Mineralogy

In this section we discuss these properties for the samples that were analyzed. The objective is to understand the modeling parameters as a function of sample characterization.

### 4.1 Fontainebleau-1 Sandstone Characterization

MST tests were run on two sets of two Fontainebleau Sandstones, as discussed in section 2.2.5. Figure 55 shows the full scale thin section scan of a Pre-test

Fontainebleau Sandstone. The whole thin section was not analyzed. Instead, the thin section was divided into smaller tiles, and they were analyzed until the analyzed statistics became constant as a function of the number of tiles analyzed.



Figure 55: Pre-test Fontainebleau-1 Sandstone thin-section. The black circles show the regions from which tiles were selected for quantitative analysis. The scale bar is 0.2 in.

On average, 150 framework grains were analyzed for each sample, which resulted in stable values for mineralogy, and contact. Any more grains analyzed did not change the overall statistics. This was equivalent to 7 to 8 small tiles. The black circles on Figure 55 show the regions where the tiles were selected to be analyzed. Figure 56 shows a single tile under transmitted light, and its analysis using internally developed software named QPI (Quantitative Petrographic Interpretation ).

The porosity is quantified first, as shown in figure 57a. The software samples a representative region of the blue dyed epoxy. The color associated with porosity can then be expanded until the entire porosity area is selected. In this image, the porosity is on the order of 12%. The next step is to hand draw all the contacts

among grains, as shown in 57b. The contacts are shown as red lines. -The contact ratio is calculated by dividing the total length of the contacts among grains by the total grain perimeter. For the Fontainebleau-1 Sandstone, the contact ratio is 0.22 (or 22%). After identifying grain contacts, quartz cement is quantified, as shown in 57c. Finally, the framework grain mineralogy is selected, and the final analyzed image is shown in figure 57d. In this case, all the grains are quartz. The yellow color grains are mono quartz, and the mustard color is poly quartz.

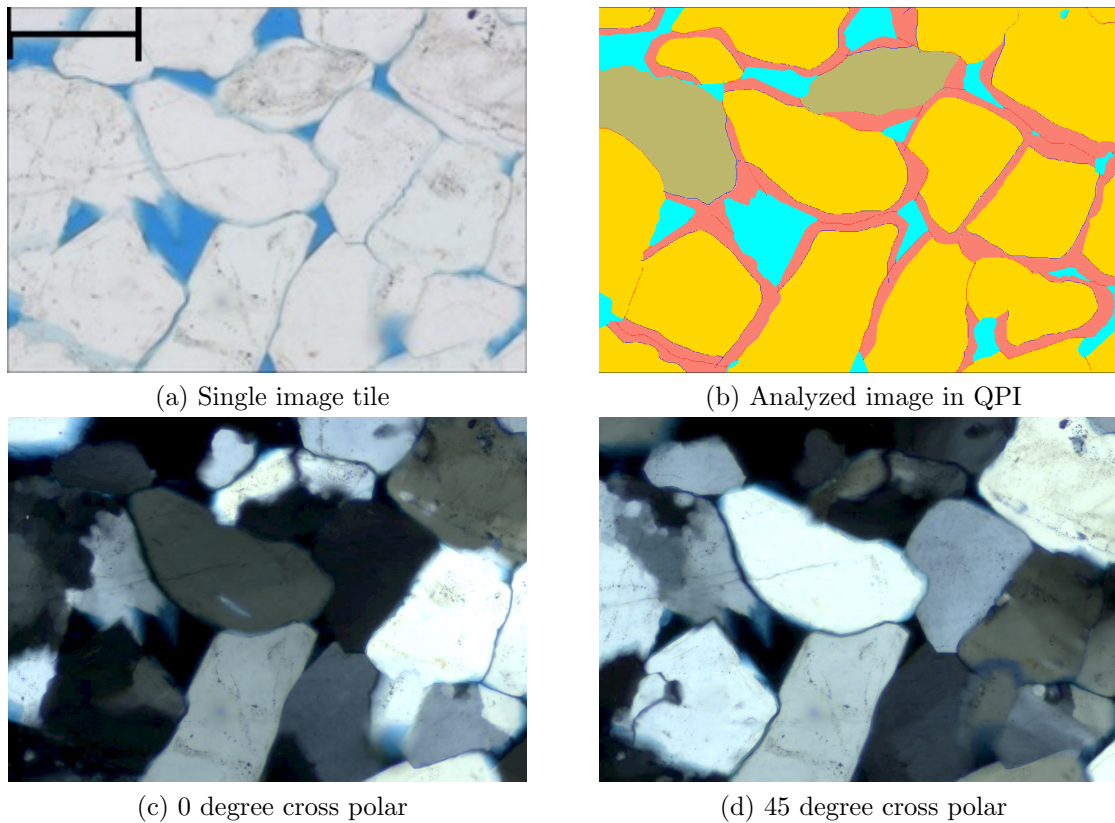


Figure 56: The analyzed image shows the sampled porosity, percentage cement, contacts between grains, and sampled grains. The scale bar is 200 microns.

Figure 58 shows the post-test axial thin section of the Fontainebleau-1.10 Sandstone sample. This sample was run to a confining pressure of 2500 psi (high stress stage). An incipient failure surface can be seen at the top left of the thin section image. The black circles show the regions from which the tiles were selected to be analyzed.

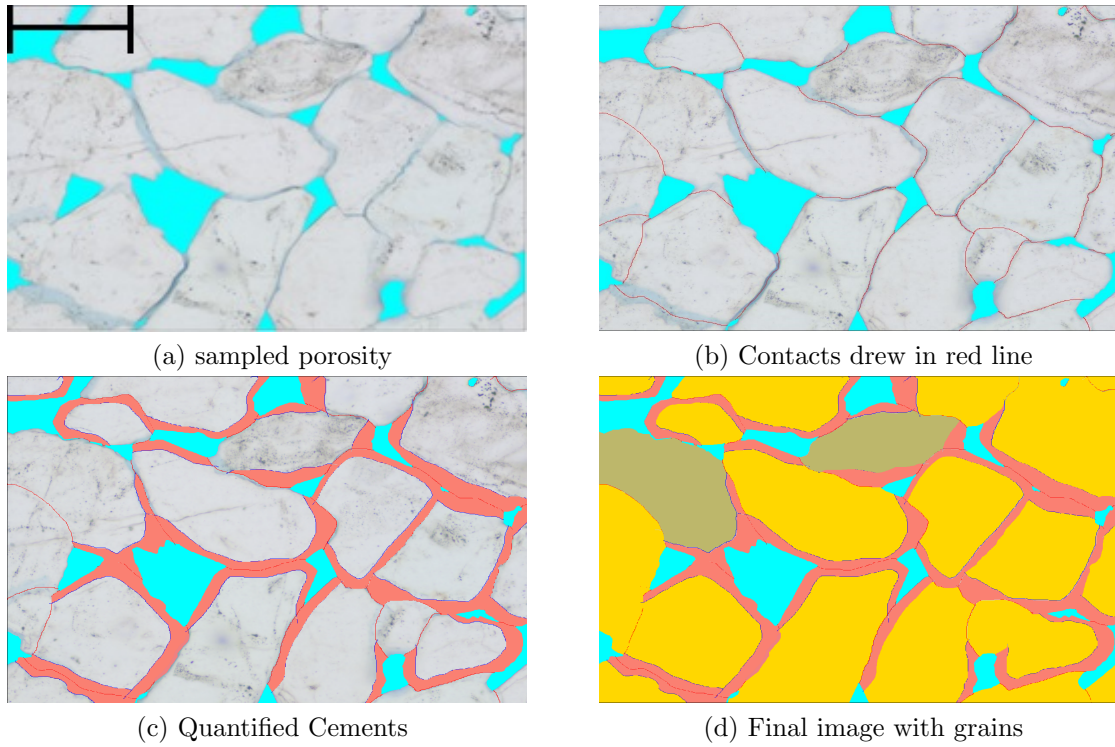


Figure 57: Workflow used to analyze the Fontainebleau Sandstone thin section. First, the porosity (13%) is quantified, then contacts (22%), then cements (18%), and finally, grains are quantified. The scale bar is 200 microns.



Figure 58: Post-test Fontainebleau-1-10 Sandstone thin-section image showing regions of interest. The sample was tested to a confining pressure of 2500 psi. An incipient failure surface can be seen in the thin-section. The black circles are the regions from which tiles were selected for detailed analysis. The scale bar is 0.2 in.

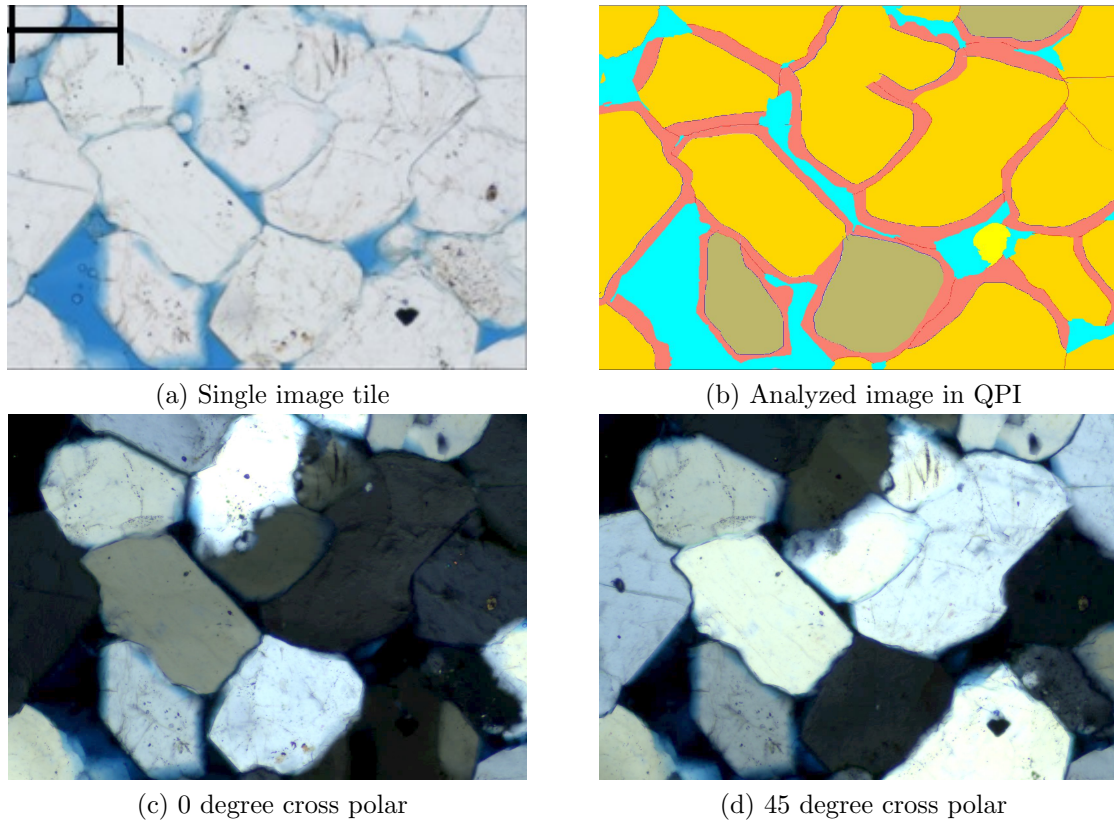


Figure 59: The analyzed image shows the sampled porosity, percentage cement, contacts between grains and sampled grains. The scale bar is 200 microns.

Figure 59 shows a single image tile in transmitted light, and its analysis using the QPI software. The sampled porosity is approximately 12%, shown in the blue color. The cement volume is approximately 14%. The cements are the regions colored pink occurring as overgrowths on framework grains. The contact ratio among grains is on the order of 0.26, or 26%. The yellow grains are mono quartz and the mustard colored grains are poly quartz.

Figure 60 shows the post-test thin section of the Fontainebleau-1.9 Sandstone sample. This sample was run to a confining pressure of 2000 psi (mid stress stage) confining pressure. The black circles are the regions from which the tiles were selected to be analyzed.

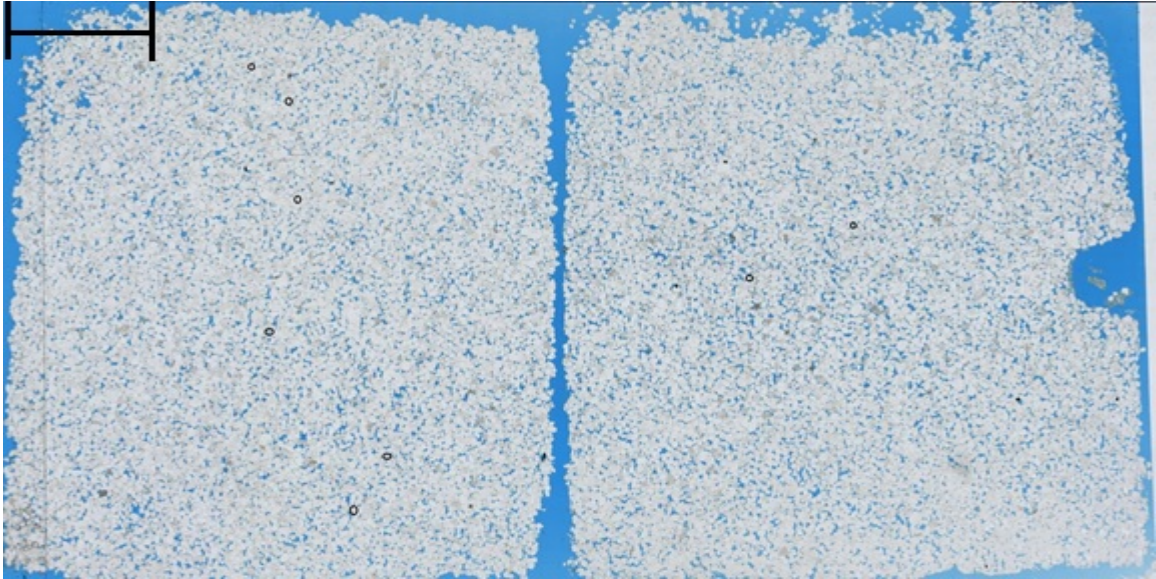


Figure 60: Post-test Fontainebleau-1-9 Sandstone thin-section. The sample was run to a confining pressure of 2000 psi. The black circled regions indicate where the tiles were selected for analysis. The scale bar is 0.2 inch.

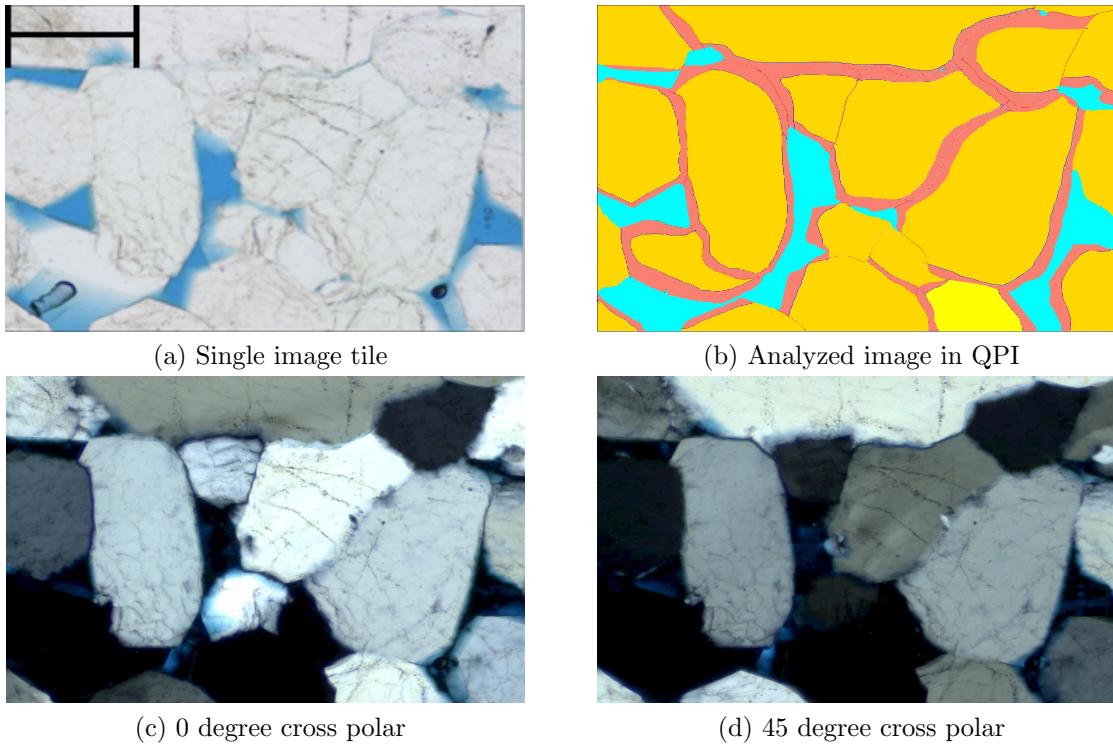


Figure 61: The analyzed image shows the sampled porosity (12%), percentage cement (17%), contacts (26%) between grains, and sampled grains. The scale bar is 200 microns.

Figure 61 shows a single image tile in transmitted light, and its analysis using the QPI software. The sampled porosity is on the order of 10%, shown in blue color. The cement volume approximately 17%. The cements are the regions colored pink occurring as overgrowths on framework grains. The contact ratio among grains is approximately 0.26. All the grains are mono quartz.

Table 19 contains a summary of the characterization data for one pre-test and two post-test samples of the Fontainebleau-1 Sandstone. There is a slight reduction in porosity with increasing confining pressure. This is expected as porosity decreases with increasing stress. The cement volume is almost constant. The contact ratio has increased. This is also expected as a result of applied stresses and porosity decrease.

Table 19: Fontainebleau-1 Sandstone sample characterization summary.

| Sample name | Confining pressure (psi) | Porosity (%) | Cements (%) | Contact ratio (%) |
|-------------|--------------------------|--------------|-------------|-------------------|
| FB-Pre      | 0                        | 13           | 18          | 22                |
| FB-1-9      | 2000                     | 12           | 17          | 26                |
| FB-1-10     | 2500                     | 10           | 17          | 26                |

The cracks were counted separately by drawing them individually on each tile. The purpose was to quantify the cracks present in the samples pre-test and post-test. Specifically, we were interested in how the cracks evolve from pre-test to post-test (intermediate stress stage) and post-test (final stress stage). The following criteria was used to quantify a crack:

- A crack is identified if it is preferentially oriented with respect to a present day grain contact at which stresses would be transmitted during testing.
- A crack is identified if it is oriented with respect to present day grain contact.
- A crack is also quantified if it connects along a contact and propagates through the adjacent grains and cements boundaries.

On average, 30% of the whole thinsection was examined. That area was sufficient so that crack statistics stabilized, as shown in figure 62. The mean number of cracks analyzed stabilized after 6 image tiles were measured. Examining more images did not change the mean number of cracks. The number of cracks was then normalized to per centimeter square area.

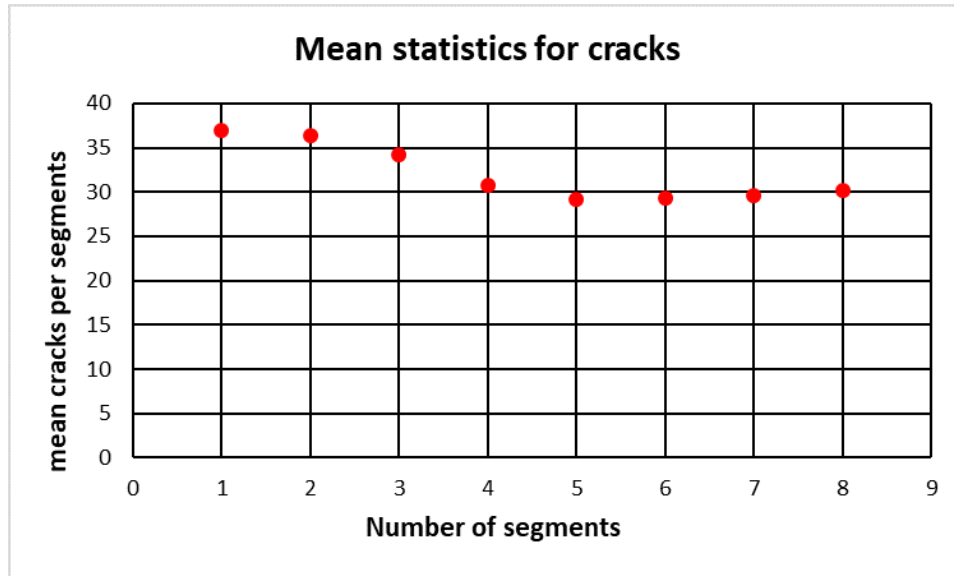


Figure 62: Mean cracks as a function of the number of image tiles analyzed for the Fontainebleau 1.9 Sandstone sample. The mean stabilizes after segment number 6.

Figure 63 shows a post-test sample image tile for the Fontainebleau 1.10 Sandstone sample. The cracks are generated during the MST test. Figure 64 shows the analyzed image. The cracks are drawn in red and identified by hand. The cracks are counted, and their orientation is determined using QPI. The cracks were identified following the protocols outlined above.

Table 20 shows the total number of incremental cracks per square centimeter for one Fontainebleau-1 pre-test and two post-test samples. Incremental cracks are those cracks that are generated only at the specified stress stage. The table also contains a column for vertical cracks only. The vertical cracks were identified as those whose orientation was at a greater than 45 degree angle.

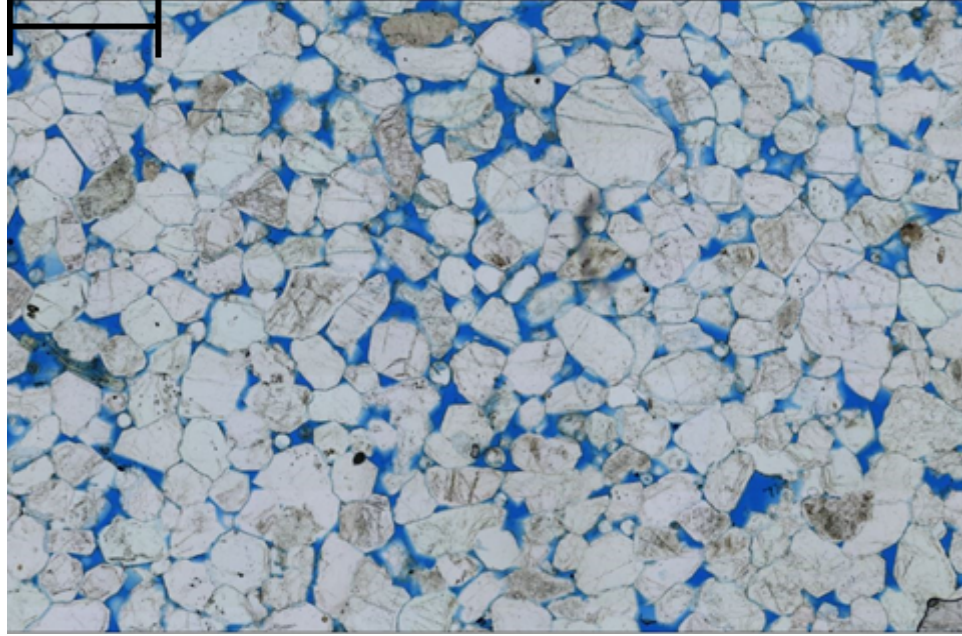


Figure 63: The post-test image for Fontainebleau 1.10 Sandstone shows the cracks generated during a MST test. The scale bar is 1000 microns.

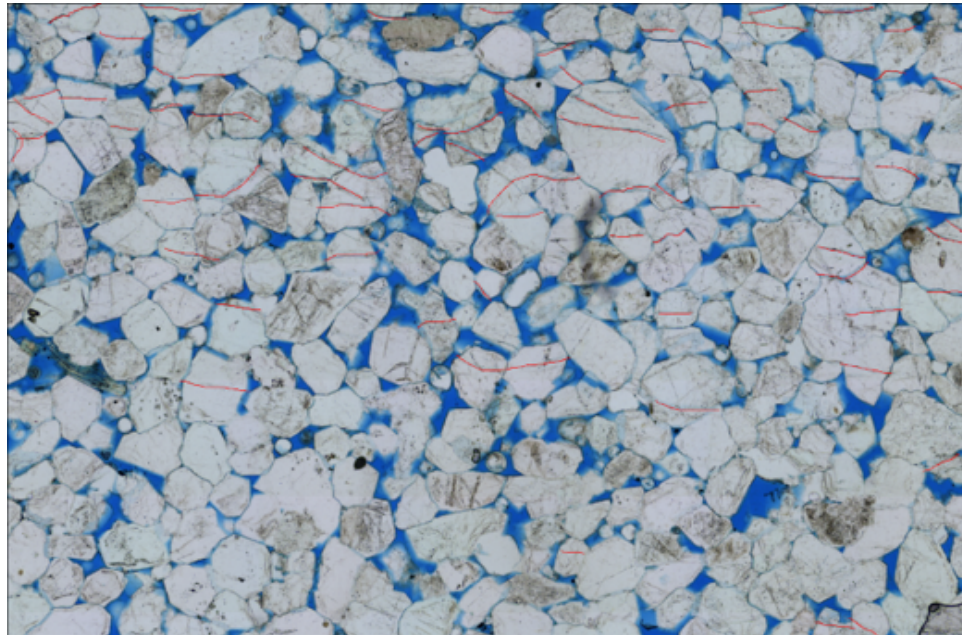


Figure 64: The analyzed image for Fontainebleau 1.10 Sandstone shows the cracks drawn on the tile with a red line. The cracks are counted along with their orientation.

Table 20: Fontainebleau-1 Sandstone sample cracks summary.

| Sample name | Confining pressure | incremental cracks/cm.sq | Vertical inc. cracks/cm.sq |
|-------------|--------------------|--------------------------|----------------------------|
| FB-Pre      | 0                  | 9                        | 9                          |
| FB-1-9      | 2000               | 79                       | 73                         |
| FB-1-10     | 2500               | 272                      | 237                        |

Figure 65 shows the total number of incremental vertical cracks versus end stage stress. There is an exponential relationship. This shows that the sample is approaching failure at a higher stage, and corresponds to the exponential increase in acoustic emission events as a function of stress observed by Prakash (2018 ).

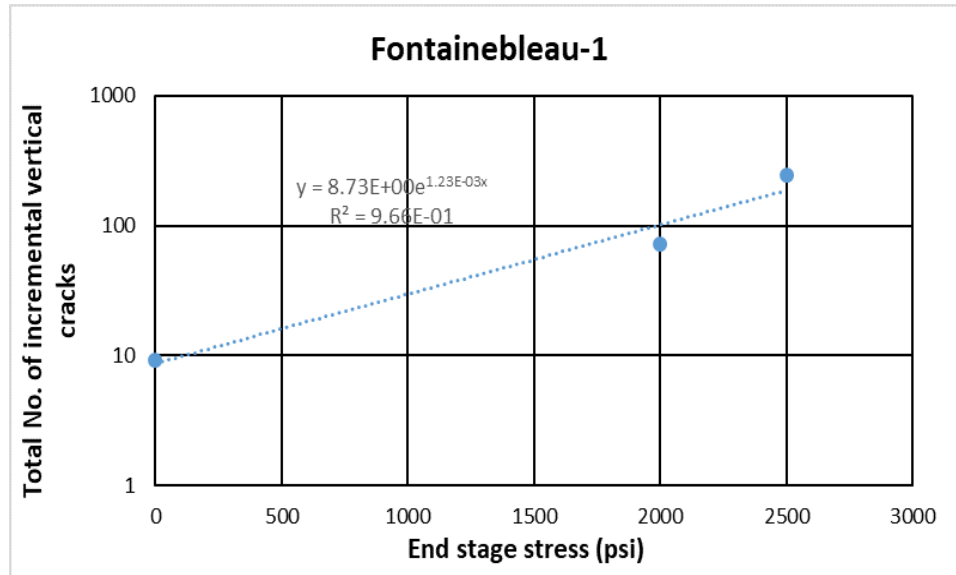


Figure 65: There is an exponential relationship between the total number of cracks as a function of increasing stress stage.

## 4.2 Fontainebleau-3 Sandstone Characterization

Similar analyses were performed on Fontainebleau-3 Sandstone as those described for the Fontainebleau-1 sandstone sample. The Fontainebleau-3 Sandstone has a permeability of 1 mD. Figure 66 shows the full scale thin section of pre-test Fontainebleau-3 Sandstone. Similar to the approach outlined above, the whole thin section was not

analyzed. Rather, the thin section was divided into smaller tiles, and they were analyzed until the statistics became constant as a function of the number of tiles analyzed.

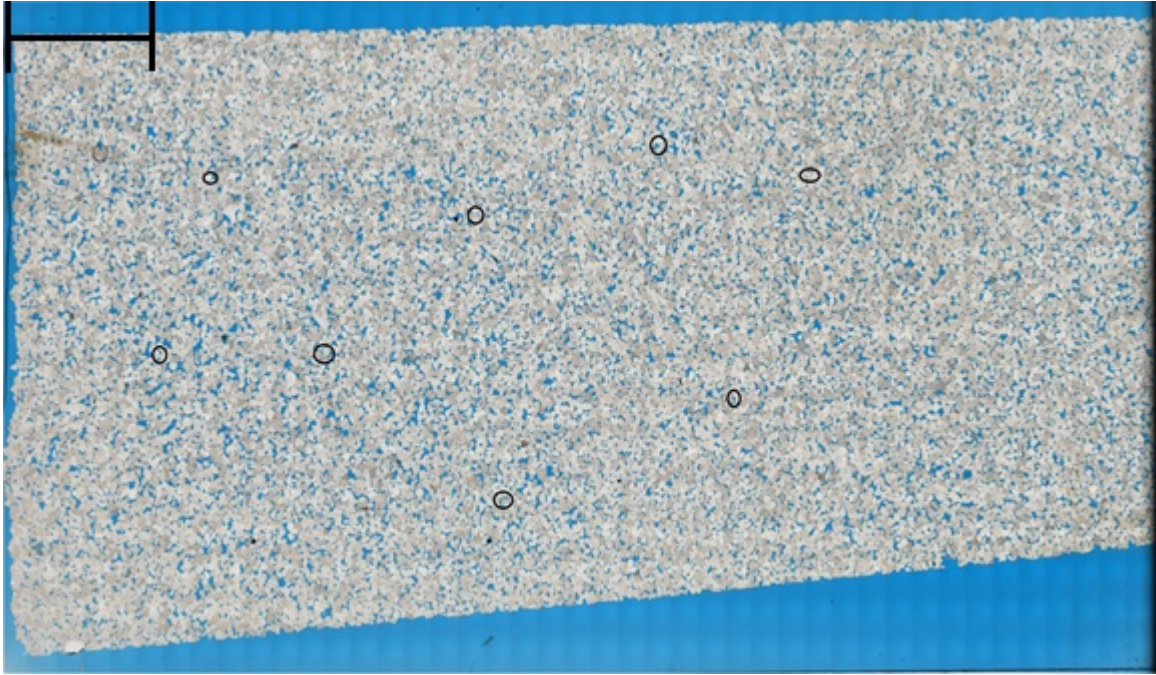
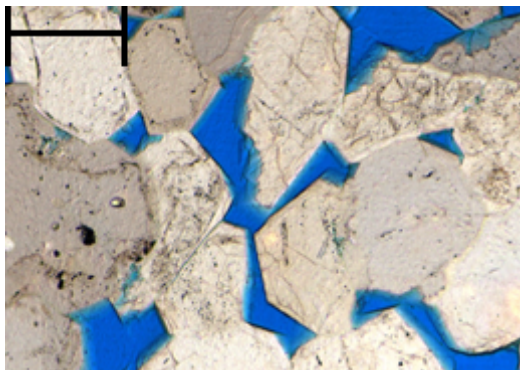
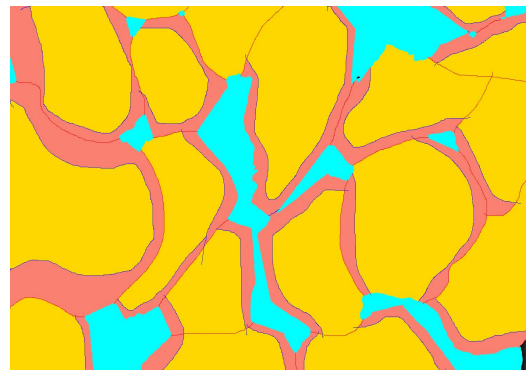


Figure 66: Pre-test Fontainebleau-3 Sandstone thin-section. The black circles are the regions from which the tiles were selected to be analyzed. The scale bar is 0.2 inch.



(a) Single image tile



(b) Analyzed image in QPI

Figure 67: The analyzed image for the Fontainebleau-3 Sandstone pre-test shows the sampled porosity (12%), percentage cement (15%), contacts between grains (27%), and sampled grains. The scale bar is 200 microns.

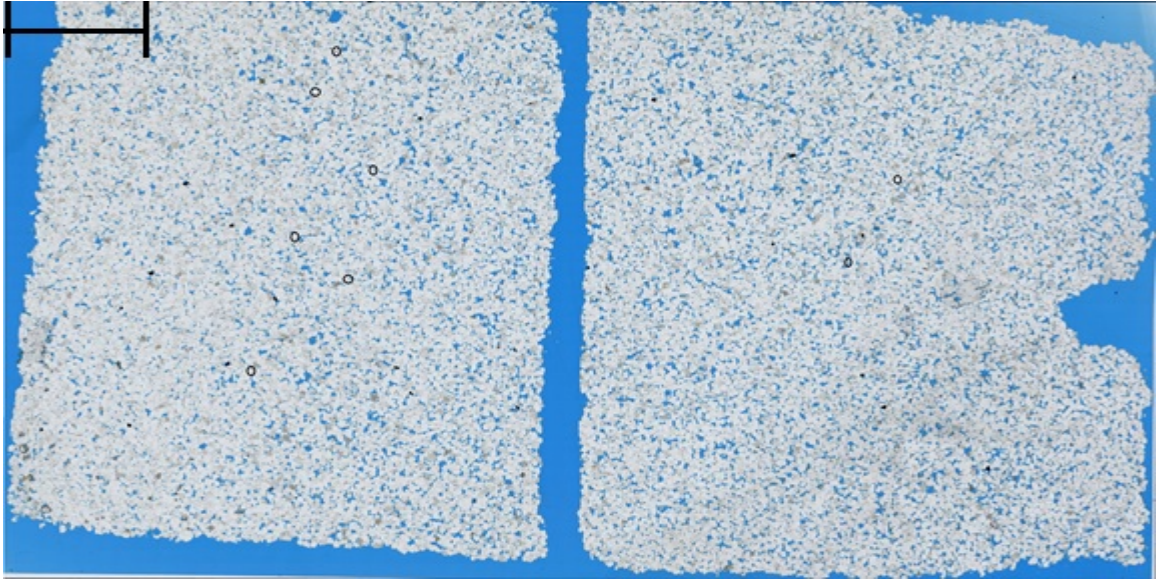


Figure 68: Post-test Fontainebleau-3.5 Sandstone thin-section. The black circles are the regions from which the tiles were selected to be analyzed. The scale bar is 0.2 inch.

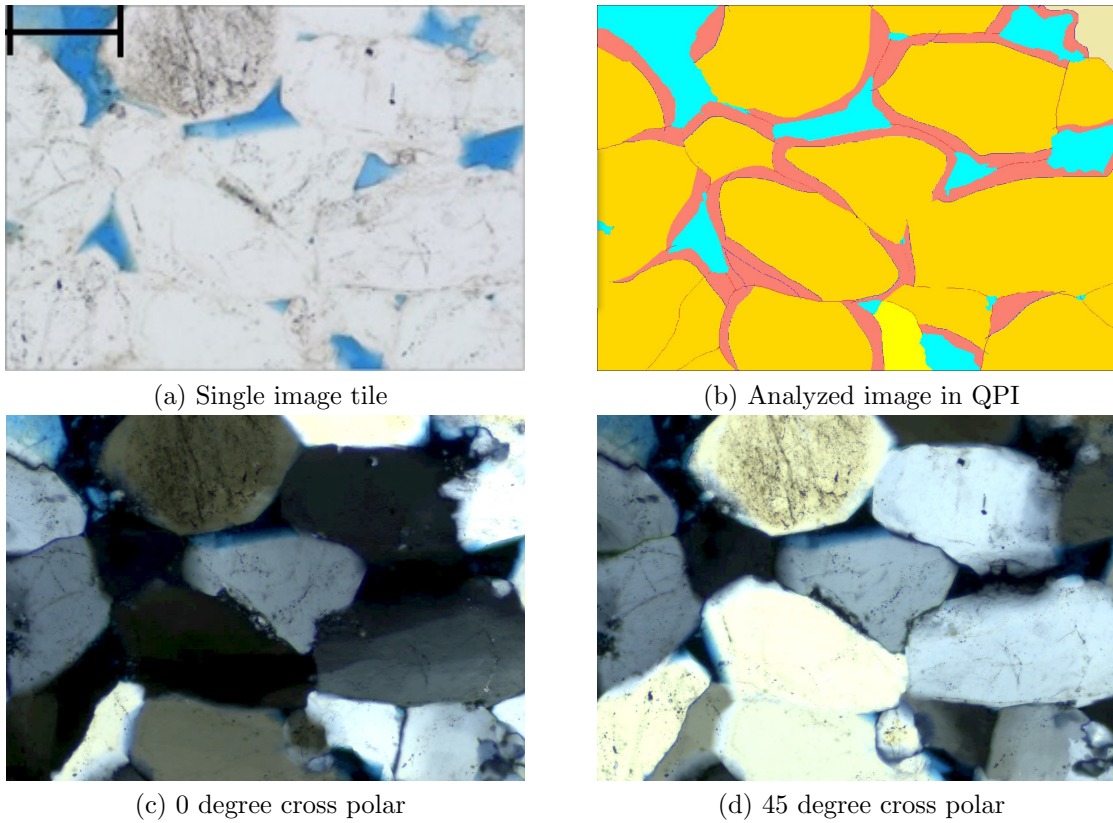


Figure 69: An analyzed image for the Fontainebleau-3.5 Sandstone sample post-test shows the segmented porosity(10%), cement volume (14%), contacts (29%) between grains, and identified framework grains. The scale bar is 200 microns.

Figure 67 shows a single image tile in transmitted light, and its analysis using the QPI software. The sample porosity is on the order of 12%, shown in blue color. The volume of cement is approximately 15%. The cements are the regions colored pink occurring as overgrowths on framework grains. The contact ratio among grains is approximately 0.27, or 27%. All the grains are mono quartz.

Figure 68 shows the full scale thin section image of post-test Fontainebleau-3.5 Sandstone. The whole thin section was not analyzed. Instead, the thin section was divided into smaller tiles, and they were analyzed until the statistics became constant as a function of the number of tiles analyzed.

Figure 69 shows a single image tile in transmitted light, and its analysis using QPI software. The segmented porosity is approximately 10%, shown in blue color. The volume of cement is approximately 15%. The cements are the regions colored pink occurring as overgrowths on framework grains. The contact ratio among grains is approximately 0.29, or 29%. All the grains are mono quartz.

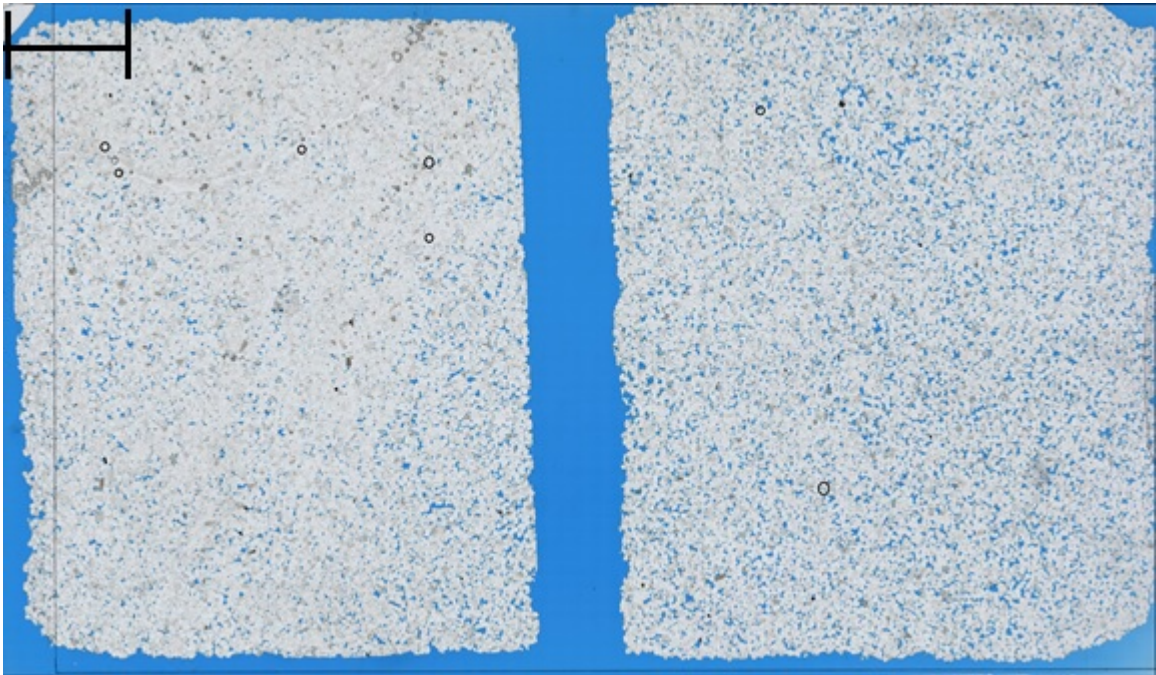


Figure 70: Post-test Fontainebleau-3.4 Sandstone thin-section. The black circles are the regions from which the tiles were selected for analysis. The scale bar is 0.2 inch.

Figure 70 shows the full scale thin section of post-test Fontainebleau-3.5 Sandstone. The whole thin section was not analyzed. Instead, the thin section was divided into smaller tiles, and they were analyzed until the statistics became constant as a function of tiles analyzed.

Figure 71 shows a single image tile in transmitted light, and its analysis using the QPI software. The segmented porosity is on the order of 9%, shown in blue color. The volume of cement is approximately 17%. The cements are the regions colored pink occurring as overgrowths on framework grains. The contact ratio among grains is approximately 0.29, or 29%. All the grains are mono quartz.

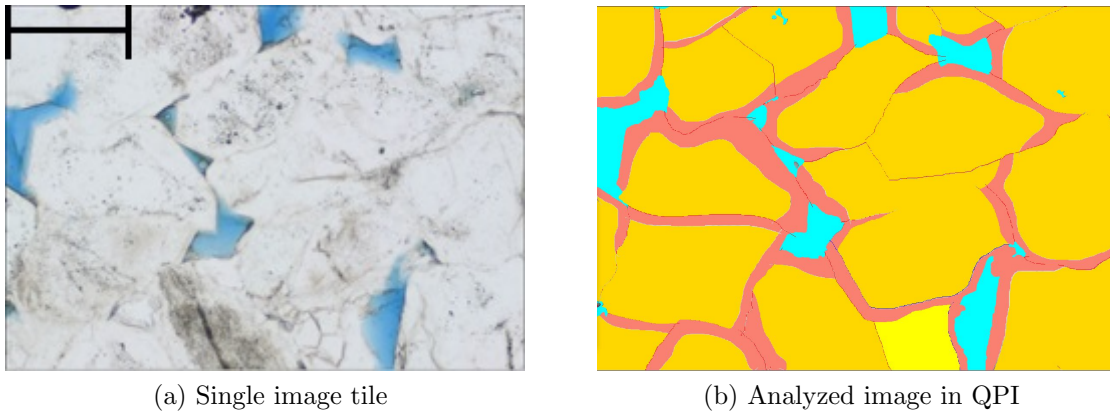


Figure 71: A sample analyzed image for the Fontainebleau-3.4 Sandstone sample post-test shows the segmented porosity (9%), volume of cement (15%), contacts between grains (40%), and identified framework grains.

Table 21 contains a summary of the sample characterization data for one pre-test and two post-test samples of the Fontainebleau-3 Sandstone sample. There is a reduction in porosity with increasing confining pressure. This is expected as porosity decreases with increasing stress. The percentage cement has remained constant. The contact ratio has increased. This is also expected as a result of increasing applied pressure and the associated decrease in porosity.

Table 21: Fontainebleau-3 Sandstone sample characterization summary.

| Sample name | Confining pressure (psi) | porosity (%) | cements (%) | Contact ratio (%) |
|-------------|--------------------------|--------------|-------------|-------------------|
| FB-Pre      | 0                        | 12           | 15          | 27                |
| FB-3-5      | 2000                     | 10           | 14          | 29                |
| FB-3-4      | 2500                     | 9            | 15          | 40                |

The cracks were counted separately by drawing them individually on each tile. The purpose was to quantify the cracks present in the samples pre-test and post-test. Specifically, we were interested in how the cracks evolve from pre-test to post-test (intermediate stress stage) and post-test (final stress stage). The protocol followed was described above in the discussion of the Fontainebleau-1 Sandstone. 30% of the tile area was examined, which was enough to generate stable statistics, as shown in figure 62. The statistics were observed to stabilize at segment 6. Examining more tiles did not change the mean number of cracks. The number of cracks was then normalized to per centimeter square area .

Table 22: Fontainebleau-3 Sandstone sample cracks summary.

| Sample name | Confining pressure | incremental cracks/cm.sq | Vertical inc. cracks/cm.sq |
|-------------|--------------------|--------------------------|----------------------------|
| FB-Pre      | 0                  | 9                        | 6                          |
| FB-3-5      | 2000               | 31                       | 20                         |
| FB-3-4      | 2500               | 59                       | 50                         |

Table 22 shows the total number of incremental cracks per centimeter squared for the Fontaine- bleau-3 pre-test and two post test samples. Incremental cracks are those cracks that are generated only at the specified stress stage. The table also contains a column for vertical cracks only. The vertical cracks were determined whose orientation was greater than 45 degree angle.

Figure 72 shows the total number of incremental vertical cracks versus end stage stress. The exponential relationship shows that cracks are being generated at a faster

rate at higher stress stage. This indicates that the sample is approaching failure.

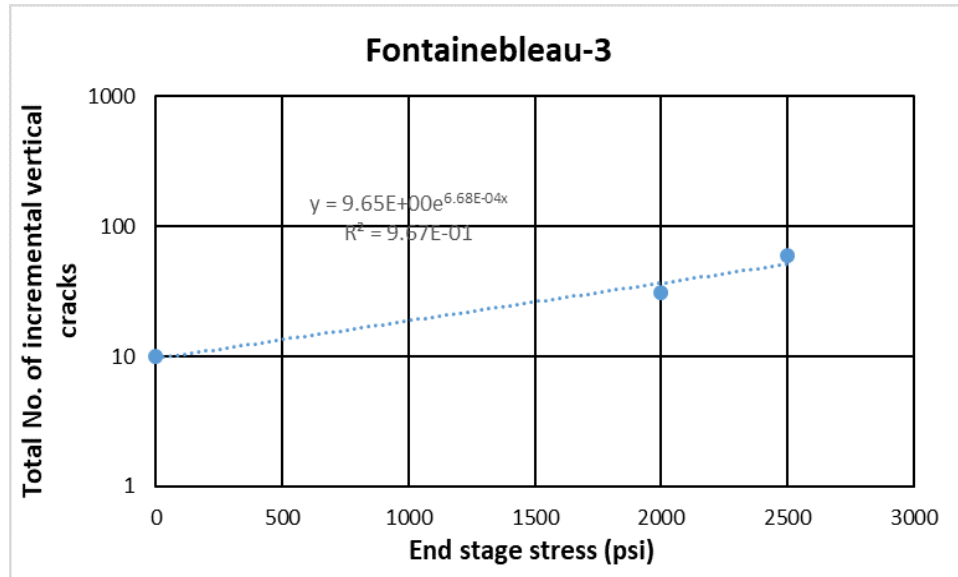


Figure 72: There is an exponential relationship between total number of cracks and the end stage stress.

### 4.3 Boise Sandstone Sample Characterization

Similar analyses were performed on Boise Sandstone samples as those performed on the Fontainebleau Sandstone samples. Figure 73 shows the full scale thin section scan of the pre-test Boise Sandstone sample. The whole thin section was not analyzed. Instead, the thin section was divided into smaller tiles, and they were analyzed until the statistics became constant as a function of the number of tiles analyzed.

Figure 74 shows a single image tile in transmitted light, and its analysis using the QPI software. The segmented porosity is on the order of 25%, shown in blue color. The volume of cement is approximately 2%. Note that in the case of the Boise Sandstone cements include clay grain coatings (principally illite) and local feldspar overgrowths. The identified cement is shown in the pink color, typically overlying as clay grain coatings. The contact ratio among grains is approximately 10%, significantly lower than for the Fontainebleau. Framework grain analysis for this image of the Boise Sandstone is approximately 38% k-feldspar, 37% quartz, 10% plagioclase

feldspar, and 3% biotite and 10% lithic fragments.

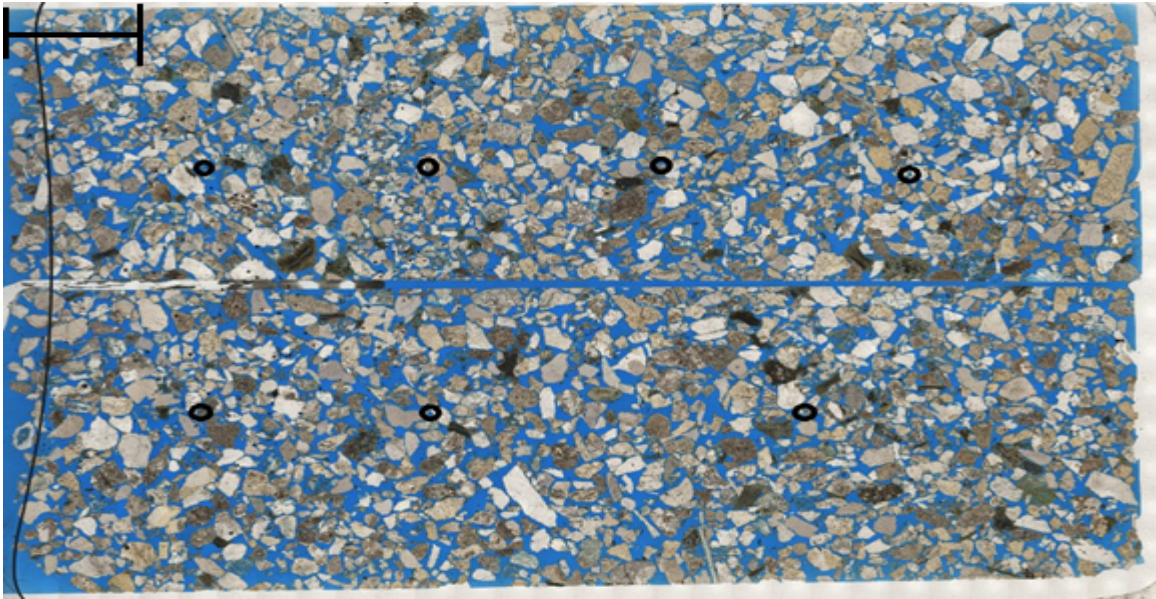
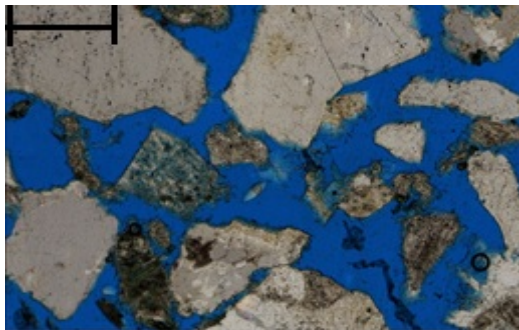
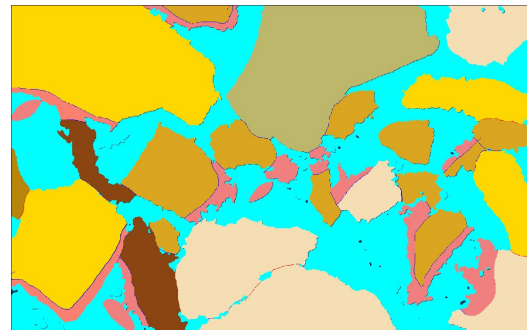


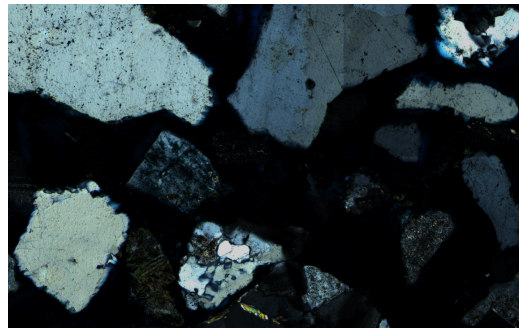
Figure 73: Pre-test Boise Sandstone thin-section. The black circles are the regions from which the tiles were selected for analysis. The scale bar is 400 microns.



(a) Single image tile



(b) Analyzed image in QPI



(c) 0 degree cross polar

Figure 74: The analyzed image for the Boise Sandstone pre-test shows the sampled porosity, percentage cement, contacts between grains, and sampled grains. The scale bar is 400 microns.

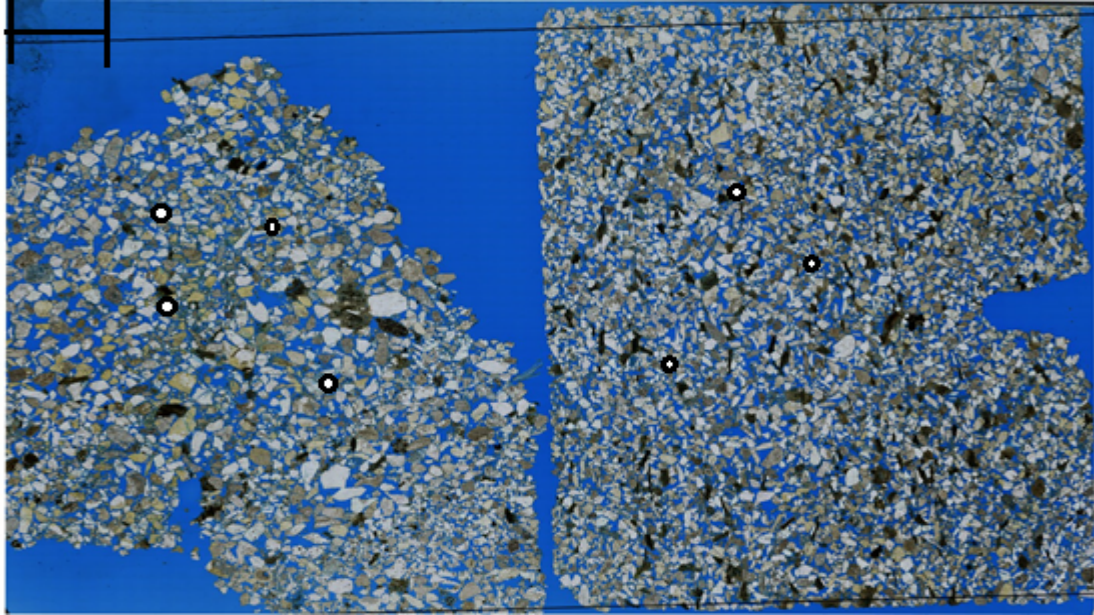


Figure 75: Post-test Boise Sandstone thin-section. The black circles are the regions from which tiles were selected for analysis. The scale bar is 0.2 inch.

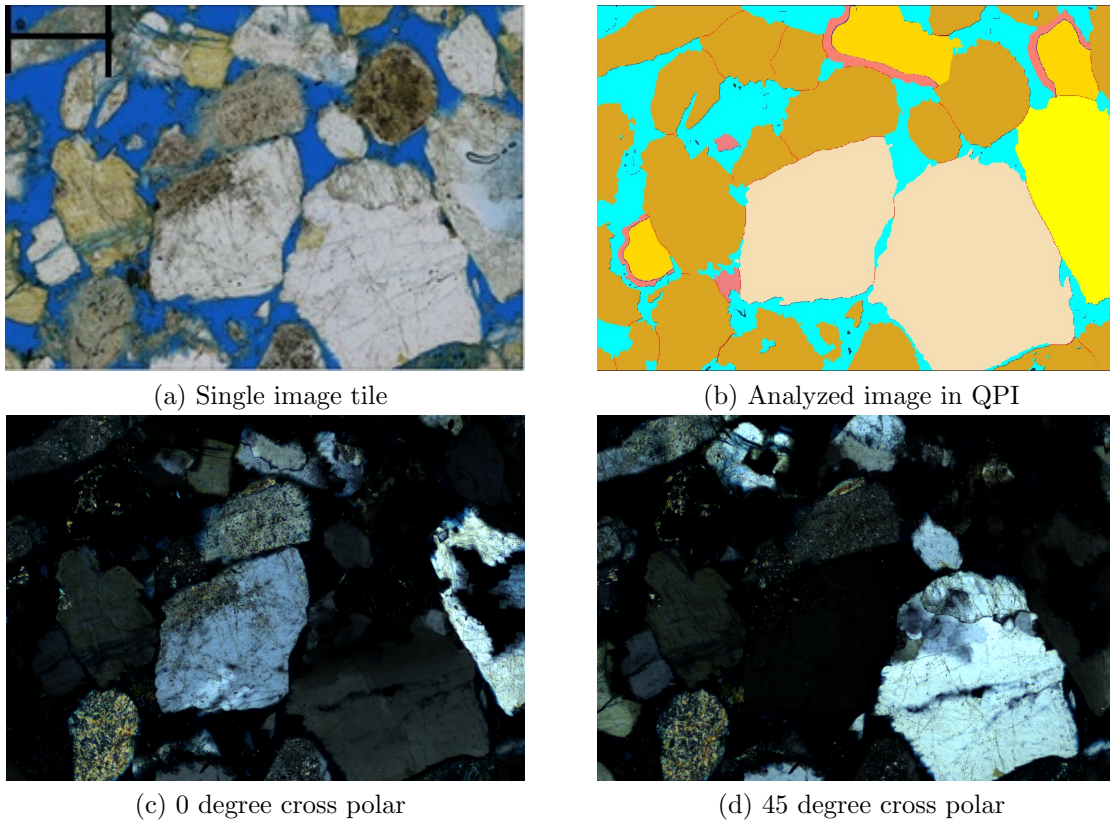


Figure 76: An analyzed image for the Boise-1.1 Sandstone sample post-test shows the segmented porosity, volume of cement, contacts among grains, and framework mineralogy.

Figure 75 shows the full scale thin section scan of a post-test Boise Sandstone sample. The whole thin section was not analyzed. Instead, the thin section was divided into smaller tiles, and they were analyzed until the statistics became constant as a function of tiles analyzed.

Figure 76 shows a single image tile in transmitted light, and its analysis using QPI software. The segmented porosity is on the order of 24%, shown in blue color. The volume of cement is approximately 2%, principally comprising clay grain coatings. The contact ratio among grains is approximately 10%. This image of the Boise Sandstone sample comprises approximately 36% k-feldspar, 37% quartz, 16% plagioclase, 4% biotite, and 10% lithic fragments.

Figure 77 shows the full scale thin section image of a post-test Boise Sandstone sample. The whole thin section was not analyzed. Instead, the thin section was divided into smaller tiles, and they were analyzed until the statistics became constant as a function of the number of tiles analyzed.

Figure 78 shows a single image tile in transmitted light, and its analysis using the QPI software. The sampled porosity is on the order of 22%, shown in blue color. The percentage cement is approximately 2%, comprising primarily illitic grain coatings. The contact ratio among grains is approximately 12%. This image of the Boise-1.2 Sandstone sample contains approximately 40% k-feldspar, 30% quartz, 16% plagioclase, 6% biotite and 5% lithic fragments .

Table 23 contains the summary of characterization data for one pre-test and two post-test samples of the Boise Sandstone. There is a reduction in porosity with increasing confining pressure. This is expected as porosity decreases with increasing stress. Both cement and contact ratio have remained approximately constant, although the contact ratio increases slightly. Table 24 shows the grain distribution. The majority of grains are k-feldspar and quartz. There is also some illite clay, plagioclase feldspar, biotite, and muscovite.

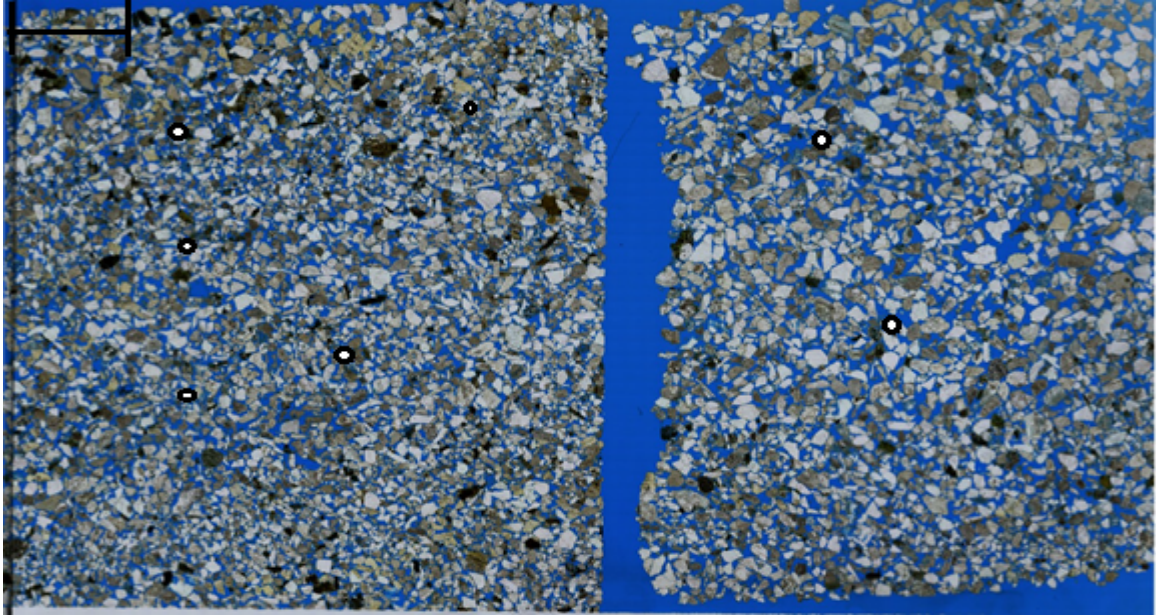
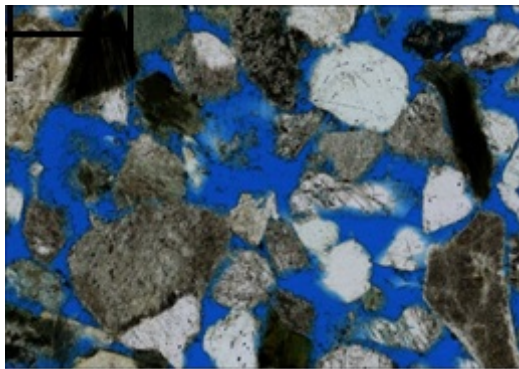
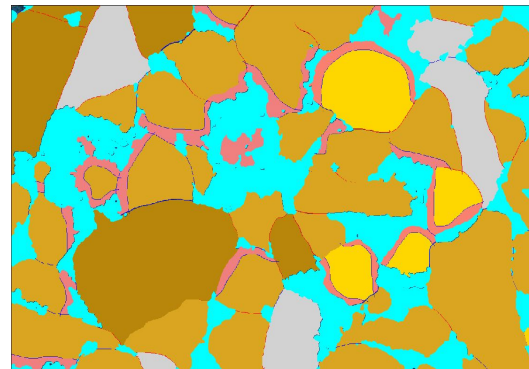


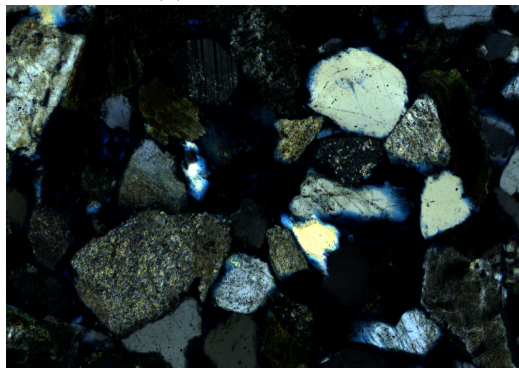
Figure 77: Scan of post-test Boise Sandstone thin-section. The black circles are the regions where tiles were selected for analysis.



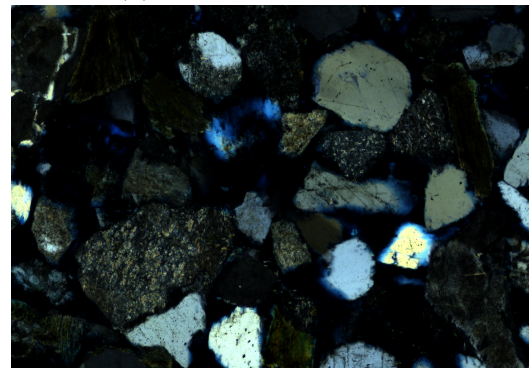
(a) Single image tile



(b) Analyzed image in QPI



(c) 0 degree cross polar



(d) 45 degree cross polar

Figure 78: An analyzed image tile for the Boise-1.2 Sandstone sample post-test illustrating the segmented porosity, volume of cement, contacts among grains, and framework grain mineralogy.

Table 23: Boise Sandstone sample characterization summary.

| Sample name | Confining pressure (psi) | porosity (%) | cements (%) | Contact ratio (%) |
|-------------|--------------------------|--------------|-------------|-------------------|
| BSE-Pre     | 0                        | 25           | 2           | 10                |
| BSE-1-1     | 2000                     | 24           | 2           | 10                |
| BSE-1-2     | 3000                     | 22           | 1           | 11                |

Table 24: Boise Sandstone framework grain characterization summary.

| Sample name | K-spar (%) | Quartz (%) | Plagioclase (%) | Biotite (%) | Lithic fragments (%) | Illite clay (%) |
|-------------|------------|------------|-----------------|-------------|----------------------|-----------------|
| BSE-Pre     | 38         | 37         | 10              | 2           | 10                   | 3               |
| BSE-1-1     | 36         | 37         | 10              | 4           | 10                   | 2               |
| BSE-1-2     | 40         | 30         | 16              | 6           | 5                    | 3               |

The cracks were counted separately by drawing them individually on each tile. The purpose was to quantify the cracks pre-test and post-test. Specifically, how the cracks evolve from pre-test to post-test (intermediate stress stage) and post-test (final stress stage). The protocol followed was similar to that for the Fontainebleau Sandstone. On average, 30% of the tile area was examined, which was sufficient for statistical analyses to become stable, as shown in figure 62. Statistics stabilized after the analysis of 6 image tiles. Examining more slides did not change the mean number of cracks. The number of cracks was then normalized to per centimeter square area.

Table 25: Boise Sandstone sample cracks summary.

| Sample name | Confining pressure | incremental cracks/cm.sq | Vertical inc. cracks/cm.sq |
|-------------|--------------------|--------------------------|----------------------------|
| BSE-Pre     | 0                  | 7                        | 4                          |
| BSE-1-1     | 2000               | 17                       | 14                         |
| BSE-1-2     | 3000               | 68                       | 55                         |

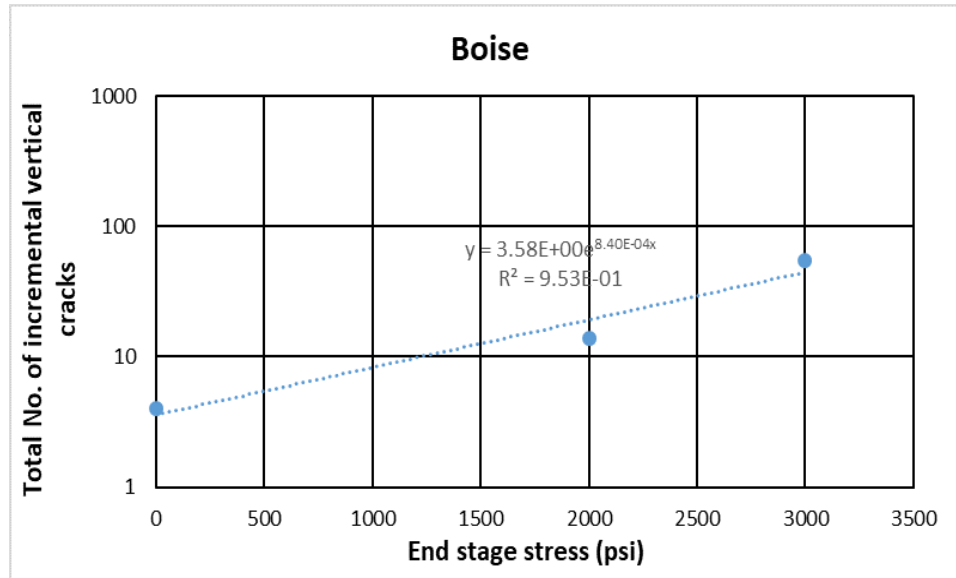


Figure 79: There is an exponential relationship between the total number of cracks and stress at each stage.

Table 25 shows the total number of incremental cracks per centimeter square for Boise Sandstone pre-test and two post test samples. Incremental cracks are those cracks that are generated only at the specified stress stage. The table also contains a column for vertical cracks only. The vertical cracks were identified as those orientation was greater than 45 degree angle.

Figure 79 shows the total number of incremental vertical cracks versus end stage stress. The exponential relationship shows that the cracks are being generated faster at higher stress stages, indicating that the sample is approaching failure.

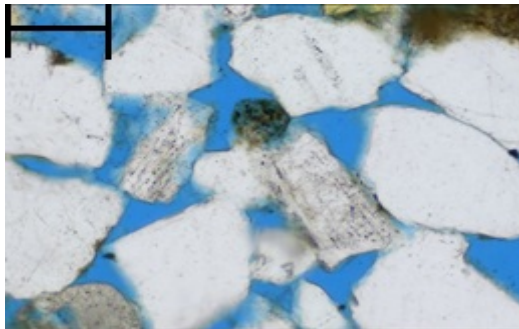
#### 4.4 Miocene sandstone

MST tests were performed on two Miocene sandstone samples. One sample was unloaded at a strain ratio of 0.5, while the second at a strain ratio of 0.3. The purpose was to see the difference in damage as a function of the point selected for unloading. The image analysis methodology is as previously described. One pre-test Miocene sandstone thin section and two post-test Miocene sandstone thin sections

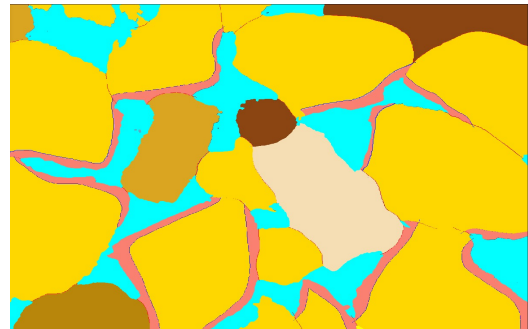
were analyzed, and the results compared.



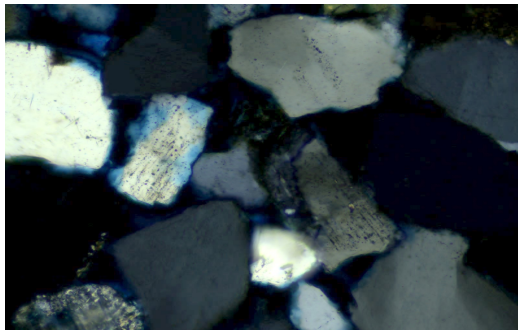
Figure 80: Pre-test Miocene sandstone thin-section. The black circles are the regions from which tiles were selected for analysis.



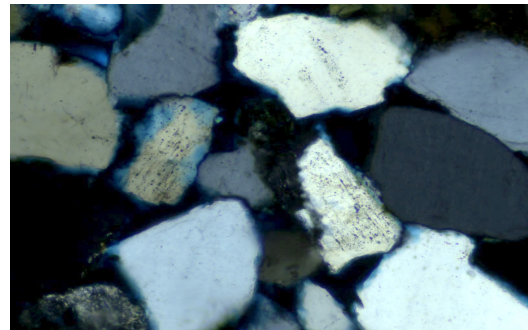
(a) Single image tile



(b) Analyzed image in QPI



(c) 0 degree cross polar



(d) 45 degree cross polar

Figure 81: The analyzed image for Miocene sandstone pre-test shows the segmented porosity, volume of cement, contacts among grains, and framework grain mineralogy.

Figure 80 shows the full scale thin section scan of the pre-test Miocene sandstone. The whole thin section was not analyzed. Instead, the thin section was divided into smaller tiles, and they were analyzed until the statistics became constant as a function of the number of tiles analyzed.

Figure 81 shows a single image tile in transmitted light, and its analysis using QPI software. The segmented porosity is approximately 20%, shown in blue color. The volume of cement is approximately 7%. All of the identified cements are present as quartz overgrowths. The contact ratio among grains is on the order of 15%. The Miocene sandstone framework grain composition is given by: 20% feldspar, 70% quartz, 3% plagioclase, 2% illite clay, and 2% shale clast.

Figure 82 shows the full scale thin section of post-test Miocene sandstone. The whole thin section was not analyzed. Instead, the thin section was divided into smaller tiles, and they were analyzed until the statistics became constant as a function of tiles analyzed.

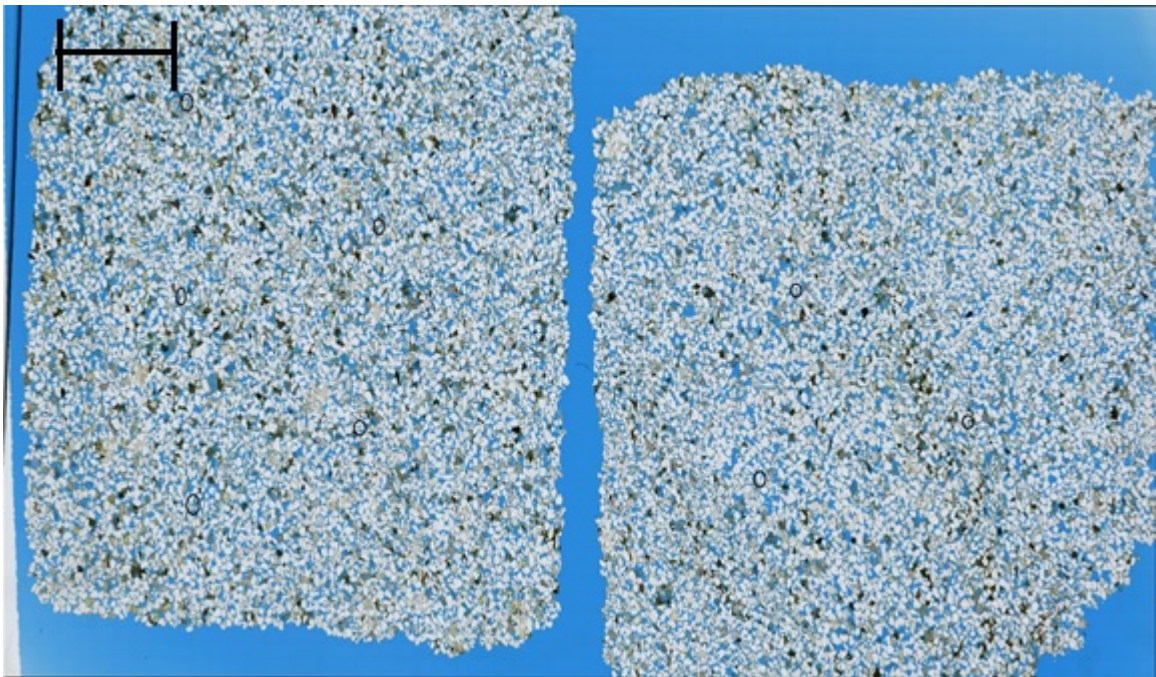


Figure 82: Post-test Miocene sandstone thin-section. The black circles are the regions from which tiles were selected for analysis.

Figure 83 shows a single image tile in transmitted light, and its analysis using the QPI software. The sampled porosity is on the order of 19%, shown in blue color. The volume of cement is approximately 6%. All of the identified cements are present as quartz overgrowths. The contact ratio among grains is approximately 17%. This Miocene sandstone sample has a framework mineralogy including: 15% feldspar, 71% quartz, 2% illite clay, 2% shale clasts and 10% plagioclase.

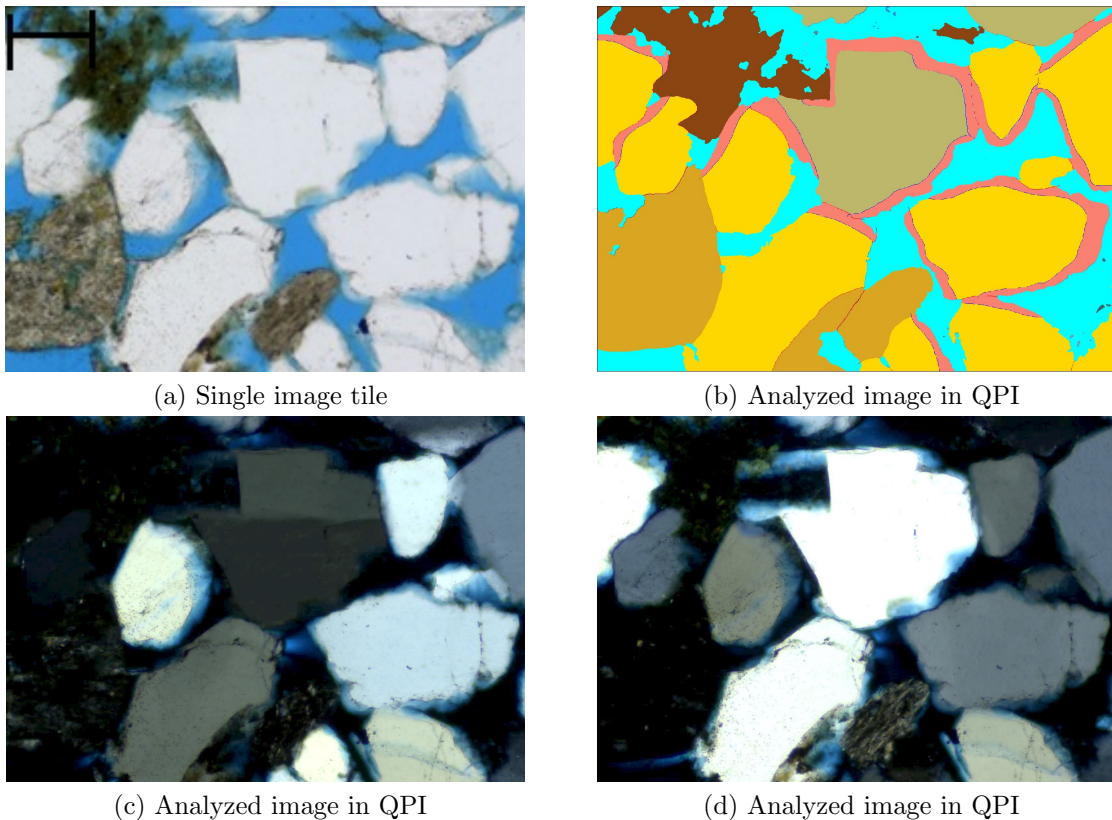


Figure 83: The analyzed image for Miocene sandstone post-test shows the segmented porosity, volume of cement, contacts among grains, and the framework grain mineralogy.

Figure 84 shows the full scale thin section of the post-test Miocene-3 sandstone. The whole thin section was not analyzed. Instead, the thin section was divided into smaller tiles. Additional tiles were analyzed until the statistics became constant as a function of the number of tiles analyzed.

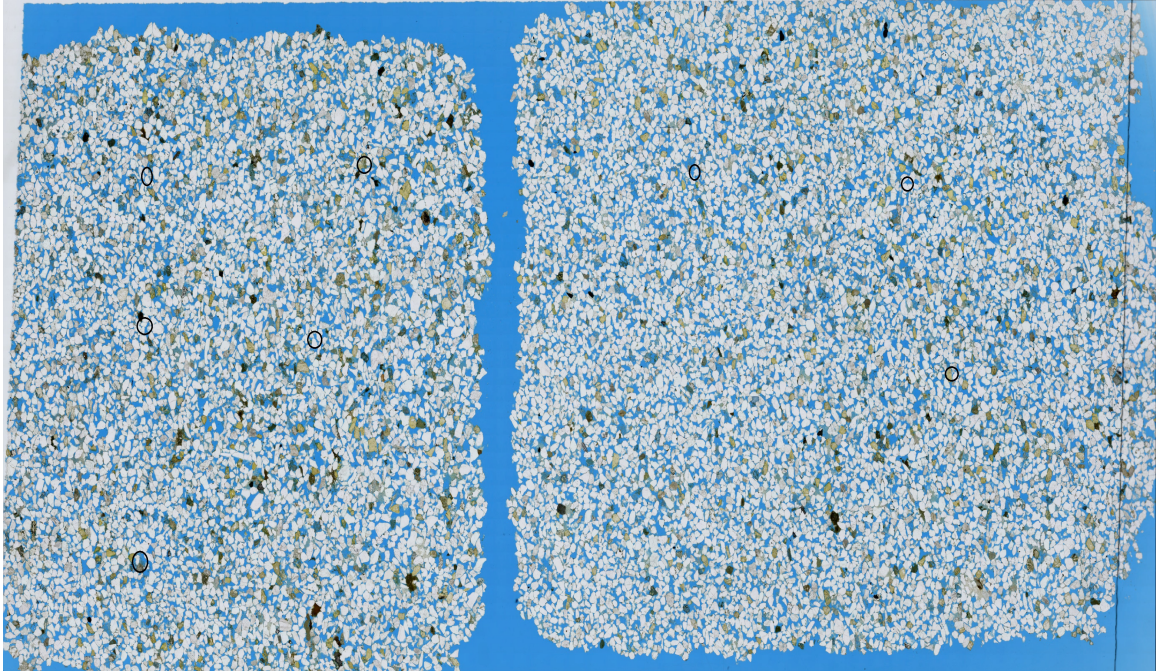
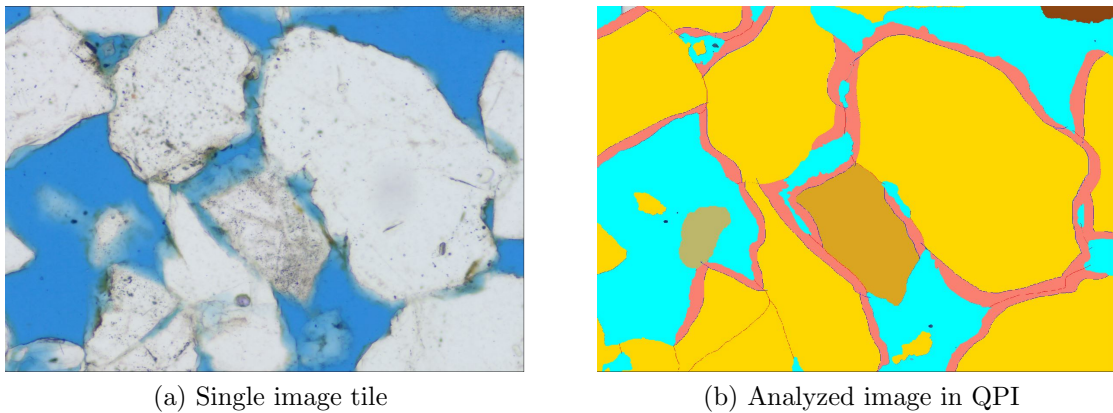


Figure 84: Post-test Miocene-3 sandstone thin-section. The black circle is the region from where the tiles were selected to be analyzed.



(a) Single image tile

(b) Analyzed image in QPI

Figure 85: An analyzed image tile for the Miocene-3 sandstone sample post-test shows the segmented porosity, volume of cement, contacts among grains, and the framework mineralogy.

Figure 85 shows a single image tile in transmitted light, and its analysis using the QPI software. The sampled porosity is approximately 22%, shown in blue color. The volume of cement is approximately 6%. All identified cement is quartz overgrowth. The contact ratio among grains is on the order of 14%. The framework mineralogy of this Miocene sandstone sample is: 15% feldspar, 5% quartz, 5% illite clay, 3% shale

clasts and 5% plagioclase.

Table 26 contains the summary of the characterization data for one pre-test and two post-test samples of the Miocene sandstone. There is a reduction in porosity with increasing confining pressure. Porosity has reduced just 1% for unloading at a strain ratio of 0.5. For a strain ratio of 0.3, the porosity is higher. This is likely due to differences resulting from sample twinning. Cement volumes remain constant As expected. The contact ratio has increased for the Miocene-1 sandstone sample. This is expected as contacts increase at higher stress. For Miocene-3 sandstone, the contact ratio has slightly decreased. Once again, this is likely due to differences resulting from sample twinning, although the lower strain ratio at the unloading point may also have influenced this number. Table 27 shows a summary of the framework grain mineralogy. The majority of grains are feldspar and quartz. There are also some clay clasts and chert.

Table 26: Miocene sandstone sample characterization summary.

| Sample name | Unload strain ratio | porosity (%) | cements (%) | Contact ratio (%) |
|-------------|---------------------|--------------|-------------|-------------------|
| MSE-Pre     | NA                  | 20           | 7           | 15                |
| MSE-1       | 0.5                 | 19           | 6           | 17                |
| MSE-3       | 0.3                 | 22           | 8           | 14                |

Table 27: Miocene sandstone grains characterization summary.

| Sample name | K-spar (%) | Quartz (%) | Chert (%) | Illite clay (%) | Plagioclase (%) | shale clast (%) |
|-------------|------------|------------|-----------|-----------------|-----------------|-----------------|
| MSE-Pre     | 20         | 70         | 3         | 2               | 5               | 2               |
| MSE-1       | 15         | 71         | 0         | 2               | 10              | 2               |
| MSE-3       | 15         | 75         | 2         | 5               | 5               | 3               |

The cracks were counted separately by drawing them individually on each tile. The purpose was to quantify the evolution of the number of cracks as a function of stress. The protocol followed was similar to that described above for the Fontainebleau

Sandstone. 30% of the tile area was examined, which was sufficient to generate robust statistics, as shown in figure. 62. The number of normalized cracks stabilized after 6 image tiles were analyzed. Examining more tiles did not change the mean number of cracks. The number of cracks was then normalized to per centimeter square area. Table 28 shows a summary of the Miocene sandstone sample cracks analysis.

Table 28: Miocene sandstone sample cracks summary.

| Sample name | Unload strain ratio | incremental cracks/cm.sq | Vertical inc. cracks/cm.sq |
|-------------|---------------------|--------------------------|----------------------------|
| MSE-Pre     | NA                  | 22                       | 15                         |
| MSE-1       | 0.5                 | 130                      | 81                         |
| MSE-3       | 0.3                 | 66                       | 38                         |

Miocene-1 sandstone sample has more cracks as compared to the Miocene-3 sandstone sample. This results from the change in the point selected for unloading. Unloading at a strain ratio of 0.5 induces more damage to the sample than unloading at a strain ration of 0.3.

## 4.5 Characterization Discussion

Analysis of cracks pre-test and post-test show that the number of cracks increases exponentially as a function of intermediate and final stress stage. This is consistent with our model base case assumption of the exponential distribution. The result is also consistent with the exponential distribution of acoustic emissions observed by Parkash et al. (2017).

In the introduction chapter, we have discussed that one of the main reasons for the difference between static and dynamic properties is that the dynamic properties are highly dependent on contacts among grains whereas cements impact the compressive strength. Figure 86 shows a plot of  $M_1$  vs Contact ratio. In section 2.3.2 we have discussed that  $M_1$  is the velocity (dynamic) measurement. The plot in figure 86 shows

that the dynamic data is directly proportional to the contact ratio among grains for different rock types.

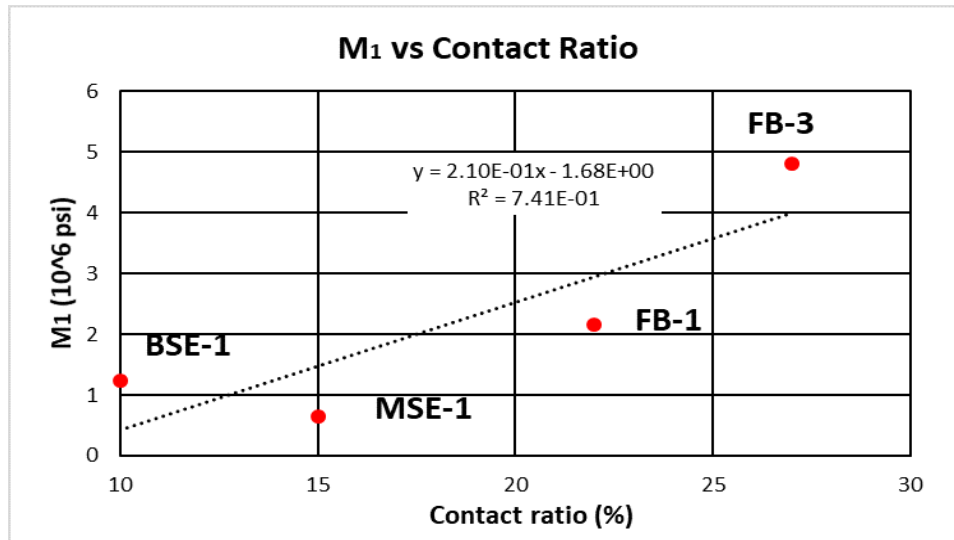


Figure 86:  $M_1$  (dynamic data) vs contact ratio for different rock types. There is a linear relationship between  $M_1$  and contact ratio.

Figure 87 is plot of maximum compressive strength (static data) vs percentage cements. The plot shows that there is a direct linear relationship between the static data and percentage cement.

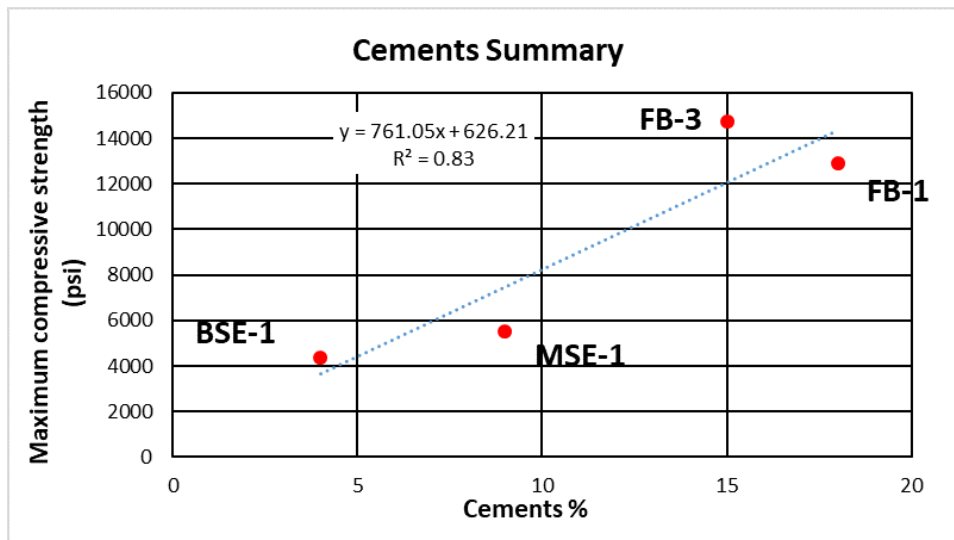


Figure 87: Maximum compressive strength (static data) vs. percentage cement for different rock types. There is a linear relationship between strength and cement volume.

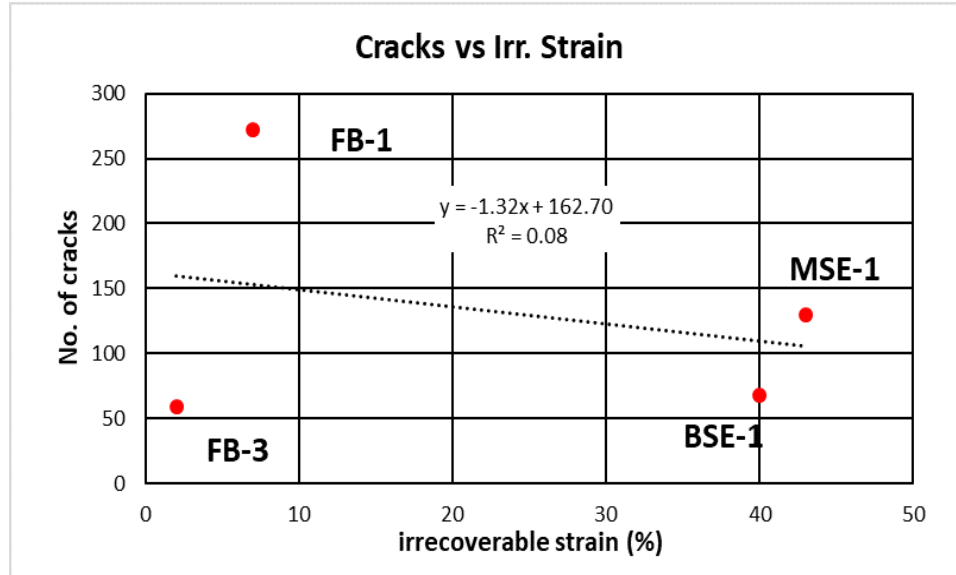


Figure 88: Total no. of cracks generated vs irrecoverable strains. There is no correlation between the number of cracks generated and the percent irrecoverable strain.

We have discussed in detail that the physical mechanism that controls  $M_1$  is acoustic velocity measurements. The non-linear elastic term  $M_2$  has been correlated to irrecoverable strains. Figure 88 is a plot of the total number of cracks generated post test vs. percent irrecoverable strains. There is no correlation between the number of cracks generated and the percent irrecoverable strains. We then normalized the cracks generated to the maximum deviatoric stress that the sample experienced during testing. The samples that have experienced higher deviatoric stress generate more cracks. Normalizing the number of cracks generated to the maximum deviatoric stress allows us to compare the cracks generated at similar stress conditions as a function of percent irrecoverable strain. Figure 89 is a plot of the total number of cracks generated normalized to the maximum shear stress. The correlation is substantially improved. A higher number of cracks generated results in higher irrecoverable strains.

The next step is to include the influence of porosity on the number of cracks generated and irrecoverable strain. A lower porosity sample is expected to have more cracks than as compared to a higher porosity sample. In a higher porosity sample, the grains have more room to shift and turn instead of getting crushed, which is the

case for a lower porosity sample. Figure 90 is the updated plot of the total number of cracks generated normalized to maximum deviatoric stress and porosity versus irrecoverable strains. The relationship is quite good now. For higher irrecoverable strains, the number of generated cracks are higher.

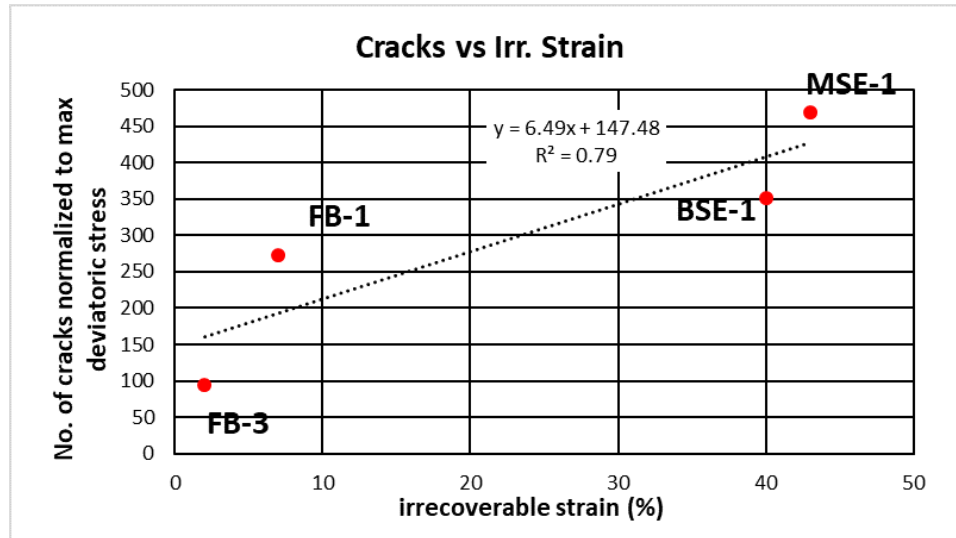


Figure 89: Total number. of cracks generated, normalized to maximum shear stress vs. irrecoverable strains. There is an improved correlation between the number of cracks generated and percent irrecoverable strains. The higher the number of normalized cracks generated the larger the irrecoverable strains.

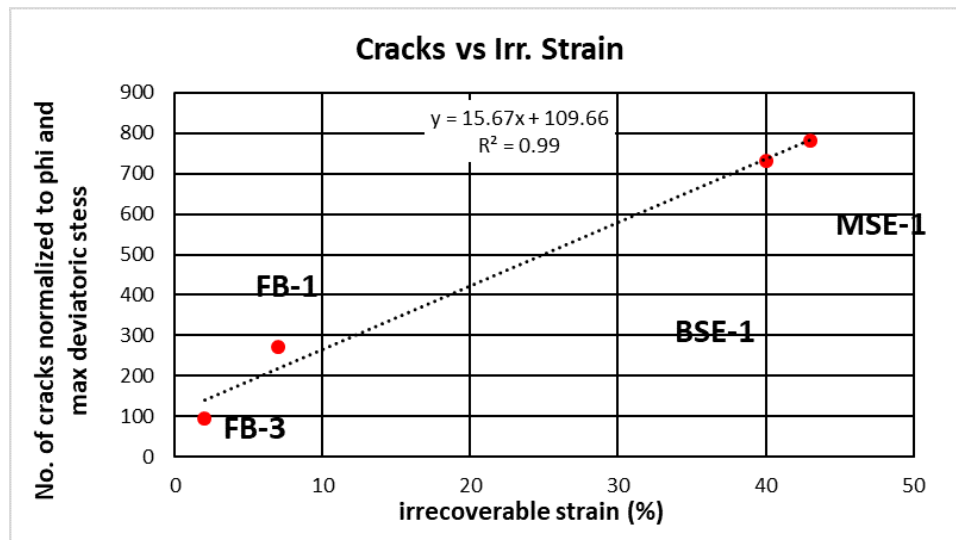


Figure 90: Total no. of cracks generated, normalized to maximum deviatoric stress and porosity vs. irrecoverable strains. There is an excellent correlation between the normalized number of cracks generated and percent irrecoverable strains.

The result in figure 90 establishes that irrecoverable strains are controlled by the number of cracks generated, once we account for the change in porosity and the maximum deviatoric stress applied. This provides us some intuition into the physical mechanisms that controls irrecoverable strains. We have previously established that  $M_2$  (hypermodulus) is related to irrecoverable strains. This means that the number of cracks generated should also correlate with  $M_2$ . Figure 91 is plot of the absolute value of  $M_2$  versus the normalized number of cracks. A higher number of normalized cracks corresponds to a higher value of  $M_2$  and a larger percent of irrecoverable strains.

The next step is to analyze how pre-test sample characterization parameters influence the number of cracks generated. This helps in predicting  $M_2$  directly from pre-test sample parameters.

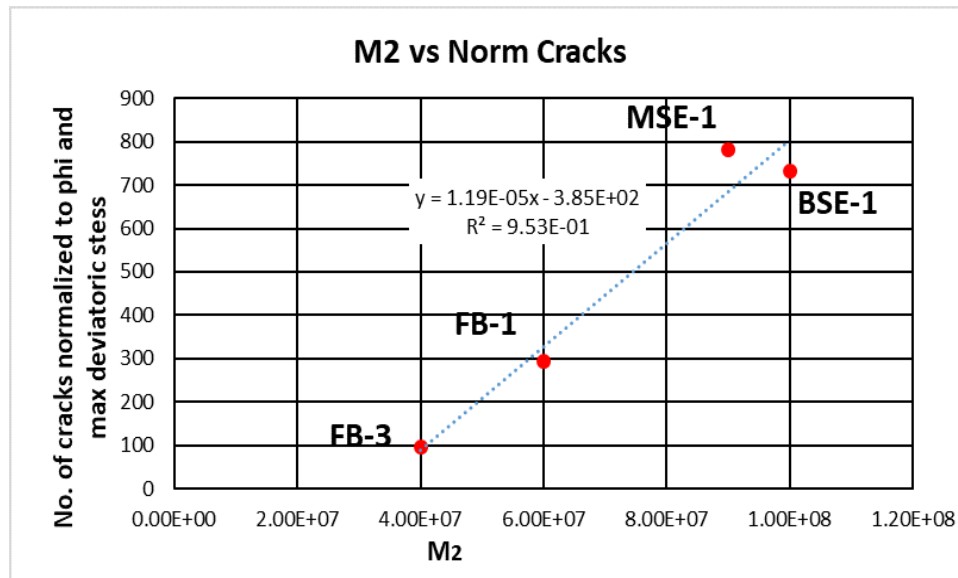


Figure 91: Total number of cracks generated, normalized to maximum deviatoric stress and porosity vs  $M_2$ . A higher number of cracks generated corresponds to higher irrecoverable strains.

Figure 92 is a plot of the absolute value of  $M_2$  versus the volumes of porosity and cements. There is a direct linear relationship between  $M_2$  and porosity. This is expected as increasing porosity should result in higher irrecoverable strains. This translates into a higher  $M_2$  value. Conversely, higher cement results in lower irrecov-

erable strains and lower  $M_2$ .

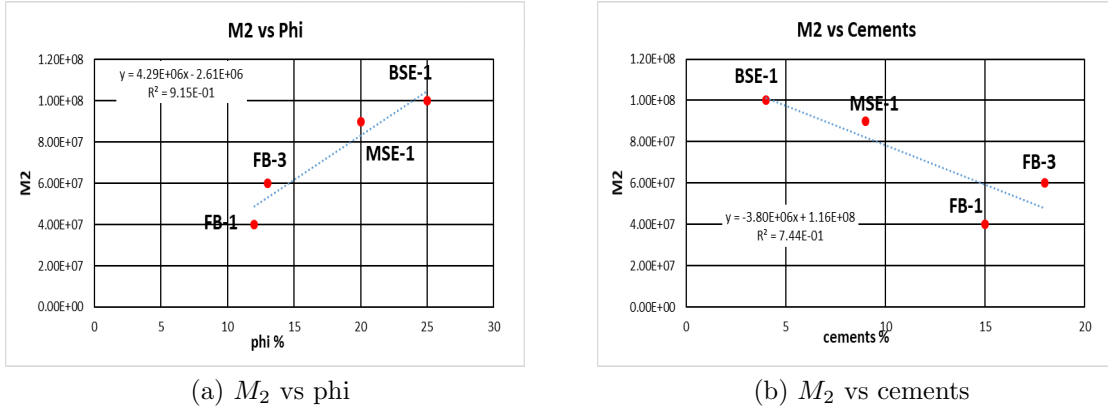


Figure 92:  $M_2$  increases with increasing porosity and increases with decreasing cement volume. This is expected as higher porosity should be related to higher irrecoverable strains, and a higher  $M_2$ . Higher cement results in lower irrecoverable strains and lower  $M_2$ .

value. The correlation coefficients between  $M_2$  vs cements and  $M_2$  vs porosity are 0.74 and 0.88. The next step is to regress  $M_2$  with cements and porosity together and see if a better correlation can be achieved.  $M_2$  can be written in term of porosity and cements as

$$M_2 = 1.07E7\phi + 6.9E6cmnt - 1.91E8. \quad (33)$$

Where  $\phi$  is porosity and  $cmnt$  is cements, both in percentage. The correlation coefficient for equation 33 is 0.98. This correlation factor is much better than the individual correlation factors of 0.88 and 0.74 between  $M_2$  and cements and between  $M_2$  and porosity respectively. Figure 93 is a plot showing the comparison between measured and predicted  $M_2$  as a function of cements and porosity.  $M_2$  is predicted using equation 33.

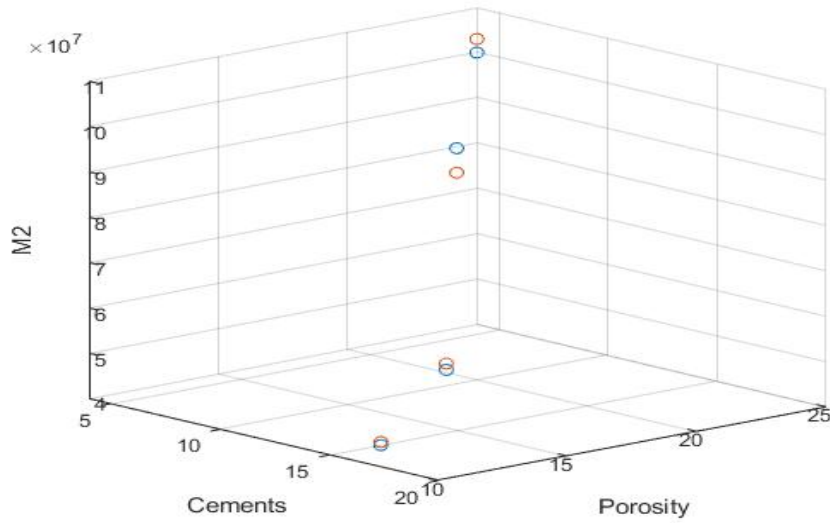


Figure 93: Comparison of original and predicted  $M_2$  as a function of cements and porosity. The blue points are the raw data and red points are predicted data. Equation 33 fits the data very well.

Figure 94 contains two plots of comparison between measured and predicted  $M_2$  as a function of cements and porosity.  $M_2$  is predicted using equation 33. The predicted data fits the original data quite well.

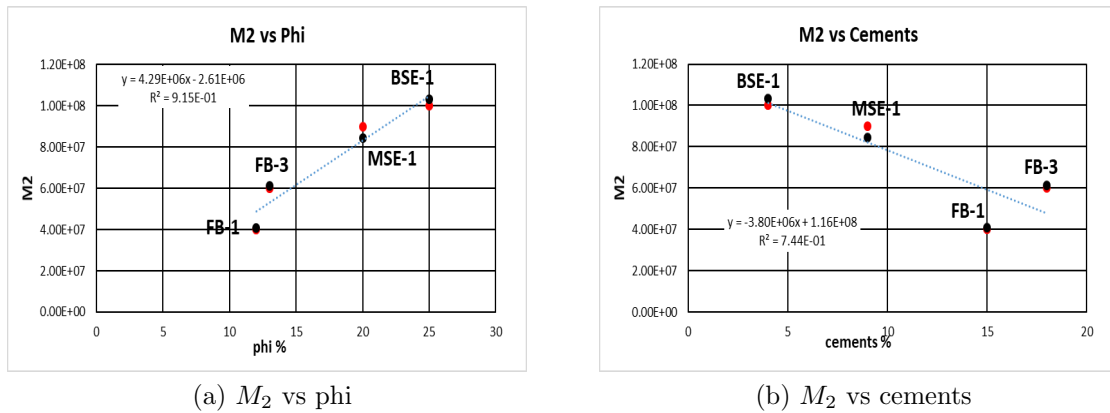


Figure 94: Comparison of original and predicted  $M_2$  as a function of cements and porosity on 2D plots. The red points are the raw data and blue points are predicted data.

The above discussion gives some intuition into the physical mechanisms that control the modeling parameters,  $M_1$  and  $M_2$ .  $M_1$  depends on the contact ratio, and  $M_2$  is controlled by the generation of cracks. The cracks depend on the amount of cement

and sample porosity. We have not quantified the effects of mineralogy. Mineralogy will also have effects on the modeling parameters, especially on the compaction model parameters  $(\eta_o, k_d, k_m)$  for plastic strains. Mineralogy will also control the creation of cracks. We need the modified compaction model to predict irrecoverable strains for samples having irrecoverable strains greater than 7%. The Fontainebleau Sandstone and equally elastic materials will not need this correction. The triaxial test data can simply be predicted using  $M_1$  and  $M_2$ . Historically, the compaction model parameters  $(\eta_o, k_d, k_m)$  have been obtained by calibrating the model to a base case. Future work will involve testing additional samples having irrecoverable strains greater than 7%. Sufficient data will then be available to include the effects of mineralogy on the non-linear elastic parameter and compaction model parameters. Table 29 is the summary plot of modeling parameters for all the samples.

Table 29: Modeling parameters for every sample.

|                | $M_1$    | $M_2$     | $\eta_o$ | $k_d$ | $k_m$ |
|----------------|----------|-----------|----------|-------|-------|
| Castlegate     | 1.50E+06 | -5.30E+07 | 1.06E-04 | 512   | -633  |
| Austin chalk   | 1.70E+06 | -1.04E+08 | 3.11E-03 | 606   | -943  |
| Austin Chalk-2 | 1.67E+06 | -7.00E+07 | 4.22E-04 | 1000  | -1100 |
| Miocene-2      | 1.10E+06 | -2.20E+07 | 7.86E-05 | 313   | -210  |
| BSE-1          | 1.24E+06 | -8.00E+07 | 5.05E-04 | 115   | -505  |
| BSE-2          | 1.40E+06 | -1.00E+08 | 2.15E-04 | 114   | -200  |
| Miocene-1      | 6.50E+06 | -9.00E+07 | 4.69E-05 | 240   | -195  |
| FB-1.9-500mD   | 3.74E+06 | -6.00E+07 | NA       |       |       |
| FB-1.10-500mD  | 2.16E+06 | -5.50E+07 |          |       |       |
| FB-3.5-1.1md   | 4.80E+06 | -4.00E+07 |          |       |       |
| FB-3.4-1.1md   | 4.15E+06 | -3.40E+07 |          |       |       |
| Berea          | 2.22E+06 | -4.20E+07 |          |       |       |

# Chapter 5: Conclusions and Future work

## 5.1 Conclusions

1. A delineation of the separate mechanisms i.e. linear versus nonlinear effects in the static elastic moduli has been documented using post-test sample characterization.
2. A polynomial fit truncated at the quadratic term is fit up to the point of maximum curvature. The rest of the data, not captured by the fit, is interpreted as plastic strains.
3.  $M_1$  is equal to the modulus obtained from velocity data at small strains, and  $M_2$  (hypermodulus) correlates with the total percent irrecoverable strains.
4. The number of cracks generated is an exponential function of the confining stress stage.
5. The number of cracks generated, normalized to the maximum deviatoric stress and scaled to porosity, is related to irrecoverable strains and therefore  $M_2$ .
6.  $M_2$  correlates with both porosity and cement volume.
7. A compaction model has been applied to predict plastic strains. The model has three parameters,  $k_d$ ,  $k_m$ , and  $\eta_o$ , which can be calibrated by running a multistage triaxial test.

## 5.2 Future Work

In the previous sections, we have documented that our model can be calibrated by running an MST test on a sample of the formation of interest. The model can then directly predict a triaxial test or the stress-strain behavior along any other stress

path. We have validated the prediction for a triaxial stress path. We now need to validate prediction for other stress paths by running tests along different stress paths and comparing the model predictions. Future work will also involve modeling radial strains. Plastic strains have been modeled assuming linear behavior of the compaction model (Myers, and Hathon 2014). The linear model does not predict sample failure, so nonlinear modeling should be performed for irrecoverable strains to predict sample failure.

In its current form, the compaction model parameters ( $\eta_o$ ,  $k_d$ ,  $k_m$ ) have been obtained by calibrating the model to a base case. Future work will involve running additional samples that have irrecoverable strains higher than 7%. This should result in sufficient data to understand the influence of framework mineralogy on the compaction model parameters.

## References

- [1] A Taheri, K Tani. "Proposal of a new Multiple-Step loading Triaxial Compression Testing Method" *ISRM International Symposium*,2008.
- [2] Al-Salman, M.E, Myers M.T. Aldin M. "Comparison of Multi-Stage to Single-Stage Tri-Axial test" *ARMA conference*,2015.
- [3] Al-Tahini, Shondergeld, Rai. "The effect of cementation on the mechanical properties of sandstones" *SPE journal paper*,2006.
- [4] ASTM D7012-14e1 Standard Test Methods for Compressive Strength and Elastic Moduli of Intact Rock Core Specimens under Varying States of Stress and Temperatures" *ASTM International, West Conshohocken*,2014.
- [5] Berryman, J.G. "The effect of cementation on the mechanical properties of sandstones" *Confirmation of Biot's theory," Applied Physical letters (1980), Vol. 37(4), 382-384.*
- [6] Berryman, J.G. "Long wavelength propagation in composite elastic media: 1. Spherical inclusions, 2 Ellipsoidal Inclusions" *Journal of the Acoustical society of America (1980). 1809-1831.*
- [7] Bilal, Myers, Hathon A . "An investigation of static and dynamic data using multistage triaxial tests" *Arma 2016.*
- [8] Biot, M.A. "Theory of propagation of elastic waves in a fluid saturated porous solid: 1. Low frequency range, 2. High frequency range" *Journal of the Acoustical society of America. (1956), Vol.28(2), 168-191.*
- [9] Birch, F. "The velocity of compressional waves in rocks to 10 kilobars" *Part 2.J. Geophys. Res., 66, 2199-2224.*

- [10] Beer, F, Johnston, R, Dewolf, J, and Mazurek, D. "Mechanics of materials" *New York McGraw-Hill companies*.
- [11] Cheng, C.H. and Toksoz, M.N. "Inversion of Seismic velocities for the pore aspect ratio spectrum of a rock" *Journal of Geophysical research (1979), Vol. 84, 7533-7543*.
- [12] Coyner, K. and Cheng, C.H. "New laboratory measurement of seismic velocities on Porous rocks" *paper RP6 presented at the 1984 SEG annual meeting, Atlanta, December 2-6*.
- [13] Drucker DC, Prager W. "Soil mechanics and plastic analysis or limit design" *Appl Math 10:157-165, 1952*.
- [14] David, E and Zimmerman, R.W. "Sliding crack model for the uniaxial compression of rock" *ARMA, 2007*.
- [15] Edimann, K., Somerville, A. "Predicting rock mechanical properties from wire-line porosities" *SPE conference paper*.
- [16] Domenico, S.N. "Elastic Properties of Unconsolidated Porous Sand Reservoirs" *Geophysics (1977), Vol. 42(7), 1339-1368*.
- [17] Eissa, E.A and Kazi, A. "Relation between static and dynamic Young's moduli of rocks, International Journal of Rock Mechanics and Mining Sciences and Geomechanics Abstracts" *Volume 25, Issue 6, 1988, ages 479-482, ISSN 0148-9062*.
- [18] Fjaer, E., Holt, R., and Stroisz . "Static vs Dynamic Moduli, another piece in the puzzle" *ARMA conference 2015*.
- [19] Fjaer, E. "Static and dynamic moduli of a weak sandstone" *GEOPHYSICS, 74(2), WA103-WA112*.

- [20] Grazielle L. P. and Marco A. R. "Difference between static and dynamic method of pore compressibility in carbonates" *15th International Congress of the Brazilian Geophysical Society and EXPOGEF, Rio de Janeiro, Brazil, 31 July-3 August 2017. August 2017, 903-907.*
- [21] Gardner, H.F., Gardner, L.W., and Gregory, A.R. "Formation velocity and density. The diagnostic basis for stratigraphic traps" *Geophysics (1974), Vol. 39(6), 770-780.*
- [22] Gassmann, F. "Uber die Elasiizatat poroser Medien. Vier. Der Natur" *Gesellschaft in Zyruch, 96, 1-23 (1951).*
- [23] Geertsma, J. "Velocity log interpretation. The effect of rock bulk compressibility" *SPEJ (Dec. 1961), 235-248.*
- [24] Graves, R.M. "Biaxial Acoustic and static measurement of rock elastic properties" *ph.D. Dissertation (T-2596), Colorado School of Mines, Golden, Colorado, USA. (1982).*
- [25] Grammatikopolos, J.N., Andreadis, Anagnostopoulos . "Determination of Modulus of elasticity Es in saturated clay- silty sand mixture"
- [26] Hamza, F., Chen, C., Gu, M., Quirein, J., Martysevich, V., and Matzar, L. "Characterization of Anisotropic Elastic Moduli and Stress for Unconventional Reservoirs Using Laboratory Static and Dynamic Geomechanical Data" *Society of Petroleum Engineers. doi:10.2118/175907-PA.*
- [27] Hathon, L.A., Myers, M.T. "Shale rock properties: Peak strength, acoustic anisotropy and rock fabric" *ARMA conference paper.*

- [28] Hathon, L., Myers, M., and Arad, A. "Controls on acoustic anisotropy observed in unconsolidated sands using laboratory measurements and digital rock technology" *Society of Exploration Geophysicists*.
- [29] Hertz, H.R. "On contact between elastic bodies" *Collected works, Vol 1, Leipzig Germany*.
- [30] Jizba, D., and A. Nur. "Static and dynamic moduli of tight gas sandstones and their relation to formation properties" *31st Annual Logging Symposium, Society of Professional Well Log Analysts, Paper BB*.
- [31] Johnston. Beer, F. R, Dewolf, J, and Mazurek, D. "Mechanics of materials" *New York: McGraw-Hill companies*.
- [32] Kachanov, M.L. "A microcrack model of rock inelasticity. Part I: Frictional sliding on microcracks." *Mech. Mater. 1: 19-27, 1982*.
- [33] King, M.S . "Static and dynamic elastic moduli of rocks under pressure" *Proc. 11 '• US Symposium on Rock Mechanics. 329-351*.
- [34] Kovari, K and A. Tisa . "Multiple failure state and strain controlled triaxial tests" *Rock Mechanics*.
- [35] Kuster, G.T., and Toksoz, M.N . "Velocity and Attenuation of Seismic Waves in Two phase Media. Part 1: Theoretical formulation, Part 2: Experimental Results" *Geophysics (1974), Vol.39, 587-618*.
- [36] Larsen, Fjaer, Renlie . "Static and dynamic Poisson's ratio of weak sandstones" *Pacific Rocks*.
- [37] Martin, m, R.J. and R.W. Haupt . "Static and dynamic elastic moduli on granite: The effect of strain amplitude. In P.P. Nelson and S.E. Lauback (eds.)" *Rock*

*Mechanics: Models and Measurements. Challenges from Industry. 473 -480. Rotterdam: Balkema.*

- [38] Mavko, G., Mukerji, T., Dvorkin, J. "The Rock Physics handbook" *Cambridge University Press, 2009.*
- [39] Mohr, O . "Uber die Darstellung des Spannungszustandes und des Deformationszustandes eines Korperelementes" *Zivilingenieur, 1882.*
- [40] Montmayeur, H. and R.M. Graves. "Prediction of Static Elastic/Mechanical Properties of Consolidated and Unconsolidated Sands from Acoustic Measurements" *Basic Measurements. SPE 14159.*
- [41] Myers, M.T., Hathon, L.A. "Compaction: Models from prediction from thin section data" *ARMA conference paper.*
- [42] Olsen, C., H. F. Christensen, and I. L. Fabricius . "Static and dynamic Young's moduli of chalk from the North Sea" *Geophysics, 73, no. 2, E41-E50.*
- [43] Plona, T.J. "Observation of a second bulk compressional wave in a Porous medium at ultrasonic frequencies" *Applied physical letter (1980), Vol. 36, 259-261.*
- [44] Prakash, S., Myers, M. T., Hathon, L. A. "Analysis of Damage Induced During a Multi-Stage Triaxial Test Using Acoustic Emissions." *ARMA, 2018.*
- [45] Roscoe, K.H., and Burland, J.B. "On the generalized stress-strain behavior of wet clay" *Engineering Plasticity, Cambridge, pp 535-609.*
- [46] Simmons, G. and W.F. Brace . "Comparison of static and dynamic measurements of compressibility of rocks" *J. Geophysical. Res. 70: 5649-5656.*
- [47] Tutuncu, A.N., M.M. Sharma and A.L. Podio . "Hysteresis observed in stress-strain diagrams and its relation to adhesion hysteresis and stick-slip sliding in

sedimentary granular rocks” In *J.J.K. Daemen and R.A. Schultz (eds.), Proceedings of the 35 • U.S. Symposium on Rock Mechanics. 801 - 806, Rotterdam: Balkema.*

- [48] Walsh, J.B . ”The effect of cracks on the uniaxial elastic compression of rocks”  
*Geophys. Res. 70: 399-441.*
- [49] Yale, D.P., J.A. Nieto and S.P. Austin . ”The effect of cementation on the static and dynamic mechanical properties of the Rotliegendes sandstone. In J.J.K. Daemen and R.A. Schultz ” *Proceedings of the 35 U.S. Symposium on Rock Mechanics. 169 - 175, Rotterdam: Balkema.*
- [50] Zimmerman R.W.,Jaeger J.C, Cook N.G.W. ”Fundamentals of Rock Mechanics ” *Malden, USA: Blackwell Publishing Ltd, 2009.*

# Appendix I

```
1 function k=LineCurvature2D(Vertices)
2 % This function calculates the curvature of a 2D line. It first fits
3 % polygons to the points. Then calculates the analytical ...
   curvature from
4 % the polygons;
5 %
6 % k = LineCurvature2D(Vertices,Lines)
7 %
8 % inputs,
9 %   Vertices : A M x 2 list of line points.
10 %   (optional)
11 %   Lines : A N x 2 list of line pieces, by indices of the vertices
12 %           (if not set assume Lines=[1 2; 2 3 ; ... ; M-1 M])
13 %
14 % outputs,
15 %   k : M x 1 Curvature values
16 %
17 %
18 %
19 % Example, Circle
20 % r=sort(rand(15,1))*2*pi;
21 % Vertices=[sin(r) cos(r)]*10;
22 % Lines=[(1:size(Vertices,1))' (2:size(Vertices,1)+1)']; ...
   Lines(end,2)=1;
23 % k=LineCurvature2D(Vertices,Lines);
24 %
25 % figure, hold on;
26 % N=LineNormals2D(Vertices,Lines);
27 % k=k*100;
```

```

28 % plot([Vertices(:,1) Vertices(:,1)+k.*N(:,1)]', [Vertices(:,2) ...
    Vertices(:,2)+k.*N(:,2)]', 'g');
29 % plot([Vertices(Lines(:,1),1) ...
    Vertices(Lines(:,2),1)]', [Vertices(Lines(:,1),2) ...
    Vertices(Lines(:,2),2)]', 'b');
30 % plot(sin(0:0.01:2*pi)*10, cos(0:0.01:2*pi)*10, 'r. ');
31 % axis equal;
32 %
33 % Example, Hand
34 % load('testdata');
35 % k=LineCurvature2D(Vertices,Lines);
36 %
37 % figure, hold on;
38 % N=LineNormals2D(Vertices,Lines);
39 % k=k*100;
40 % plot([Vertices(:,1) Vertices(:,1)+k.*N(:,1)]', [Vertices(:,2) ...
    Vertices(:,2)+k.*N(:,2)]', 'g');
41 % plot([Vertices(Lines(:,1),1) ...
    Vertices(Lines(:,2),1)]', [Vertices(Lines(:,1),2) ...
    Vertices(Lines(:,2),2)]', 'b');
42 % plot(Vertices(:,1),Vertices(:,2), 'r. ');
43 % axis equal;
44 %
45 % Function is written by D.Kroon University of Twente (August 2011)
46 % If no line-indices, assume a x(1) connected with x(2), x(3) ...
    with x(4) ...
47 if(nargin<2)
48     Lines=[(1:(size(Vertices,1)-1))' (2:size(Vertices,1))'];
49 end
50 % Get left and right neighbor of each points
51 Na=zeros(size(Vertices,1),1); Nb=zeros(size(Vertices,1),1);
52 Na(Lines(:,1))=Lines(:,2); Nb(Lines(:,2))=Lines(:,1);
53 % Check for end of line points, without a left or right neighbor

```

```

54 checkNa=Na==0; checkNb=Nb==0;
55 Naa=Na; Nbb=Nb;
56 Naa(checkNa)=find(checkNa); Nbb(checkNb)=find(checkNb);
57 % If no left neighbor use two right neighbors, and the same for ...
    right...
58 Na(checkNa)=Nbb(Nbb(checkNa)); Nb(checkNb)=Naa(Naa(checkNb));
59 % Correct for sampling differences
60 Ta=-sqrt(sum((Vertices-Vertices(Na,:)).^2,2));
61 Tb=sqrt(sum((Vertices-Vertices(Nb,:)).^2,2));
62 % If no left neighbor use two right neighbors, and the same for ...
    right...
63 Ta(checkNa)=-Ta(checkNa); Tb(checkNb)=-Tb(checkNb);
64 % Fit a polygons to the vertices
65 % x=a(3)*t^2 + a(2)*t + a(1)
66 % y=b(3)*t^2 + b(2)*t + b(1)
67 % we know the x,y of every vertice and set t=0 for the vertices, and
68 % t=Ta for left vertices, and t=Tb for right vertices,
69 x = [Vertices(Na,1) Vertices(:,1) Vertices(Nb,1)];
70 y = [Vertices(Na,2) Vertices(:,2) Vertices(Nb,2)];
71 M = [ones(size(Tb)) -Ta Ta.^2 ones(size(Tb)) zeros(size(Tb)) ...
    zeros(size(Tb)) ones(size(Tb)) -Tb Tb.^2];
72 invM=inverse3(M);
73 a(:,1)=invM(:,1,1).*x(:,1)+invM(:,2,1).*x(:,2)+invM(:,3,1).*x(:,3);
74 a(:,2)=invM(:,1,2).*x(:,1)+invM(:,2,2).*x(:,2)+invM(:,3,2).*x(:,3);
75 a(:,3)=invM(:,1,3).*x(:,1)+invM(:,2,3).*x(:,2)+invM(:,3,3).*x(:,3);
76 b(:,1)=invM(:,1,1).*y(:,1)+invM(:,2,1).*y(:,2)+invM(:,3,1).*y(:,3);
77 b(:,2)=invM(:,1,2).*y(:,1)+invM(:,2,2).*y(:,2)+invM(:,3,2).*y(:,3);
78 b(:,3)=invM(:,1,3).*y(:,1)+invM(:,2,3).*y(:,2)+invM(:,3,3).*y(:,3);
79 % Calculate the curvature from the fitted polygon
80 k = 2*(a(:,2).*b(:,3)-a(:,3).*b(:,2)) ./ ...
    ((a(:,2).^2+b(:,2).^2).^2).^2);
81 function Minv = inverse3(M)
82 % This function does inv(M) , but then for an array of 3x3 matrices

```

```

83 adjM(:,1,1)= M(:,5).*M(:,9)-M(:,8).*M(:,6);
84 adjM(:,1,2)= -(M(:,4).*M(:,9)-M(:,7).*M(:,6));
85 adjM(:,1,3)= M(:,4).*M(:,8)-M(:,7).*M(:,5);
86 adjM(:,2,1)= -(M(:,2).*M(:,9)-M(:,8).*M(:,3));
87 adjM(:,2,2)= M(:,1).*M(:,9)-M(:,7).*M(:,3);
88 adjM(:,2,3)= -(M(:,1).*M(:,8)-M(:,7).*M(:,2));
89 adjM(:,3,1)= M(:,2).*M(:,6)-M(:,5).*M(:,3);
90 adjM(:,3,2)= -(M(:,1).*M(:,6)-M(:,4).*M(:,3));
91 adjM(:,3,3)= M(:,1).*M(:,5)-M(:,4).*M(:,2);
92 detM=M(:,1).*M(:,5).*M(:,9)-M(:,1).*M(:,8).*M(:,6)-M(:,4).*M(:,2).*
93      M(:,9)+M(:,4).*M(:,8).*M(:,3)+M(:,7).*M(:,2).*M(:,6)-
94      M(:,7).*M(:,5).*M(:,3);
95 Minv=bsxfun(@rdivide,adjM,detM);

```

## Appendix II

```
1 classdef thisiscode_exported < matlab.apps.AppBase
2
3     % Properties that correspond to app components
4     properties (Access = public)
5         UIFigure                matlab.ui.Figure
6         kdEditFieldLabel        matlab.ui.control.Label
7         kdEditField             matlab.ui.control.NumericEditField
8         kmEditFieldLabel        matlab.ui.control.Label
9         kmEditField             matlab.ui.control.NumericEditField
10        DevMinEditFieldLabel     matlab.ui.control.Label
11        DevMinEditField         matlab.ui.control.NumericEditField
12        DevMaxEditFieldLabel     matlab.ui.control.Label
13        DevMaxEditField         matlab.ui.control.NumericEditField
14        MeanMinEditFieldLabel    matlab.ui.control.Label
15        MeanMinEditField        matlab.ui.control.NumericEditField
16        MeanMaxEditFieldLabel    matlab.ui.control.Label
17        MeanMaxEditField        matlab.ui.control.NumericEditField
18        MeanInitEditFieldLabel   matlab.ui.control.Label
19        MeanInitEditField       matlab.ui.control.NumericEditField
20        ThetaEditFieldLabel     matlab.ui.control.Label
21        ThetaEditField          matlab.ui.control.NumericEditField
22        UIAxes                  matlab.ui.control.UIAxes
23        compressibilityButton    matlab.ui.control.Button
24        checkEditFieldLabel      matlab.ui.control.Label
25        checkEditField          matlab.ui.control.NumericEditField
26        UIAxes2                 matlab.ui.control.UIAxes
27        UIAxes3                 matlab.ui.control.UIAxes
28        UIAxes4                 matlab.ui.control.UIAxes
29        DevoEditFieldLabel      matlab.ui.control.Label
```

```

30         DevoEditField          matlab.ui.control.NumericEditField
31         MeanoEditFieldLabel    matlab.ui.control.Label
32         MeanoEditField         matlab.ui.control.NumericEditField
33     end
34
35
36     properties (Access = public)
37         mydata = load('data-1-14.mat'); % Description
38
39     end
40
41     methods (Access = public)
42
43     end
44
45
46     methods (Access = private)
47
48         % Code that executes after component creation
49         function startupFcn(app)
50
51             %mydata = load('data-1-14.mat');
52
53
54         end
55
56         % Button pushed function: compressibilityButton
57         function compressibility(app, event)
58     for k = 1:15
59
60         dev(k) = app.DevMinEditField.Value+k*500;
61         mean(k) = ...
                dev(k)*app.ThetaEditField.Value+app.MeanInitEditField.Value;

```

```

62     mean4000(k) = dev(k)*app.ThetaEditField.Value + ...
           app.MeanInitEditField.Value-500;
63     mean5000(k) = dev(k)*app.ThetaEditField.Value + ...
           app.MeanInitEditField.Value+500;
64     mean5500(k) = dev(k)*app.ThetaEditField.Value + ...
           app.MeanInitEditField.Value+1000;
65     devo(k)=app.DevoEditField.Value;
66     meano(k)=app.MeanoEditField.Value;
67     end
68
69     kM = app.kmEditField.Value;
70     kM = app.kdEditField.Value;
71
72     for i = 1:15
73         compressibility(i) ...
           =(1.01E-7)*exp((mean(i)-app.mydata.castle4000(1,2)) ...
           *app.kmEditField.Value + (dev(i)- ...
           app.mydata.castle4000(1,3))* app.kdEditField.Value);
74     compressibility4000(i) =(1.01E-7)* exp((mean4000(i)- ...
           app.mydata.castle4000(1,2))* app.kmEditField.Value + ...
           (dev(i)-app.mydata.castle4000(1,3))* ...
           app.kdEditField.Value);
75     compressibility5000(i) =(1.01E-7)* exp((mean5000(i)- ...
           app.mydata.castle4000(1,2))* app.kmEditField.Value + ...
           (dev(i)- app.mydata.castle4000(1,3))* ...
           app.kdEditField.Value);
76     compressibility5500(i) =(1.01E-7)* exp((mean5500(i)- ...
           app.mydata.castle4000(1,2))* app.kmEditField.Value + ...
           (dev(i)- app.mydata.castle4000(1,3))* ...
           app.kdEditField.Value);
77     compressibility4500(i) =(1.01E-7)* exp((mean(i)- ...
           app.mydata.castle4000(1,2))* app.kmEditField.Value + ...
           (dev(i)- app.mydata.castle4000(1,3))* ...

```

```

        app.kdEditField.Value);
78     compressibilitym(i) =(1.01E-7)* exp((mean(i)- ...
        app.mydata.castle4000(1,2))* app.kmEditField.Value + ...
        (devo(k)- app.mydata.castle4000(1,3))* ...
        app.kdEditField.Value);
79     compressibilityd(i) = (1.01E-7)* exp((meano(k)- ...
        app.mydata.castle4000(1,2))* app.kmEditField.Value + ...
        (dev(i)- app.mydata.castle4000(1,3))* ...
        app.kdEditField.Value);
80     end
81
82     mean = mean.';
83     dev = dev.';
84     meano = meano.';
85     devo = devo.';
86     app.checkEditField.Value=dev(2);
87     %plot3(app.UIAxes,mean,dev,mean5000);
88
89     %%
90     j=1;
91
92     for i = 1:15
93         surface(j,1)= mean4000(i);
94         surface(j,2)=dev(i);
95         surface(j,3)=compressibility4000(i);
96         j=j+1;
97     end
98     for i = 1:15
99         surface(j,1)= mean(i);
100        surface(j,3)=compressibility4500(i);
101        surface(j,2)=dev(i);
102        j=j+1;
103    end

```

```

104 for i = 1:15
105     surface(j,1)= mean5000(i);
106     surface(j,2)=dev(i);
107     surface(j,3)=compressibility5000(i);
108     j=j+1;
109 end
110 for i = 1:15
111     surface(j,1)= mean5500(i);
112     surface(j,2)=dev(i);
113     surface(j,3)=compressibility5500(i);
114     j=j+1;
115 end
116
117
118 %%
119 ax=app.UIAxes2;
120 %scatter3 (app.UIAxes,mean,dev,compressibility);
121 %hold(app.UIAxes);
122
123
124 scatter3(app.UIAxes2,meano,dev,compressibilityd);
125 app.UIAxes2.ZLim=[0 0.00001];
126 app.UIAxes2.YLim=[9000 13000];
127 app.UIAxes2.XLim=[7000 10000];
128
129
130 hold(app.UIAxes2);
131 scatter3(app.UIAxes2,mean,devo,compressibilitym);
132
133 scatter (app.UIAxes3,dev,compressibilityd);
134 hold(app.UIAxes3);
135 scatter (app.UIAxes3,dev,compressibility5500);
136 app.UIAxes3.YLim=[0 0.00002];

```

```

137     app.UIAxes3.XLim=[9000 13000];
138
139     scatter (app.UIAxes4,mean,compressibilitym);
140     app.UIAxes4.XLim=[7000 10000];
141     app.UIAxes4.YLim=[0 0.00001];
142     hold(app.UIAxes4);
143     scatter (app.UIAxes4,mean,compressibility5500);
144
145
146
147     scatter3(app.UIAxes,surface(:,1),surface(:,2),surface(:,3));
148     %app.UIAxes.YLim=[9000 13000];
149     %app.UIAxes.XLim=[7000 10000];
150     app.UIAxes.ZLim=[0 0.000001];
151     hold(app.UIAxes);
152     tri = delaunay(surface(:,1),surface(:,2));
153     plot(app.UIAxes,surface(:,1),surface(:,2),'.')
154     %%
155     % How many triangles are there?
156     [r,c] = size(tri);
157     disp(r)
158     %% Plot it with TRISURF
159     trisurf(tri,surface(:,1), surface(:,2), ...
160             surface(:,3), 'Parent',app.UIAxes);
161
162     end
163
164
165     % App initialization and construction
166     methods (Access = private)
167
168     % Create UIFigure and components

```

```

169     function createComponents(app)
170
171         % Create UIFigure
172         app.UIFigure = uifigure;
173         app.UIFigure.Position = [100 100 913 671];
174         app.UIFigure.Name = 'UI Figure';
175
176         % Create kdEditFieldLabel
177         app.kdEditFieldLabel = uilabel(app.UIFigure);
178         app.kdEditFieldLabel.HorizontalAlignment = 'right';
179         app.kdEditFieldLabel.VerticalAlignment = 'top';
180         app.kdEditFieldLabel.Position = [51 588 25 15];
181         app.kdEditFieldLabel.Text = 'kd';
182
183         % Create kdEditField
184         app.kdEditField = uieditfield(app.UIFigure, 'numeric');
185         app.kdEditField.Position = [91 584 100 22];
186         app.kdEditField.Value = 0.002222;
187
188         % Create kmEditFieldLabel
189         app.kmEditFieldLabel = uilabel(app.UIFigure);
190         app.kmEditFieldLabel.HorizontalAlignment = 'right';
191         app.kmEditFieldLabel.VerticalAlignment = 'top';
192         app.kmEditFieldLabel.Position = [51 557 25 15];
193         app.kmEditFieldLabel.Text = 'km';
194
195         % Create kmEditField
196         app.kmEditField = uieditfield(app.UIFigure, 'numeric');
197         app.kmEditField.Position = [91 553 100 22];
198         app.kmEditField.Value = -0.001621;
199
200         % Create DevMinEditFieldLabel
201         app.DevMinEditFieldLabel = uilabel(app.UIFigure);

```

```

202     app.DevMinEditFieldLabel.HorizontalAlignment = 'right';
203     app.DevMinEditFieldLabel.VerticalAlignment = 'top';
204     app.DevMinEditFieldLabel.Position = [29 519 47 15];
205     app.DevMinEditFieldLabel.Text = 'DevMin';
206
207     % Create DevMinEditField
208     app.DevMinEditField = uieditfield(app.UIFigure, ...
209         'numeric');
210     app.DevMinEditField.Position = [91 515 100 22];
211     app.DevMinEditField.Value = 7000;
212
213     % Create DevMaxEditFieldLabel
214     app.DevMaxEditFieldLabel = uilabel(app.UIFigure);
215     app.DevMaxEditFieldLabel.HorizontalAlignment = 'right';
216     app.DevMaxEditFieldLabel.VerticalAlignment = 'top';
217     app.DevMaxEditFieldLabel.Position = [26 480 50 15];
218     app.DevMaxEditFieldLabel.Text = 'DevMax';
219
220     % Create DevMaxEditField
221     app.DevMaxEditField = uieditfield(app.UIFigure, ...
222         'numeric');
223     app.DevMaxEditField.Position = [91 476 100 22];
224     app.DevMaxEditField.Value = 15000;
225
226     % Create MeanMinEditFieldLabel
227     app.MeanMinEditFieldLabel = uilabel(app.UIFigure);
228     app.MeanMinEditFieldLabel.HorizontalAlignment = 'right';
229     app.MeanMinEditFieldLabel.VerticalAlignment = 'top';
230     app.MeanMinEditFieldLabel.Position = [20 441 56 15];
231     app.MeanMinEditFieldLabel.Text = 'MeanMin';
232
233     % Create MeanMinEditField

```

```

232     app.MeanMinEditField = uieditfield(app.UIFigure, ...
           'numeric');
233     app.MeanMinEditField.Position = [91 437 100 22];
234     app.MeanMinEditField.Value = 9000;
235
236     % Create MeanMaxEditFieldLabel
237     app.MeanMaxEditFieldLabel = uilabel(app.UIFigure);
238     app.MeanMaxEditFieldLabel.HorizontalAlignment = 'right';
239     app.MeanMaxEditFieldLabel.VerticalAlignment = 'top';
240     app.MeanMaxEditFieldLabel.Position = [17 406 59 15];
241     app.MeanMaxEditFieldLabel.Text = 'MeanMax';
242
243     % Create MeanMaxEditField
244     app.MeanMaxEditField = uieditfield(app.UIFigure, ...
           'numeric');
245     app.MeanMaxEditField.Position = [91 402 100 22];
246     app.MeanMaxEditField.Value = 15000;
247
248     % Create MeanInitEditFieldLabel
249     app.MeanInitEditFieldLabel = uilabel(app.UIFigure);
250     app.MeanInitEditFieldLabel.HorizontalAlignment = 'right';
251     app.MeanInitEditFieldLabel.VerticalAlignment = 'top';
252     app.MeanInitEditFieldLabel.Position = [23 367 52 15];
253     app.MeanInitEditFieldLabel.Text = 'MeanInit';
254
255     % Create MeanInitEditField
256     app.MeanInitEditField = uieditfield(app.UIFigure, ...
           'numeric');
257     app.MeanInitEditField.Position = [90 363 100 22];
258     app.MeanInitEditField.Value = 4500;
259
260     % Create ThetaEditFieldLabel
261     app.ThetaEditFieldLabel = uilabel(app.UIFigure);

```

```

262     app.ThetaEditFieldLabel.HorizontalAlignment = 'right';
263     app.ThetaEditFieldLabel.VerticalAlignment = 'top';
264     app.ThetaEditFieldLabel.Position = [39 335 36 15];
265     app.ThetaEditFieldLabel.Text = 'Theta';
266
267     % Create ThetaEditField
268     app.ThetaEditField = uieditfield(app.UIFigure, ...
269         'numeric');
270     app.ThetaEditField.Position = [90 331 100 22];
271     app.ThetaEditField.Value = 0.33;
272
273     % Create UIAxes
274     app.UIAxes = uiaxes(app.UIFigure);
275     title(app.UIAxes, 'Title')
276     xlabel(app.UIAxes, 'Mean stress')
277     ylabel(app.UIAxes, 'Deviatoric stress')
278     app.UIAxes.GridAlpha = 0.15;
279     app.UIAxes.MinorGridAlpha = 0.25;
280     app.UIAxes.XGrid = 'on';
281     app.UIAxes.YGrid = 'on';
282     app.UIAxes.ZGrid = 'on';
283     app.UIAxes.Position = [245 402 286 201];
284
285     % Create compressibilityButton
286     app.compressibilityButton = uibutton(app.UIFigure, ...
287         'push');
288     app.compressibilityButton.ButtonPushedFcn = ...
289         createCallbackFcn(app, @compressibility, true);
290     app.compressibilityButton.Position = [91 282 100 22];
291     app.compressibilityButton.Text = 'compressibility';
292
293     % Create checkEditFieldLabel
294     app.checkEditFieldLabel = uilabel(app.UIFigure);

```

```

292     app.checkEditFieldLabel.HorizontalAlignment = 'right';
293     app.checkEditFieldLabel.VerticalAlignment = 'top';
294     app.checkEditFieldLabel.Position = [39 247 37 15];
295     app.checkEditFieldLabel.Text = 'check';
296
297     % Create checkEditField
298     app.checkEditField = uieditfield(app.UIFigure, ...
299         'numeric');
300     app.checkEditField.Editable = 'off';
301     app.checkEditField.Position = [91 247 100 22];
302
303     % Create UIAxes2
304     app.UIAxes2 = uiaxes(app.UIFigure);
305     title(app.UIAxes2, 'Title')
306     xlabel(app.UIAxes2, 'Mean Stress')
307     ylabel(app.UIAxes2, 'Deviatoric Stress')
308     app.UIAxes2.XGrid = 'on';
309     app.UIAxes2.YGrid = 'on';
310     app.UIAxes2.ZGrid = 'on';
311     app.UIAxes2.Position = [556 410 300 185];
312
313     % Create UIAxes3
314     app.UIAxes3 = uiaxes(app.UIFigure);
315     title(app.UIAxes3, {'Constant Mean test'; ''})
316     xlabel(app.UIAxes3, 'Deviatoric stress')
317     ylabel(app.UIAxes3, {'compressibility'; ''})
318     app.UIAxes3.XGrid = 'on';
319     app.UIAxes3.YGrid = 'on';
320     app.UIAxes3.ZGrid = 'on';
321     app.UIAxes3.Position = [238 183 300 185];
322
323     % Create UIAxes4
324     app.UIAxes4 = uiaxes(app.UIFigure);

```

```

324     title(app.UIAxes4, 'Constant deviatoric stress')
325     xlabel(app.UIAxes4, 'Mean Stress')
326     ylabel(app.UIAxes4, 'Compressibility')
327     app.UIAxes4.XGrid = 'on';
328     app.UIAxes4.YGrid = 'on';
329     app.UIAxes4.ZGrid = 'on';
330     app.UIAxes4.Position = [556 183 300 185];
331
332     % Create DevoEditFieldLabel
333     app.DevoEditFieldLabel = uilabel(app.UIFigure);
334     app.DevoEditFieldLabel.HorizontalAlignment = 'right';
335     app.DevoEditFieldLabel.VerticalAlignment = 'top';
336     app.DevoEditFieldLabel.Position = [39 194 36 22];
337     app.DevoEditFieldLabel.Text = 'Devo';
338
339     % Create DevoEditField
340     app.DevoEditField = uieditfield(app.UIFigure, 'numeric');
341     app.DevoEditField.Limits = [9000 13000];
342     app.DevoEditField.Position = [90 197 100 22];
343     app.DevoEditField.Value = 11000;
344
345     % Create MeanoEditFieldLabel
346     app.MeanoEditFieldLabel = uilabel(app.UIFigure);
347     app.MeanoEditFieldLabel.HorizontalAlignment = 'right';
348     app.MeanoEditFieldLabel.VerticalAlignment = 'top';
349     app.MeanoEditFieldLabel.Position = [33 159 42 22];
350     app.MeanoEditFieldLabel.Text = 'Meano';
351
352     % Create MeanoEditField
353     app.MeanoEditField = uieditfield(app.UIFigure, ...
354         'numeric');
355     app.MeanoEditField.Limits = [7000 10000];
356     app.MeanoEditField.Position = [90 162 100 22];

```

```

356         app.MeanoEditField.Value = 8000;
357     end
358 end
359
360 methods (Access = public)
361
362     % Construct app
363     function app = thesiscode_exported
364
365         % Create and configure components
366         createComponents(app)
367
368         % Register the app with App Designer
369         registerApp(app, app.UIFigure)
370
371         % Execute the startup function
372         runStartupFcn(app, @startupFcn)
373
374         if nargin == 0
375             clear app
376         end
377     end
378
379     % Code that executes before app deletion
380     function delete(app)
381
382         % Delete UIFigure when app is deleted
383         delete(app.UIFigure)
384     end
385 end
386 end

```